UNIVERSIDAD DE CHILE
FACULTAD DE CIENCIAS FÍSICAS Y MATEMÁTICAS
ESCUELA DE POSTGRADO

Degeneration of internal gravity waves in a stratified rotating basin

Numerical and laboratory experiments

TESIS PARA OPTAR AL GRADO DE DOCTOR EN CIENCIAS DE LA INGENIERÍA
MENCIÓN FLUIDODINÁMICA

Hugo Nicolás Ulloa Sánchez

PROFESORES GUÍAS:
Yarko Niño Campos
Alberto de la Fuente Stranger
Kraig B. Winters

MIEMBROS DE LA COMISIÓN:
Cristián Escauriaza Mesa
Claudio Falcon Beas

Esta tesis ha sido parcialmente financiada por CONICYT
Beca de Doctorado Nacional No 21110069

SANTIAGO DE CHILE
2015

RESUMEN DE TESIS
PARA OPTAR AL GRADO DE DOCTOR EN
CIENCIAS DE LA INGENIERÍA
MENCIÓN FLUIDODINÁMICA
POR: HUGO N. ULLOA SÁNCHEZ
PROF. GUÍA: YARKO NIÑO CAMPOS

Degeneration of internal gravity waves in a stratified rotating basin Numerical and laboratory experiments

Con el fin de mejorar la comprensión de la dinámica no-lineal de las oscilaciones internas de gran escala observadas en lagos estratificados afectados por la rotación terrestre, se investigó la degeneración de 'ondas internas gravitacionales' (OIG) en un dominio idealizado, estratificado en dos capas separadas por una zona de transición continua de espesor dado.

Para obtener soluciones teóricas y construir condiciones iniciales de OIG, tales como ondas de Kelvin y Poincaré, se utilizó la teoría lineal de modos normales en un dominio cilíndrico rotatorio estratificado en dos capas. Estas soluciones fueron utilizadas para analizar experimentos de laboratorio y realizar simulaciones numéricas directas, que permitieron estudiar la degeneración de las OIG.

En primer lugar, se analizaron resultados de laboratorio obtenidos de experimentos desarrollados en una mesa rotatoria. A partir de estos resultados, se estudió la evolución temporal de las OIG de gran escala en un flujo estratificado en dos capas bajo diferentes escenarios de estratificación y rotación. El flujo inducido mediante la relajación de una inclinación inicial lineal de la interfaz de densidad, generó ondas gravitacionales de tipo Kelvin y Poincaré en respuesta al efecto de la rotación. Los resultados mostraron experimentalmente que la onda interna Kelvin fundamental degenera en un paquete de ondas tipo solitarias, producto del empinamiento y dispersión no-hidrostática. La rotación del medio determina la forma y estructura de estas ondas tipo solitarias. En particular, a medida que la rotación se incrementaba, las escalas de longitud de la onda tipo solitaria líder fueron muy similares a ondas no-lineales tipo KdV. Además, los resultados experimentales mostraron que existe una interacción no-lineal entre las ondas Kelvin y Poincaré, que podría inducir un estado pseudo-resonante entre ambas ondas y la transferencia de energía desde las modos fundamentales a sub-modos. En general, se observó que las condiciones de estratificación/rotación tienen un efecto importante en la intensidad de los procesos no lineales, los que a su vez mostraron un impacto directo en la tasa de decaimiento de la onda Kelvin. Esta tasa de decaimiento mostró concordancia con el decaimiento de Ekman y un incremento del decaimiento a medida que las no-linealidades se intensificaban.

En segundo lugar, se estudió la evolución de la onda interna Kelvin fundamental a través de simulaciones numéricas directas, con un enfoque híper-viscoso/difusivo, para condiciones de rotación y estratificación similares a las utilizadas en los experimentos de laboratorio. La dinámica de la onda fue controlada mediante el incremento de la amplitud inicial, forzando así la tendencia al empinamiento y el flujo de corte en la vecindad de la interfaz de densidad. Los resultados mostraron la existencia de diferentes regímenes, desde un régimen laminar amortiguado, en el que la onda Kelvin retuvo su carácter lineal, hasta un régimen no-lineal de transición a la turbulencia, en el que la dinámica no-lineal y no-hidrostática de la onda Kelvin indujo inestabilidades hidrodinámicas intermitentes en la interfaz de densidad. En el régimen de transición, se observaron parches de turbulencia producidos por quiebres parciales de la onda Kelvin en el interior de un radio interno de Rossby medido desde el borde horizontal hacia el interior. Estos parches se asociaron al crecimiento y colapso tanto de inestabilidades inducidas por corte, como de inestabilidades convectivas en la región del frente y cola de las ondas más energéticas.

El estudio permitió concluir que la amplitud de onda, la estratificación y la rotación del medio juegan roles importantes en la degeneración de las OIG de gran escala en lagos. Tanto la estructura de la estratificación como la amplitud de la onda tienen un efecto directo en el empinamiento de la onda, y en consecuencia un efecto en la concentración de energía en su dirección de propagación; mientras que la rotación tiene un efecto directo en la concentración de energía en la escala transversal de la propagación de la onda, la que es proporcional al radio interno de Rossby. Ambos mecanismos de concentración de energía generan una intensificación local de los procesos no-lineales, los cuales, a su vez, intensifican la actividad turbulenta y la mezcla en el medio fluido.

Summary

The degeneration of 'internal gravity waves' was investigated in an idealized stratified rotating basin, with the purpose of having a better understanding of the nonlinear dynamic of basin-scale motions observed in large stratified lakes.

The linear theory of normal modes was adopted to obtain solutions and construct suitable initial conditions of single internal gravity waves, – such as internal Kelvin and Poincaré waves –, and internal gravity wave fields, in a smooth two-layer stratified rotating cylindrical domain. The theoretical solutions were used to analyse laboratory experiments and to implement and perform direct numerical simulations (DNS).

The temporal evolution of nonlinear large-scale internal gravity waves, in a two-layer flow affected by background rotation, was studied via laboratory experiments conducted in a cylindrical tank on a rotating turntable. The internal wave field was excited by the relaxation of an initial forced tilt of the density interface, which generated Kelvin and Poincaré waves in response to rotation effects. The density interface evolution was analysed in the shore region in terms of the background rotation and the nonlinear steepening of the basin-scale internal waves. The results showed that the degeneration of the gravest internal Kelvin wave into a solitary-type wave packet was caused by nonlinear steepening and it was influenced by the background rotation. In fact, the physical scales of the leading solitary-type wave were closer to Korteweg-de Vries theory as the rotation increased. Moreover, the results showed a nonlinear interaction between Kelvin and Poincaré waves, which could lead to a pseudo-resonant state between both waves, and the transfer of energy from lower modes to higher modes. In general, the background stratification/rotation conditions showed having an important effect in the intensity of nonlinear processes, which in turn showed a direct impact on the decay rate of the gravest Kelvin waves. The experimental decay rate showed a good agreement with the Ekman damping rate when there was no evidence of steepening and it showed a strong increment of decay as nonlinearities increased.

The free evolution of the gravest internal Kelvin wave was studied via spectral based DNS with an hyper-viscosity/diffusivity approach, using stratification/rotation conditions similar to those observed in mid-latitude lakes during the season summer. The wave dynamics was controlled by increasing the initial wave amplitude, thus forcing the tendency for wave steepening and the shear in the vicinity of density interface. The results showed the existence of several regimes, from a damped linear-laminar regime (DLR), in which the Kelvin wave retains its linear character, to the nonlinear-turbulent transition regime (TR), in which nonlinearity and dispersion become significant in the evolution of the Kelvin wave, leading to intermittent hydrodynamic instabilities at the interface. In the TR, localized turbulent patches were produced by the Kelvin wave breaking, i.e. shear and convective instabilities that occurred at the front and tail of energetic waves, within an internal Rossby radius of deformation from the boundary.

The study allows concluding that the wave amplitude, the stratification structure and the background rotation play an important role in the degeneration of large-scale internal waves in enclosed basins. The stratification and the wave amplitude have a direct control in the potential wave steepening, and thus in the concentration of energy along the direction of the wave propagation; while the rotation has a direct effect in the concentration of energy along the transverse direction of the wave, which is proportional to the internal Rossby radius. Both mechanisms of energy concentration generate the local intensification of the nonlinear processes and the energy transfer from the large-scale to smaller scales, which in turn enhance the turbulence and mixing activity in the aquatic systems.

Any fact becomes important when it's connected to another. Umberto Eco

Acknowledgment

Quisiera partir agradeciendo a los Profesores Alberto de la Fuente, Aldo Tamburrino y Yarko Niño, quienes me apoyaron y guiaron tanto en el proceso de postulación al programa de Doctorado en Fluidodinámica, de la Universidad de Chile, como en la postulación a la Beca de Doctorado Nacional CONICYT (2011). Ellos pronunciaron las palabras claves para que las puertas se abrieran y para que yo avanzara.

Quiero dar un profundo agradecimiento a mis mentores, Yarko Niño, Alberto de la Fuente y Kraig Winters, de quienes recibí apoyo, crítica constructiva, libertad y la guía necesaria para desarrollar mis proyectos. En particular, agradezco a Yarko y Beto por darme siempre espacio en sus cargados horarios y por las oportunidades que me dieron para trabajar juntos en la docencia. A Kraig le quiero dar un especial agradecimiento por abrirme las puertas de SIO y de su hogar; mi estadía en California fue muy intensa e importante para mi formación personal y académica. Adicionalmente, quiero agradecer a los miembros de la comisión, al Profesor Cristián Escauriaza, y al Profesor Claudio Falcón, quien contribuyó con ideas valiosas para nuestro trabajo.

En el transcurso del doctorado, tuve la oportunidad de aprender y compartir con excelentes académicos. Particularmente, quiero dar las gracias a los Profesores Rodrigo Soto, Christian Ihle y Aldo Tamburrino, cuyas cátedras siempre estaban acompañadas de algo más que fluidodinámica.

Mi dirección, a lo largo de estos años, fue el Departamento de Ingeniería Civil, División de Recursos Hídricos y Medio Ambiente (FCFM, U. Chile). Quisiera agradecer a los académicos, funcionarios y estudiantes que componen a esta división; aquí encontré siempre lo necesario para disfrutar la jornada. Quiero agradecer además a Jacqueline Suarez, por su ayuda y preocupación, y al staff del Laboratorio de Hidráulica Francisco Javier Domínguez. En particular, quiero dar gracias a Tomás Trewhela, Rodrigo Pérez, Oscar Sepúlveda y Pedro Rojas, quienes siempre estuvieron dispuestos a leer un manuscrito preliminar y a discusiones metafísicas.

Durante este período fui siempre apoyado por el Programa de Doctorado en Fluiodinámica. Tengo que destacar y agradecer el trabajo realizado por los Directores y Profesores Rodrigo Soto, Jaime Ortega y Ricardo Muñoz, y a sus asistentes Bernardette Vásquez y Loreto Fuentes. Este equipo siempre ayudó a resolver ágilmente los temas administrativos propios del doctorado, y los temas contractuales con CONICYT. No puedo olvidar a mis colegas del doctorado: Santiago Montserrat, Mónica Bello, Francisca Guzmán, Eduardo Rojas, Juvenal Letelier y Sergio Palma, a quienes quiero dar las gracias por permitirme aprender de sus investigaciones y por compartir buenos momentos.

Quiero agradecer a mis patrocinadores:

- Esta tesis ha sido parcialmente financiada por CONICYT, Beca de Doctorado Nacional 2011, No 21110069.
- La asistencia a congresos en el extranjero fue parcialmente financiadas por: (1) el Programa de Doctorado en Fluidodinámica, de la Universidad de Chile, y (2) la 'Asignación Anual para Gastos Operacionales del Proyecto de Tesis Doctoral', CONICYT.
- La asistencia a congresos nacionales fue parcialmente financiada por la División de Recursos Hídricos y Medio Ambiente, del Departamento de Ingeniería Civil, FCFM, Universidad de Chile.
- La estadía de investigación en Scripps Institution of Oceanography (SIO), UC-SD, fue parcialmente financiada por: (1) la Beca de Estadías en el Extranjero (2012), del Departamento de Postgrado de la Universidad de Chile, y (2) por la US National Science Foundation (grant OCE-1155121).
- Los recursos computacionales utilizados durante la estadía de investigación en SIO fueron obtenidos a través del apoyo de XSEDE Computing Resources (grant TG-OCE 120004).
- "Powered@NLHPC: Esta investigación fue parcialmente apoyada por la infraestructura de supercómputo del NLHPC (ECM-02)".
- A mis amigos y anfitriones: Alvaro Ayala (Estadía en Zurich, Suiza), Martín Jacques-Coper (Estadía en Berna, Suiza) y Felipe Orellana (Estadía en Berkeley, USA).

Finalmente, quiero agradecer a mi padres, a mis hermanos de sangre y de vida, y a mi compañera, $\mathscr{M}\mathscr{X}$.

$\mathscr{H}$

Table of Contents

List of Figures

List of Tables

Chapter 1

Introduction

The physical description of lakes started in late 19th century (Forel, 1873; Murray, 1888; Watson, 1904; Wedderburn, 1908, 1909, 1912), with the detection of vertical gradients of temperature along the water column (vertical stratification) and coherent water motions both on the surface and the interior (seiches[1]), which obeyed to the wind action. During this period an integrative discipline denominated 'Limnology' was established by Forel (1892), and whose main purpose was to study the lakes and their aquatic ecosystems, from physics or hydrodynamics, chemistry and biology points of view. In present times, the study of lakes has been motivated by the notorious increment of water quality issues, such as water eutrophication, anoxic waters, loss of fish, benthos and wildlife habitat. In particular, large lakes have supported the development of human population and their activities: nourishment, transport, energy, tourism, etc. Most of these human activities have been intervening lakes and the quality of their waters. In this context, the physical description of the water motions and their transport properties are a fundamental issue in a lake ecosystem, because every aspect interacts with each other.

The framework of this thesis is the hydrodynamics of large stratified water basins (Csanady, 1975; Imberger & Hamblin, 1982). Here the adjective 'large' means that Earth's rotation is important in the basin-scale motions. The study is focused specifically in the evolution and degeneration of basin-scale internal gravity waves (Wüest & Lorke, 2003; Ivey *et al.*, 2008). These type of waves reside in internal interfaces of layered stratified basins, and these are mostly energized by the wind action across the free surface. Wind stress tends to be balanced by horizontal pressure gradients that tilt the internal interfaces, thus injecting energy to the larger scales. Then, when the wind stress decreases (or vanishes), the unbalanced, large-scale horizontal pressure gradient induces free internal motions in a wide range of scales denominated 'internal wave field'. Energy distribution in the internal wave field follows a cascade type structure, where most of the energy is located in the large-scale and this decays with a ω^{-2} law (Garrett & Munk, 1979), where ω is the frequency of internal waves. In a rotating and stratified flow, the limits of the internal gravity wave frequencies are the 'inertial frequency', f, which depends of the rotating environment, and the 'buoyancy frequency', $\mathcal{N}$, which depends of the stratified structure (Cushman-Roisin & Beckers, 2011): $f \leq \omega \leq \mathcal{N}$. In this range of frequency, we can find two well-known gravity waves, the super-inertial internal Kelvin and Poincaré waves (Csanady, 1967). However, in most of the large stratified lakes, the gravest basin-scale waves can be characterized by lower frequencies than f, such as the case of the sub-inertial internal Kelvin waves (Csanady, 1967). On the other hand, higher frequencies than $\mathcal{N}$ are related to nonlinear motions, which characterize the transition to turbulence.

This thesis is motivated by the field observations obtained from large stratified lakes during the last decade (Lorke, 2007; MacIntyre *et al.*, 2009; de la Fuente *et al.*, 2010; Bouffard *et al.*, 2012; Bouffard & Lemmin, 2013; Rozas *et al.*, 2014), which have shown the complex and nonlinear dynamic of basin-scale internal waves. With the aim of understanding the dynamics of the basin-scale internal waves under weakly nonlinear and non-hydrostatic limits de la Fuente *et al.* (2008) and Sakai & Redekopp (2010) developed numerical models and performed numerical experiments in an idealized, two-layer stratified rotating basin. Both authors obtained similar results, highlighting the steepening and the nonlinear degeneration of the internal Kelvin wave into a train of solitary type waves, and the not-steepen

[1]The word originates in a Swiss French dialect, which means 'rocking backwards and forwards' (Vincent, 2012)

dynamics of the internal Poincaré wave, with a pseudo oscillatory structure with time. In this thesis, we use laboratory and numerical experiments in an idealized domain to validate and extend these studies, on the nonlinear evolution of basin-scale internal waves in two-layer stratified rotating basins.

The main objective of this thesis was to investigate the degeneration[2] of basin-scale internal gravity waves in a two-layer stratified rotating basin. For this, we have adopted a simple setup in order to develop and test a basic theoretical model. Following this main directive, three specific objectives were defined:

1. To develop solutions of linear normal modes of internal gravity waves in a smoothly two-layer stratification into a rotating cylindrical basin. The aim was to have a continuous and smooth mathematical description of the Kelvin and Poincare waves, in terms of dimensionless parameter that allow controlling its dynamics. For this, we have adopted the Csanady's conceptual model (1967) as starting point.

2. To analyse the temporal evolution of basin-scale internal gravity waves via laboratory experiments. The aim was to characterize the dynamics of the gravest internal gravity waves in a internal wave field, parameterized in terms of the initial perturbation of the internal interface, the aspect ratio of the stratification and the background rotation. For this, we have analysed laboratory experiments conducted in a cylindrical tank, mounted on a rotating turntable (Ulloa, 2011).

3. To explore and characterize the evolution of the gravest internal Kelvin wave in a continuous two-layer rotating cylindrical basin in terms of dynamics and energetic regimes. The aim was to analyse the effect of the Kelvin wave amplitude in its evolution and degeneration, from damped, linear-laminar regime to the nonlinear-turbulent transition regime. For this, we have implemented the smooth solution of the Kelvin wave (previously obtained in Ulloa *et al.* (2015a)) in a numerical setup to perform numerical experiments, using the spectrally-based model *flow_solve* (Winters & de la Fuente, 2012).

This thesis consists of three main chapters; each of them includes an article (two of them already published), plus a chapter for the conclusions. In addition, the thesis has two appendices, which present the equations of motion of Boussinesq type fluids and the derivation of linear internal gravity waves in a stratified, inviscid, Boussinesq fluid on an f-plane, respectively. In Chapter 2, we introduce an analytical approach to construct three-dimensional smooth linear normal modes of internal gravity waves in an idealized continuous two-layer rotating basin, addressing the first specific goal of this thesis (Ulloa *et al.*, 2015a). In Chapter 3, we present the analysis of laboratory experiments conducted in a rotating turntable, which show the free evolution of the basin-scale waves under different environmental background (Ulloa *et al.*, 2014). In Chapter 4, we present the results and analysis of numerical experiments, which show the degeneration of the gravest internal Kelvin wave, addressing the second specific goal of this thesis (Ulloa *et al.*, 2015b). Finally, in Chapter 5 the main conclusions are summarized.

[2]In this thesis, the term 'degeneration' is used to denote the lost of energy of an internal gravity wave as a consequence of linear and/or nonlinear processes.

Chapter 2

Analytical construction of Kelvin and Poincaré modes in a smooth two-layer stratification. Application to the wave regimes study.

Abstract

We introduce an analytical approach to construct smooth linear normal modes (SLNM) that support arbitrary initial amplitudes in continuously stratified rotating fluids. Analytical solutions of internal Kelvin and Poincaré waves $(\vec{v}, \rho)$ in an ideal confined stratified basin are provided. The solutions are used as initial conditions to compute direct numerical simulations of the gravest internal Kelvin and Poincaré waves in a continuous two-layer stratification, to illustrate the evolution from a linear-laminar regime to a nonlinear, turbulent transition regime, characterized by the emergence of interfacial instabilities driven by shear stratified flows. The numerical experiments show important similarities with recent field data obtained in large stratified lakes.

2.1 Introduction

It is known that in mid-latitude large stratified lakes the wind forcing and the Earth rotation allow the existence of two main classes of linear gravity motions, widely known as internal Kelvin and Poincare waves (Thomson, 1880; Lamb, 1932; Csanady, 1967). A Kelvin wave is a sub-inertial cyclonic boundary-trapped wave whose amplitude $\eta_\ell(t, \vec{x})$ (of the layer ℓ) decays exponentially from the shore boundary to the interior and its horizontal flow has a strong shore-parallel component. A Poincaré wave is a super-inertial anti-cyclonic wave characterized by a cell structure on the horizontal plane, whose maximum amplitude is located at the center of the cell and its flow propagates mainly through the interior of the water body. Although the Kelvin and Poincaré waves have been theoretically characterized through linear equations of motion, field observations have shown a rich nonlinear phenomenology associated to them (Boegman *et al.*, 2003; Lorke, 2007; MacIntyre *et al.*, 2009; de la Fuente *et al.*, 2010; Preusse *et al.*, 2010; Bouffard *et al.*, 2012; Rozas *et al.*, 2014).

The degeneration of linear Kelvin and Poincaré waves has been studied using the following hypothesis: the initial linear waves that do not satisfy the linear theory assumptions of small amplitudes evolve to nonlinear waves. Assuming this hypothesis, theoretical, numerical and laboratory studies (Wake *et al.*, 2005; de la Fuente *et al.*, 2008; Sakai & Redekopp, 2010; Ulloa *et al.*, 2014) have explored the linear and weakly nonlinear evolution of Kelvin and Poincaré waves (Grimshaw, 1985) in ideal (layered) stratified rotating basins, adopting linear solutions as initial conditions (Csanady, 1967; Stocker & Imberger, 2003). These works have shown that the linear theory can predict with good agreement the dynamic of the gravest gravity waves in the wave field, but also can predict the weakly nonlinear degeneration of Kelvin waves into solitary-Kelvin waves when the advection and non-hydrostatic effects are important. A few laboratory experiments have analyzed the evolution and coexistence of Kelvin and Poincaré waves in nonlinear regimes (Maxworthy, 1983; Renouard *et al.*, 1987, 1993; Ulloa *et al.*, 2014), which have shown the incipient emergence of interfacial instabilities on the wavefronts as it

increases the wave amplitude, the existence of resonant interaction among Kelvin and Poincaré waves, and the similitude of the Kelvin wave evolution with KdV waves as rotation is more important in the gravity wave dynamics.

The emergence of interfacial instabilities and turbulent patches driven by the nonlinear internal gravity wave avance has been mainly studied in non-rotating stratified systems via laboratory and numerical experiments (Carr *et al.*, 2008, 2011; Fructus *et al.*, 2009). However, no numerical studies on the transition to turbulent regime driven by the nonlinear internal gravity wave evolution in rotating stratified basins have been conducted. In this type of flows a wide range of motions coexist and interact, from basin-scales (Kelvin and Poincaré) to small-turbulent scales. We are interested in exploring, via direct numerical simulations (DNS), the conditions under which Kelvin and Poincaré waves reach different dynamic regimes, focusing on the laminar to turbulent transition. For this type of numerical technique, the initial condition and subsequent solution must be smooth. Considering the aforementioned interest, we have revisited the linear normal modes problem in layered stratifications to obtain convenient initial conditions for DNS.

The remainder of the paper is organized as follows. In section 2.2 we introduce the formulation of the problem and we discuss briefly the pros and cons of the classical analytical solutions of internal Kelvin and Poincaré waves (Csanady, 1967, 1982) which are derived in section 2.3 for a discontinuous two-layer stratification, in a flat and lidded cylindrical basin. In section 2.4 we introduce an analytical approach based in Laplacian diffusion to construct smooth linear normal modes (here called SLNM) in a smooth two-layer stratification. In section 2.5 is characterized the interfacial shear flow resulting from the SLNM's construction, in terms of the gradient Richardson number, the rotation, the initial wave amplitude and the aspect ratio of the stratification. In section 2.6 we use the SLNM as initial condition to compute direct numerical simulations of internal Kelvin and Poincaré waves under different dynamic regimes, whose results are discussed in section 2.7.

2.2 Formulation

We consider a cylindrical geometry to construct free normal modes in a rotating stratified fluid. Two-layer solutions for rotating, inviscid linear normal modes in a cylindrical geometry are available (Csanady, 1967), which define the vertical interface displacement, η_ℓ (of the layer $\ell = 1, 2$), of the Kelvin and Poincaré modes. Figure 2.2.1 sketches the conceptual model of the two-layer model. The external parameters are the average thickness and density of each layer (h_ℓ and ρ_ℓ), the horizontal and vertical length scales, characterized by the diameter $D = 2R$ and the total depth $H = h_1 + h_2$, respectively, and the angular velocity of rotation $\Omega_z = f/2$ (in the direction of gravity), where f is the inertial frequency or Coriolis parameter. The linear modal celerity can be expressed as $c_\ell = \sqrt{g' D_\ell}$, where g' is the reduced gravity and D_ℓ is the equivalent modal depth that depends of h_ℓ and ρ_ℓ (Csanady, 1982). In the two-layer system, the internal Kelvin and Poincaré modes are conventionally obtained in the limit in which the Rossby radius of deformation, $R_\ell = c_\ell/f$, is smaller than the radius of the basin, R.

In the two-layer conceptual model (and in general in the layered models) the density and the horizontal velocity fields have a vertical discontinuity at the density interface, whose vertical position is characterized by η_ℓ. We define $\eta_0 = \max\{\eta_\ell(t = 0, \vec{x})\}$ that under the linear assumptions must satisfy $\eta_0/h_\ell \ll 1$. Despite this assumption of small motions, the two-layer solution allows defining

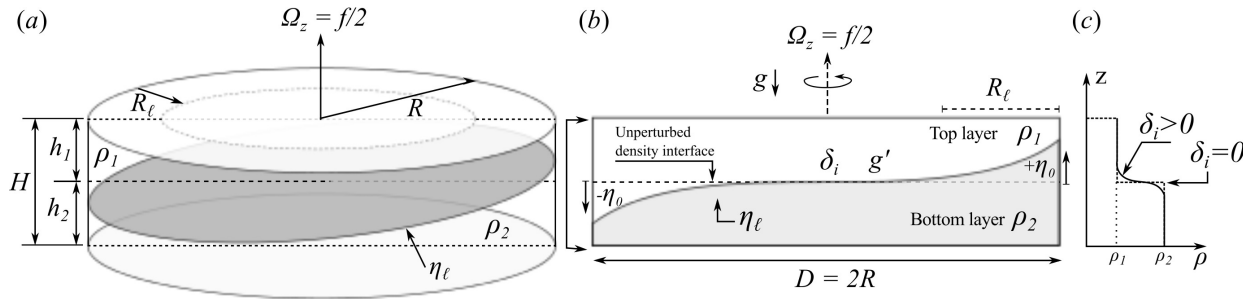

Figure 2.2.1: Schematic of the conceptual model. (a) a 3D view; (b) a 2D vertical plane view; (c) a 1D vertical density profile at the center of domain.

$\eta_0 \in [0, \min(h_1, h_2)]$ with no mathematical inconsistency in the equations. However, the velocity and density fields derived from this conceptual model are inconvenient as starting points for DNS that require continuous and smooth initial conditions.

On the other hand, we can assume a stratified fluid where fluid density and velocity vary continuously and smoothly across a finite length scale associated to the density interface, $\delta_\mathrm{i} > 0$ (see solid line in figure 2.2.1(c)). In the case of the two-layer solution: $\delta_\mathrm{i} = 0$ (see dash line in figure 2.2.1c). However, the normal modes derived from the solution of the continuous eigenvalue problem, $\delta_\mathrm{i} > 0$, are also inconvenient because these are formally restricted to have displacement amplitudes much smaller than δ_i (Kundu *et al.*, 2012). Consequently, in these cases, the flow would not be energetic enough to become nonlinear or turbulent. Here we wish to construct solutions to study the nonlinear transition regime and waves in this regime have amplitudes substantially larger than δ_i. To achieve this goal, we have constructed the velocity and density fields of linear internal Kelvin and Poincaré waves in a continuous and smooth two-layer stratification based on Csanady (1967) solutions for the two-layer flow. We have introduced a Laplacian diffusion process on the density and velocity fields to create a smooth transition layer, $\delta_\mathrm{i} > 0$, in the density interface region, with $\delta_\mathrm{i} \ll h_\ell$, to keep the two-layer structure. We addressed this problem in the next two sections. In section 2.3 we revisit the work of Csanady (1967) to obtain the modal structures of the density interface η_ℓ, which are used to derive the respective velocity field in a two-layer stratification with $\delta_\mathrm{i} = 0$. In section 2.4 we introduce the new analytical solution by considering a continuous and smooth two-layer stratification with $0 < \delta_\mathrm{i} \ll h_\ell$.

2.3 Normal modes in a two-layer stratification ($\delta_\mathrm{i} = 0$)

Csanady (1967) derived the 'free normal modes' in an incompressible, inviscid, two-layer stratified, Boussinesq fluid confined in a flat cylindrical geometry. Assuming hydrostaticity, $\partial p/\partial z + \rho g$, with p the fluid pressure, the vertically integrated linear equations of motion on an f-plane in cylindrical coordinates, for each ℓ-layer, take the form:

$$\frac{\partial}{\partial t}\begin{pmatrix} q_r \\ q_\theta \end{pmatrix}_\ell + f\begin{pmatrix} -q_\theta \\ q_r \end{pmatrix}_\ell + c_\ell^2 \nabla_H \eta_\ell = 0, \tag{2.3.1a}$$

$$\frac{1}{r}\left\{\frac{\partial\,(r \cdot q_r)}{\partial r} + \frac{\partial q_\theta}{\partial \theta}\right\}_\ell + \frac{\partial \eta_\ell}{\partial t} = 0. \tag{2.3.1b}$$

Here c_ℓ and η_ℓ are the modal celerity and the modal displacement of the ℓ-interface, ∇_H is the horizontal

gradient operator, f is the inertial frequency, while q_r and q_θ are the horizontal modal transport components defined for each layer ℓ as:

$$q_r^{(\ell)} = \int_\ell u(t,r,\theta)\mathrm{d}z\ , \qquad q_\theta^{(\ell)} = \int_\ell v(t,r,\theta)\mathrm{d}z, \tag{2.3.2}$$

where u and v are the horizontal velocity components in the r and θ axes, respectively.

In this study only internal modes of $\ell = 2$ are discussed. However the solution of the two-layer, three-layer or even for the n-layer problem, is analog to solve n independent equations of motions (2.3.1), by taking a suitable combination of the variables for the respective problem (Csanady, 1982; Stocker & Imberger, 2003).

We work in cylindrical coordinates ($r \in [0, R]$ and $\theta \in [0, 2\pi]$, $z \in [0, H]$) to facilitate the description of the boundary conditions, which in this case are:

$$q_r(t, r = R, \theta, z) = 0, \tag{2.3.3a}$$

$$w(t, r, \theta, z = 0) = 0, \quad w(t, r, \theta, z = H) = 0, \tag{2.3.3b}$$

$$\mathrm{d}\eta_\ell(t, r, \theta)/\mathrm{d}t - w(t, r, \theta, z = z_\ell) = 0, \tag{2.3.3c}$$

where w is the vertical velocity component, z_ℓ is the vertical position of the ℓth-interface. In addition, the symmetry of the problem indicates that the azimuthal component of the modal transport q_θ must be periodic.

A wave equation for η_ℓ is derived from equations (2.3.1):

$$\left(\frac{\partial^2}{\partial t^2} + f^2\right)\eta_\ell - c_\ell^2 \Delta_H \eta_\ell = 0. \tag{2.3.4}$$

Here Δ_H is the horizontal Laplacian operator. The boundary condition for η_ℓ (Csanady, 1967) is obtained after some manipulation of the equations of motion (2.3.1) and the boundary condition (2.3.3a):

$$\frac{\partial^2 \eta_\ell}{\partial r \partial t} + f\frac{1}{r}\frac{\partial \eta_\ell}{\partial \theta} = 0, \qquad \text{at } r = R. \tag{2.3.5}$$

We first derive the modal structure of $\eta_\ell(t, r, \theta)$ from equations (2.3.4) and (2.3.5). Note that in a two-layer system it is only possible to study the first vertical mode ($m = 1$) of each field.

2.3.1 Vertical displacement of the density interface: η_ℓ

We are interested in normal modes whose radial modal structure is an arbitrary function $G_\ell(r)$ and its azimuthal and temporal components are trigonometric functions. Wave solutions of η_ℓ can be sought in the form:

$$\eta_{\ell,n}(t, r, \theta) = \eta_0 \cdot G_{\ell,n}(r)\cos\left(n\theta - \omega_{\ell,n}t - \varphi\right). \tag{2.3.6}$$

Here $n \in \{1, 2, 3, ...\}$ is the azimuthal mode, θ is the azimuthal coordinate, $\omega_{\ell,n}$ is the wave frequency and φ is an arbitrary phase. Substituting (2.3.6) into (2.3.4) yields the following ordinary differential

equation (ODE):

$$\frac{\mathrm{d}^2 G_{\ell,n}}{\mathrm{d}r^2} + \frac{1}{r}\frac{\mathrm{d}G_{\ell,n}}{\mathrm{d}r} - \left(\frac{n^2}{r^2} - \frac{\omega_{\ell,n}^2 - f^2}{c_\ell^2}\right) G_{\ell,n} = 0. \tag{2.3.7}$$

To simplify the notation the following parameter is introduced:

$$\alpha_{\ell,n}^2 = \frac{\omega_{\ell,n}^2 - f^2}{c_\ell^2} = \frac{\sigma_{\ell,n}^2 - 1}{R_\ell^2}, \tag{2.3.8}$$

where $\sigma_{\ell,n} = \omega_{\ell,n}/f$ is the dimensionless wave frequency. So far we have not defined a sign for $\alpha_{\ell,n}^2$ but from (2.3.8), an important condition is infered. If $\alpha_{\ell,n}^2 > 0$, then $\omega_{\ell,n}^2 > f^2$, which means that we will find super-inertial wave frequencies. If $\alpha_{\ell,n}^2 < 0$, then $\omega^2 < f^2$, which means that we will find sub-inertial wave frequencies. The case $\alpha_{\ell,n}^2 = 0$ or $\omega^2 = f^2$ will not be addressed in this study, but a discussion of its meaning can be found in Pedlosky (1987, Chapter 3.9, pp 79-81). In general, the radial structure $G_{\ell,n}(r, \alpha_{\ell,n})$ will depend of the azimuthal mode n and the $\alpha_{\ell,n}$ parameter. We analyse the radial structure in terms of $\alpha_{\ell,n}^2$ next.

Radial structure G_ℓ: Case $\alpha_\ell^2 < 0$, Kelvin wave

We consider that $\alpha_{\ell,n}^2 < 0$ or $\sigma_{\ell,n}^2 < 1$ (sub-inertial waves). Just for mathematical convenience a new parameter $\beta_{\ell,n}$ is defined as $\beta_{\ell,n}^2 = -\alpha_{\ell,n}^2$. Then, using a stretching variable $r_\beta = \beta_{\ell,n} \cdot r$ and substituting $r = \beta_{\ell,n}^{-1} r_\beta$ in (2.3.7) yields a new ODE for $G_{\ell,n}$ in terms of r_β:

$$\frac{\mathrm{d}^2 G_{\ell,n}}{\mathrm{d}r_\beta^2} + \frac{1}{r_\beta}\frac{\mathrm{d}G_{\ell,n}}{\mathrm{d}r_\beta} - \left(\frac{n^2}{r_\beta^2} + 1\right) G_{\ell,n} = 0. \tag{2.3.9}$$

Equation (2.3.9) corresponds to a Modified Bessel equation whose solutions are the Modified Bessel functions (Abramowitz & Stegun, 1965):

$$G_{\ell,n}(r) = A \cdot I_n(\beta_{\ell,n} r) + B \cdot K_n(\beta_{\ell,n} r). \tag{2.3.10}$$

Here I_n is the Modified Bessel function of the first kind and K_n is the Modified Bessel function of the second kind, A and B are constants and n is the azimuthal mode. At the origin of r_β, $G_{\ell,n}(r_\beta) < \infty$. Then, as $K_n(r_\beta) \to \infty$ when $r_\beta \to 0$, the constant B must be zero. The boundary condition for the radial component $G_{\ell,n}$ is derived replacing η_ℓ in (2.3.5). Evaluating the result at $r = R$ an equation for $\omega_{\ell,n}$ is obtained as:

$$\omega_{\ell,n}\frac{\partial}{\partial_r} I_n(\beta_{\ell,n} R) + \frac{fn}{\beta_{\ell,n} R} I_n(\beta_{\ell,n} R) = 0, \tag{2.3.11}$$

where $\omega_{\ell,n}$ is the wave frequency linked to the azimuthal mode n and layer ℓ. Rearranging expression (2.3.11) and using the recursive properties of Modified Bessel function, yields a dispersion relation for $\sigma_{\ell,n} = \omega_{\ell,n}/f$ as a function of the Burger number (Antenucci & Imberger, 2001), $\mathcal{B}_\ell = R_\ell/R$:

$$\frac{\sqrt{1-\sigma_{n,\ell}^2}}{\mathcal{B}_\ell} I_{n-1}\left(\frac{\sqrt{1-\sigma_{\ell,n}^2}}{\mathcal{B}_\ell}\right) + n\left(\frac{1}{\sigma_{\ell,n}} - 1\right) I_n\left(\frac{\sqrt{1-\sigma_{n,\ell}^2}}{\mathcal{B}_\ell}\right) = 0. \tag{2.3.12}$$

For a specific set of n-mode and $\mathcal{B}_\ell$, equation (2.3.12) is numerically solved to obtain the wave frequency $\omega_{\ell,n}$, which in this case corresponds to a sub-inertial frequency ($\omega_{\ell,n} < f$). This kind of mode is known as **Kelvin wave** (Thomson, 1880) and the modal wave amplitude, $\eta_{\ell,n}$, is given by

$$\eta_{\ell,n}(t,r,\theta) = \eta_0 \cdot I_n\left(\frac{\sqrt{1-\sigma_{\ell,n}^2}}{\mathcal{B}_\ell}\frac{r}{R}\right)\cos(n\theta - \sigma_{\ell,n} f t - \varphi). \tag{2.3.13}$$

Radial structure G: Case $\alpha_\ell^2 > 0$, Poincaré wave

We consider that $\alpha_{\ell,n}^2 > 0$ or $\sigma_{\ell,n}^2 > 1$ (super-inertial waves). As in the first case, we use a stretching variable $r_\alpha = \alpha_{\ell,n} \cdot r$ which is substituted in equation (2.3.7) to obtain a new ODE for $G_{\ell,n}$ in terms of r_α:

$$\frac{\mathrm{d}^2 G_{\ell,n}}{\mathrm{d}r_\alpha^2} + \frac{1}{r_\alpha}\frac{\mathrm{d}G_{\ell,n}}{\mathrm{d}r_\alpha} - \left(\frac{n^2}{r_\alpha^2} - 1\right) G_{\ell,n} = 0. \tag{2.3.14}$$

Equation (2.3.14) corresponds to a Bessel equation, whose solutions are the Bessel functions (Abramowitz & Stegun, 1965)

$$G_{\ell,n}(r) = A \cdot J_n(\alpha_{\ell,n} r) + B \cdot Y_n(\alpha_{\ell,n} r). \tag{2.3.15}$$

Here J_n is the Bessel function of the first kind and Y_n is the Bessel function of the second kind, A and B are constants and n is the azimuthal mode. At the origin of r_α, $G_{\ell,n}(r_\alpha) < \infty$. Then, as $Y_n(r) \to \infty$ when $r \to 0$, the constant B must be zero. Similarly to the first case, a dispersion relation is obtained for $\sigma_{\ell,n} = \omega_{\ell,n}/f$ in terms of Bessel functions J_n and the Burger number $\mathcal{B}_\ell$:

$$\frac{\sqrt{\sigma_{\ell,n}^2 - 1}}{\mathcal{B}_\ell} J_{n-1}\left(\frac{\sqrt{\sigma_{n,\ell}^2 - 1}}{\mathcal{B}_\ell}\right) + n\left(\frac{1}{\sigma_{\ell,n}} - 1\right) J_n\left(\frac{\sqrt{\sigma_{\ell,n}^2 - 1}}{\mathcal{B}_\ell}\right) = 0. \tag{2.3.16}$$

For a specific set of n-mode and $\mathcal{B}_\ell$, equation (2.3.16) is numerically solved to obtain the wave frequency $\omega_{\ell,n}$, which in this case corresponds to a super-inertial frequency ($\omega_{\ell,n} > f$). This kind of mode is known as **Poincaré wave** (Poincaré, 1885) and the modal wave amplitude, $\eta_{\ell,n}$, is given by:

$$\eta_{\ell,n}(t,r,\theta) = \eta_0 \cdot J_n\left(\frac{\sqrt{\sigma_{\ell,n}^2 - 1}}{\mathcal{B}_\ell}\frac{r}{R}\right)\cos(n\theta - \sigma_{\ell,n} f t - \varphi). \tag{2.3.17}$$

2.3.2 Horizontal component of velocity field: $(U_r, U_\theta)_{\ell,n} = (q_r, q_\theta)_{\ell,n}/h_\ell$

We look for $(q_r, q_\theta)_{\ell,n}$ with the same structure of η_ℓ:

$$\begin{aligned} q_r^{(\ell,n)}(t,r,\theta) &= q_{0,r} \cdot G_{q_r}(r)\Theta_{q_r}(n\theta - \omega_{\ell,n} t - \varphi), \\ q_\theta^{(\ell,n)}(t,r,\theta) &= q_{0,\theta} \cdot G_{q_\theta}(r)\Theta_{q_\theta}(n\theta - \omega_{\ell,n} t - \varphi), \end{aligned} \tag{2.3.18}$$

where G_q and Θ_q are the radial and the azimuthal-temporal modal structures of the horizontal modal transport, respectively. Replacing (2.3.6) and (2.3.18) into (2.3.1), $(q_r, q_\theta)_\ell$ is given by:

$$\begin{aligned} q_r^{(\ell,n)}(t,r,\theta) &= \frac{\eta_0}{\alpha_{\ell,n}^2}\left\{\omega_{\ell,n}\frac{\partial}{\partial r}\, G_{\ell,n}(\alpha_{\ell,n}r) - \frac{f\cdot n}{r}G_{\ell,n}(\alpha_{\ell,n}r)\right\}\sin(n\theta-\omega_{\ell,n}t-\varphi),\\ q_\theta^{(\ell,n)}(t,r,\theta) &= -\frac{\eta_0}{\alpha_{\ell,n}^2}\left\{f\frac{\partial}{\partial r}\, G_{\ell,n}(\alpha_{\ell,n}r) - \frac{\omega_{\ell,n}\cdot n}{r}G_{\ell,n}(\alpha_{\ell,n}r)\right\}\cos(n\theta-\omega_{\ell,n}t-\varphi). \end{aligned} \tag{2.3.19}$$

Considering the definition (2.3.2), the averaged horizontal velocity field on the ℓth-layer is $(U_r, U_\theta)_{\ell,n} = (q_r, q_\theta)_{\ell,n}/h_\ell(t,r,\theta)$. In particular, in a two-layer basin, neglecting the vertical displacement of barotropic modes ($\ell = 1$), $\eta_{1,n} \sim 0$, and keeping constant the total depth H, the contribution of baroclinic modes on the two-layer horizontal velocity field is

$$\begin{aligned} U_r^{(1,n)}(t,r,\theta) &= \frac{q_r^{(1,n)}(t,r,\theta)}{h_1-\eta_{2,n}(t,r,\theta)}\,, \quad U_\theta^{(1,n)}(t,r,\theta) = \frac{q_\theta^{(1,n)}(t,r,\theta)}{h_1-\eta_{2,n}(t,r,\theta)},\\ U_r^{(2,n)}(t,r,\theta) &= \frac{q_r^{(2,n)}(t,r,\theta)}{h_2+\eta_{2,n}(t,r,\theta)}\,, \quad U_\theta^{(2,n)}(t,r,\theta) = \frac{q_\theta^{(2,n)}(t,r,\theta)}{h_{2,n}+\eta_2(t,r,\theta)}. \end{aligned} \tag{2.3.20}$$

2.3.3 Vertical component of velocity field: $w_{\ell,n}$

We have assumed hydrostaticity in the equations of motion, $w_{\ell,n} \sim 0$. However, this approach admits the estimation of the vertical velocity, $w_{\ell,n}$, at the internal interface ($\ell = 2$), and on the vertical boundaries:

$$\begin{aligned} w_{2,n}(t,r,\theta,z=z_{2,n}) &= \frac{\mathrm{d}\eta_{2,n}}{\mathrm{d}t} = \frac{\partial\eta_{2,n}}{\partial t} + U_r^{(2,n)}\frac{\partial\eta_{2,n}}{\partial r} + U_\theta^{(2,n)}\frac{1}{r}\frac{\partial\eta_{2,n}}{\partial\theta},\\ w_{\ell,n}(t,r,\theta,z=0) &= w_{\ell,n}(t,r,\theta,z=H) = 0, \end{aligned} \tag{2.3.21}$$

where $z_{2,n}(t,r,\theta) = h_2 + \eta_{2,n}(t,r,\theta)$ is the height of the internal interface. Additionally, the horizontal velocity components $(U_r, U_\theta)_{\ell,n}$ are constant along the thickness of each layer by construction, hence, from the continuity equations, it is derived that $w_{2,n}$ is a linear function of z whose vertical velocity structure can be expressed as follows (Choi & Camassa, 1999):

$$w_{\ell,n} = a_{\ell,n}\cdot z + b_{\ell,n}, \tag{2.3.22}$$

where $a_{\ell,n}$ and $b_{\ell,n}$ are constants for each layer and mode. Substituting (2.3.22) into (2.3.21) and considering that $w_{1,n}(t,r,\theta,z=z_{2,n}) = w_{2,n}(t,r,\theta,z=z_{2,n})$, the constants $a_{\ell,n}$ and $b_{\ell,n}$ are solved and $w_{\ell,n}$ is determined:

$$w_{\ell,n}(t,r,\theta,z) = \begin{cases} w_{1,n} = \frac{\mathrm{d}\eta_{2,n}}{\mathrm{d}t}\left(\frac{H-z}{h_1-\eta_{2,n}}\right) & z \geq z_{2,n}\\ w_{2,n} = \frac{\mathrm{d}\eta_{2,n}}{\mathrm{d}t}\left(\frac{z}{h_2+\eta_{2,n}}\right) & z \leq z_{2,n} \end{cases} \tag{2.3.23}$$

Note that when $\eta_0 = 0$, then $\eta_{2,n} = 0$ and $U_r = U_\theta = w = 0$.

2.4 Normal modes in a smooth two-layer stratification ($0 < \delta_\mathrm{i} \ll h_1$)

In the previous section we have derived the modal structure of the internal gravity waves in a two-layer stratification, assuming a null thickness of the density interface, $\delta_\mathrm{i} = 0$. The discontinuous structure of the density function, at $z = z_{2,n}$, generates a discontinuity on the horizontal velocity component at the same height. This, additionally, generates undefined vertical derivatives at $z = z_{2,n}$. Hence, these modal solutions are not useful as starting point for direct numerical simulations (DNS), because of their mathematical singularities at the density interface. In this section we construct new smooth solutions, which are suitable as a starting point for DNS.

In a two-layer stratification, the velocity and density fields of the previously derived Kelvin and Poincaré waves can be mathematically expressed as :

$$\begin{pmatrix} U_r \\ U_\theta \\ w \end{pmatrix} = \begin{pmatrix} U_r \\ U_\theta \\ w \end{pmatrix}_2 \cdot \{1 - \mathcal{H}(z - z_{2,n})\} + \begin{pmatrix} U_r \\ U_\theta \\ w \end{pmatrix}_1 \cdot \mathcal{H}(z - z_{2,n}), \tag{2.4.1a}$$

$$\rho = \rho_2 \cdot \{1 - \mathcal{H}(z - z_{2,n})\} + \rho_1 \cdot \mathcal{H}(z - z_{2,n}), \tag{2.4.1b}$$

where $\mathcal{H}$ is the Heaviside function. Starting from solutions as (2.4.1) we wish to get a continuous and smooth version of the fields. For this, we propose to use a controlled vertical Laplacian diffusion along the vertical component of ρ and (U_r, U_θ, w) during a time scale to construct new continuous and smooth solutions. We then must solve the following diffusion equation:

$$\frac{\partial \phi}{\partial t} = \mathcal{D}_c \frac{\partial^2 \phi}{\partial z^2}, \tag{2.4.2}$$

where $\phi = \phi(t, r, \theta, z)$ is a field to diffuse in z and $\mathcal{D}_c$ is a diffusion coefficient. The boundary conditions to solve (2.4.2) depend of each field. In the case of ρ and (U_r, U_θ), Neumann boundary conditions are imposed at $z = 0$ and $z = H$, which are interpreted as no-flux through the boundary and free-slip condition, respectively:

$$\frac{\partial \phi}{\partial z} = 0 \quad \text{at } z = 0, H. \tag{2.4.3}$$

In the the case of w, Dirichlet boundary conditions are imposed:

$$\phi = 0 \quad \text{at } z = 0, H. \tag{2.4.4}$$

Both problems have analytical solutions described by Fourier Series. Hereafter we use a sub-index 'i' instead of $\ell = 2$, to denote properties at the internal interface (e.g., $z_2 = z_\mathrm{i}$, $\eta_2 = \eta_\mathrm{i}$). In the first case (Neumann conditions), the analytical solution of equation (2.4.2) is given by:

$$\phi = \frac{a_0}{2} + \sum_{k=1}^{\infty} a_k \cos\left(\frac{k\pi}{H} z\right) \mathrm{e}^{-\gamma_k t}, \tag{2.4.5}$$

where a_0 and a_k are defined as:

$$\begin{aligned} a_0 &= \frac{2 z_\mathrm{i}}{H} (\phi_2 - \phi_1) + 2\phi_1, \\ a_k &= 2 \sin\left(\frac{k\pi z_\mathrm{i}}{H}\right) \left(\frac{\phi_2 - \phi_1}{k\pi}\right), \end{aligned} \tag{2.4.6}$$

ϕ_1 and ϕ_2 are the initial values of the field ϕ in each layer, with $\gamma_k = (k\pi)^2\mathcal{D}_c/H^2$. In the second case (Dirichlet condition), the analytical solution of equation (2.4.2) is given by:

$$\phi = \sum_{k=1}^{\infty} b_k \sin\left(\frac{k\pi}{H}z\right) \mathrm{e}^{-\gamma_k t}, \tag{2.4.7}$$

where b_k is defined as follows:

$$\begin{aligned} b_k^{(1)} &= \frac{2\phi_\mathrm{i}}{k\pi(h_2+\eta_\mathrm{i})}\left\{\frac{H}{k\pi}\sin\left(\frac{k\pi z_\mathrm{i}}{H}\right) - z_\mathrm{i}\cos\left(\frac{k\pi z_\mathrm{i}}{H}\right)\right\}, \\ b_k^{(2)} &= \frac{2\phi_\mathrm{i}}{k\pi(h_1-\eta_\mathrm{i})}\left\{\frac{H}{k\pi}\sin\left(\frac{k\pi z_\mathrm{i}}{H}\right) + (H-z_\mathrm{i})\cos\left(\frac{k\pi z_\mathrm{i}}{H}\right)\right\}, \end{aligned} \tag{2.4.8}$$

with $b_k = b_k^{(1)} + b_k^{(2)}$ and $\phi_\mathrm{i} = \phi(z = z_\mathrm{i})$. The values of ϕ_1, ϕ_2 and ϕ_i are obtained from equations (2.3.22). Then, the smooth versions of (U_r, U_θ, w) and ρ are written as follows:

$$\begin{pmatrix} U_r(t,r,\theta,z) \\ U_\theta(t,r,\theta,z) \end{pmatrix} = \frac{z_\mathrm{i}(r,\theta)}{H}\begin{pmatrix} \Delta U_r \\ \Delta U_\theta \end{pmatrix} + \begin{pmatrix} U_r \\ U_\theta \end{pmatrix}_1 + \sum_{k=1}^{\infty}\begin{pmatrix} a_k^{(U_r)}(r,\theta) \\ a_k^{(U_\theta)}(r,\theta) \end{pmatrix}\cos\left(\frac{k\pi}{H}z\right)\mathrm{e}^{-\gamma_k t}, \tag{2.4.9a}$$

$$w(t,r,\theta,z) = \sum_{k=1}^{\infty} b_k(r,\theta)\sin\left(\frac{k\pi}{H}z\right)\mathrm{e}^{-\gamma_k t}, \tag{2.4.9b}$$

$$\rho(t,r,\theta,z) = \frac{z_\mathrm{i}(r,\theta)}{H}\Delta\rho + \rho_0 + \sum_{k=1}^{\infty} a_k(r,\theta)\cos\left(\frac{k\pi}{H}z\right)\mathrm{e}^{-\gamma_k t}, \tag{2.4.9c}$$

where $\Delta\rho = \rho_2 - \rho_1$, $\Delta U_r = U_r^{(2)}(r,\theta) - U_r^{(1)}(r,\theta)$ and $\Delta U_\theta = U_\theta^{(2)}(r,\theta) - U_\theta^{(1)}(r,\theta)$. Finally, each field is described by the linear superposition of smooth functions (C^∞). For $t > 0$ the solution (2.4.9) constructs normal modes with smooth density interface transitions, and we can specifically define a time scale $t_{\delta_\mathrm{i}} = \delta_\mathrm{i}^2/\mathcal{D}_c$, in which the vertical diffusion process occurs given the length scale δ_i and the diffusion coefficient $\mathcal{D}_c$.

An example of smooth linear normal modes (SLNM) obtained from (2.4.9) for a time scale $t = t_{\delta_\mathrm{i}}$ are illustrated in figures 2.4.1, 2.4.2 and 2.4.3. Figure 2.4.1 shows the density field ρ and buoyancy frequency, $\mathcal{N} = \sqrt{-(g/\rho_0)\mathrm{d}\rho/\mathrm{d}z}$, derived from the analytical solution at $t = 0$ (grey line: discontinuous two-layer stratification) and $t = t_{\delta_\mathrm{i}}$ (red line: smooth two-layer stratification). Density and velocity fields of the gravest modes ($n = 1$) of Kelvin and Poincaré waves are exhibited in figures 2.4.2 and 2.4.3 for $\mathcal{B}_2 = 0.25$, $h_1/H = 0.35$, and $\eta_0/h_1 = 0.5$.

2.5 Gradient Richardson number of SLNM

The flows induced by the linear internal Kelvin and Poincaré waves are parallel and predominantly horizontal. Indeed, the ratio between the vertical and horizontal wavelengths is usually very small, $\lambda_V/\lambda_H < \mathcal{O}(10^{-2})$. Hence, the hydrodynamic stability of the parallel two-layer flow drives by the SLNM can be examined via the computation of the local gradient Richardson number, $\mathcal{J}$, or its inverse version:

$$\mathcal{J}^{-1} \equiv \frac{\mathcal{S}^2}{\mathcal{N}^2}, \tag{2.5.1}$$

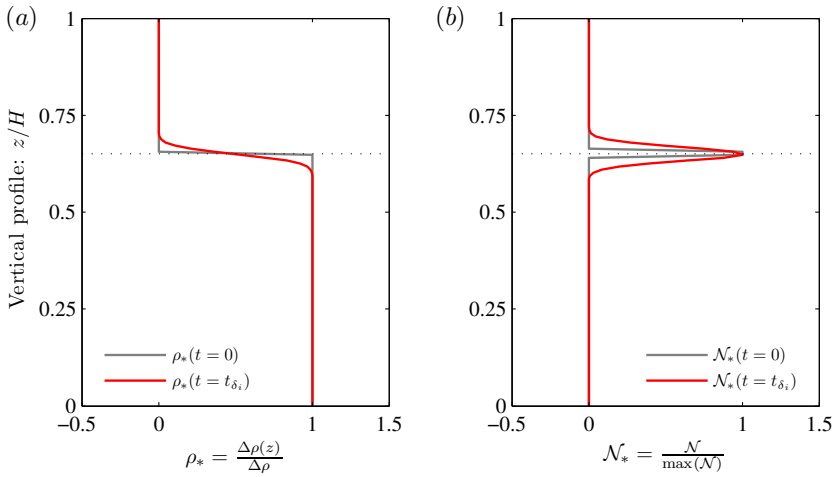

Figure 2.4.1: Density profile $\Delta\rho(z)/\Delta\rho$ and buoyancy frequency $\mathcal{N}(z)$ of two-layer stratification, $\delta_i(t=0)=0$ (grey line), and smooth two-layer stratification, $0<\delta_i(t_{\delta_i}>0)\ll h_1$ (red line).

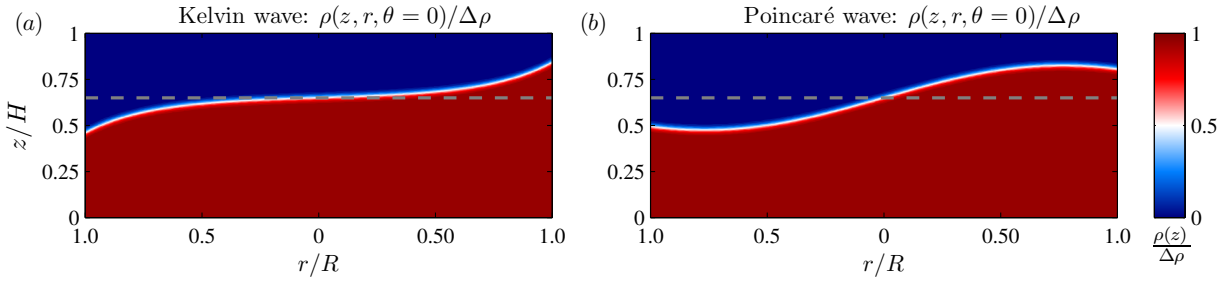

Figure 2.4.2: Density field of Kelvin and Poincaré waves on the plane $x-z$ at $y=L_y/2$; dash line shows the vertical position of density interface in the unperturbed state.

where $\mathcal{S}=\mathrm{d}U/\mathrm{d}z$ is the vertical shear rate of the horizontal flow U and whose critical value is $J_c^{-1}=4$. The Miles–Howard theorem (Miles, 1961; Howard, 1961) states that the sufficient condition for hydrodynamic stability in a parallel stratified shear flow is satisfied if $\mathcal{J}<\mathcal{J}_c^{-1}$ everywhere; a value $\mathcal{J}_c^{-1}=4$ is a necessary but no sufficient condition for instabilities. However, local values $\mathcal{J}>\mathcal{J}_c^{-1}$ suggest that shear instabilities are a distinct possibility around the density interface.

In a two-layer stratified flow both $\mathcal{N}^2$ and $\mathcal{S}^2$ have a unique maximum located at the density interface, $z=z_i$. From the SLNM we can compute $\mathcal{J}^{-1}$ and estimate its maximum value near the density interface, and where it occurs. As a first approach, we can assume that hydrodynamic stability of Kelvin and Poincaré flows is similar to the stability of continuously stratified parallel flow in a non-rotating limit. Therefore, we can solve the equation

$$\mathcal{J}_c^{-1}=4=\frac{\mathcal{S}^2\left(\mathcal{B}_2,\delta_i/H,h_1/H,\eta_0/h_1\right)}{\mathcal{N}^2\left(\delta_i/H,\Delta\rho/\rho_0\right)}, \tag{2.5.2}$$

The spatial structure of the shear rate is controlled by four parameters: the rotation through the Burger number $\mathcal{B}_2$, the aspect ratios of the stratification δ_i/H, h_1/H, and the dimensionless wave amplitude η_0/h_1. Then, for a given combination of $(\mathcal{B}_2,h_1/H,\delta_i/H)$ and $\mathcal{N}$, we can solve η_0/h_1 to obtain the critical value $\mathcal{J}_c=1/4$. We define the vertical shear rate as $\mathcal{S}^2\equiv\left\{(\mathrm{d}U_r/\mathrm{d}z)^2+(\mathrm{d}U_\theta/\mathrm{d}z)^2\right\}$.

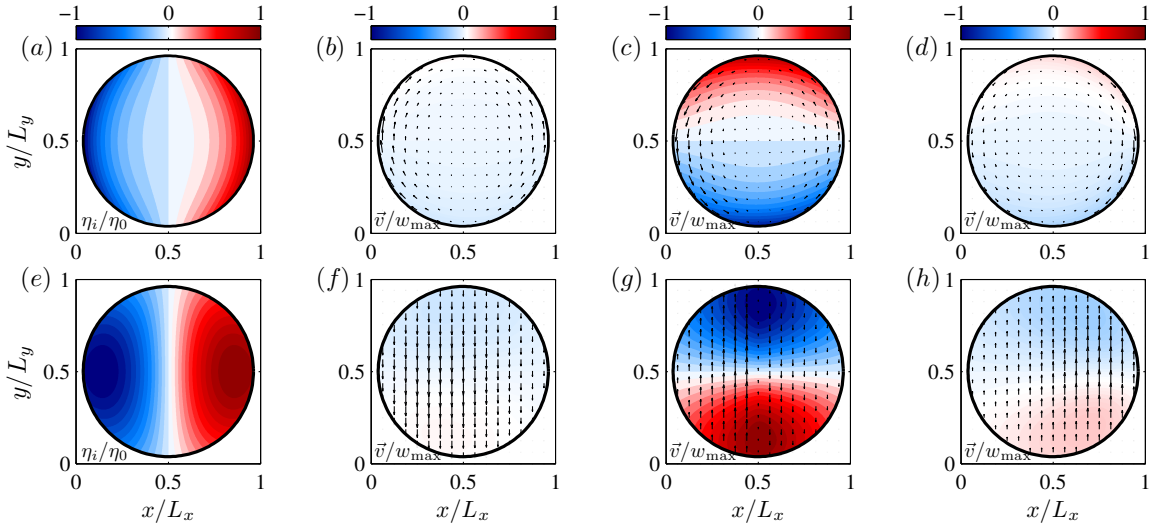

Figure 2.4.3: Panels (a) and (e) show the vertical displacement $\eta_{\rm i}/\eta_0$ of gravest internal Kelvin/Poincaré waves. Panels (b)-(f), (c)-(g) and (d)-(h) show the dimensionless velocity field $\vec{v}/w_{\max}$ at $z/H = 0.05$, $z/H = 0.65$ and $z/H = 0.95$, respectively. Arrows show the horizontal velocity components (U_r, U_θ) and background colours shows the vertical velocity component w.

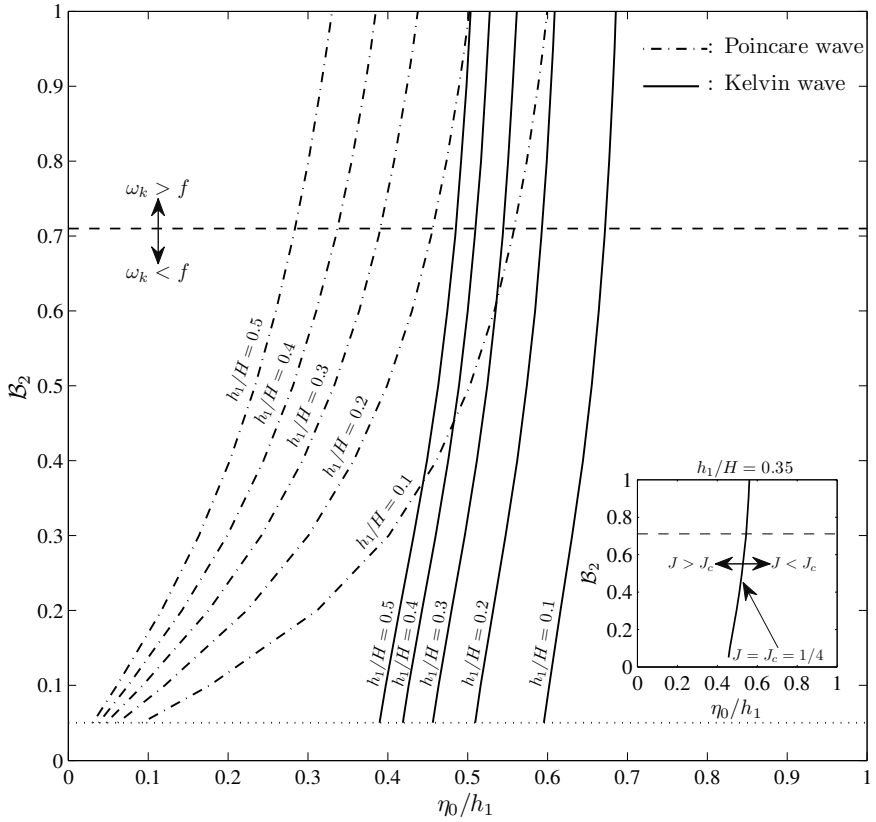

Figure 2.5.1: Curves of the critical gradient Richardson number, $\mathcal{J}_c = 1/4$, at the density interface in terms of $\mathcal{B}_2$, η_0/h_1, h_1/H, $\delta_{\rm i}/H = 5 \times 10^{-2}$, in a sheared flow induced by the gravest internal Kelvin and Poincaré waves in solid lines and dash-dot lines, respectively.

Figure 2.5.1 shows the space of parameter $\mathcal{J}(\mathcal{B}_2, \eta_0/H, h_1/H)$, with $\mathcal{B}_2 \in [0.05, 1.0]$, $\eta_0/h_1 \in [0.05, 1.0]$, $\eta_1/H \in [0.1, 0.5]$, $\delta_i/H = 5 \times 10^{-2}$ and $\Delta\rho/\rho_0 = 1.5 \times 10^{-2}$; solid lines denote a family of solutions of equation (2.5.2) for the gravest internal Kelvin wave flow ($n = 1, \ell = 2$) whereas dash-dot lines denote a family of solutions of equation (2.5.2) for the gravest internal Poincaré wave flow ($n = 1, \ell = 2$). Each curve divides the space of parameter in two regions: to the right of the curves, the flow has regions where $J < J_c$; while to the left of the curves, the flow has $J > J_c$ everywhere. From figure 2.5.1 we highlight the following characteristics: (1) for a given initial amplitude, η_0/h_1, and an aspect ratio of the stratification, h_1/H, both the Kelvin and Poincaré waves tend to unstable flow as rotation effect increases ($\mathcal{B}_2 \to 0$), but this effect is more important in the Poincaré wave; (2) given a rotating regime, $\mathcal{B}_2$, and an initial amplitude, η_0/h_1, both the Kelvin and Poincaré waves tend to unstable flow as aspect ratio increases ($h_1/H \to 0.5$); and (3) given a rotating regime, $\mathcal{B}_2$, and an aspect ratio of the stratification, h_i/H, both the Kelvin and Poincaré waves tend to unstable flow as wave amplitude increases $\eta_0/h_1 \to 1.0$. These results are discussed in the next section.

2.6 Direct numerical simulation of Kelvin and Poincaré waves

Nine three-dimensional numerical experiments were performed using the SLNMs as initial conditions, to illustrate the free evolution and degeneration of the gravest internal Kelvin and Poincaé waves. The parameters used were $\mathcal{B}_2 = 0.25$, $h_1/H = 0.35$ and $\delta_i/H = 5 \times 10^{-2}$. Six experiments of the internal Kelvin wave varied its initial wave amplitude between $0.07 \leq \eta_0/h_1 \leq 0.60$ and its minimum gradient Richardson number between $0.13 \leq \min\{\mathcal{J}\} \leq 31.86$, and three experiments of the internal Poincaré wave varied its initial wave amplitude between $0.05 \leq \eta_0/h_1 \leq 0.15$ and its minimum gradient Richardson number between $0.34 \leq \min\{\mathcal{J}\} \leq 18.57$. After the initial condition, the flow motion was computed via the direct numerical simulation of the equations of motion (momentum, continuity and mass transport equations in the Boussinesq sense) using the spectral model **flow_solve** (Winters & de la Fuente, 2012), with a hyper-viscosity/diffusivity approach. Free-slip and no-flux conditions on the boundaries were employed to solve the governing equation in the physical domain schematized in figure 2.2.1. For more details on the equations of motion and the numerical approach, read Chapter 4, subsection 4.2.1.

Figure 2.6.1 show results of the internal Kelvin wave evolution. Left panels of figure 2.6.1 show time series of vertical density profiles at $r/R = 0.98$ and $\theta = 0$, for different values of η_0/h_1, whereas the right panels show the respective power spectral density of the local potential energy, $E_p(t) = \int_0^H \rho(t, z) g \mathrm{d}z$. The increment of η_0/h_1 induces an intensification of both the wave steepening and the shear flow in the density interface region, around the maximum wave amplitude. The results show the existence of different regimes: from a damped linear and laminar regime, associated to amplitudes η_0 that scale with the thickness of the transition layer δ_i, in which the Kelvin wave retains most of the linear characteristics, to a nonlinear turbulent transition regime (T.R.), associated with amplitudes η_0 that scale with the thickness of the thinner layer, h_1, in which the nonlinear processes induce the growth of interfacial instabilities and turbulent patches in the density interface vicinity. These nonlinear processes were observed when $\max\{\mathcal{J}^{-1}\} > 4$. As the Kelvin wave dynamics tends to its linear regime, $\eta_i \to 0$, the theoretical Kelvin wave frequency, ω_K, is virtually the frequency reproduced by the numerical simulations that shows that the new smoothed solution preserves the linear modal structure of the two-layer solution. Further description and characterization on these regimes are given in Ulloa *et al.* (2015b).

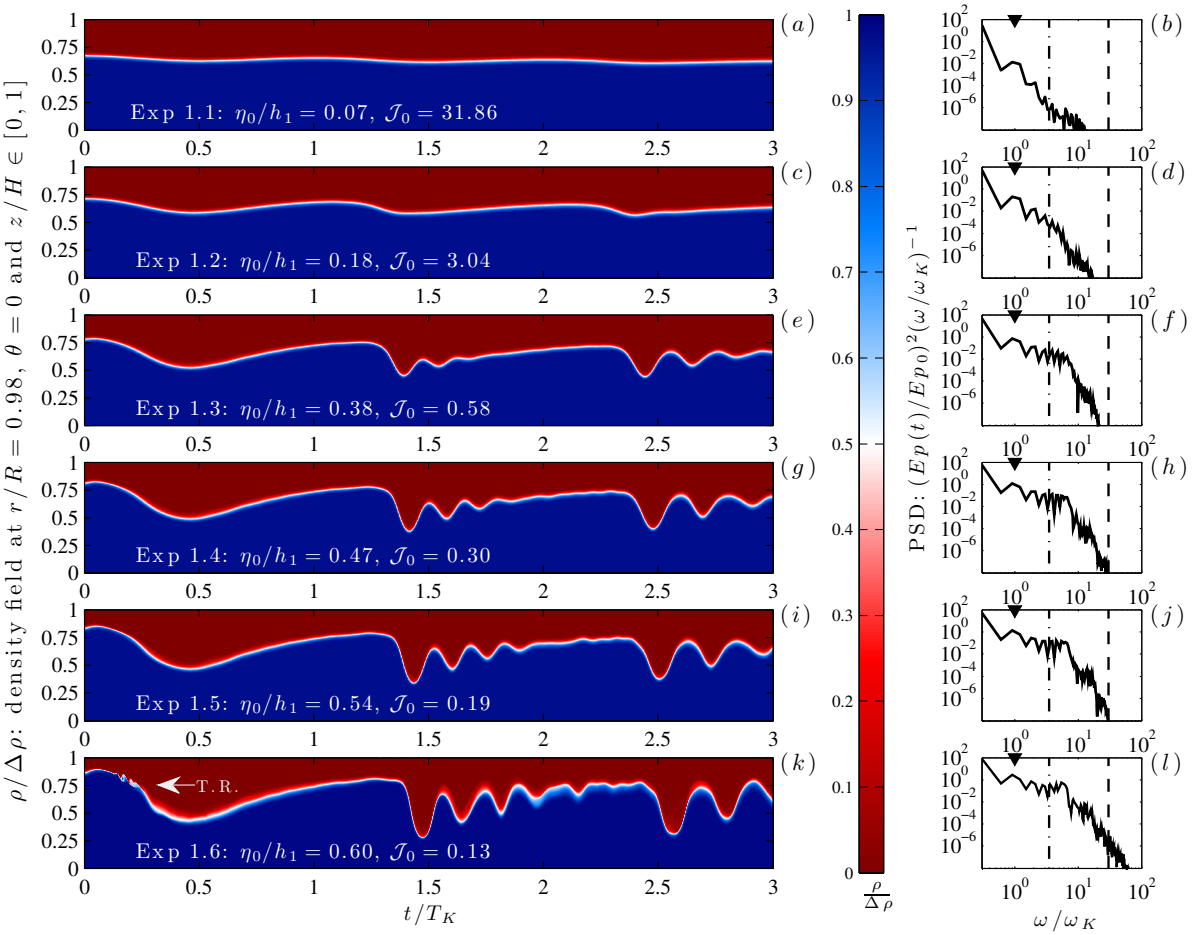

Figure 2.6.1: Left panels exhibit time series of density field along the vertical profile near where the maximum Kelvin wave amplitude is achieved. **T.R.**: region where interfacial instabilities grow. Right panels exhibit the power spectral density of the local potential energy, $E_p(t)$. Legend: ▼ : ω_k/ω_k; *dash-line*: $\mathcal{N}_0/\omega_k$; *dot-dash line*: f/ω_k

Figure 2.6.2 shows results of the internal Poincaré wave evolution. Figures 2.6.1(a) to 2.6.1(f) show time series (in the left panels) of vertical density profiles at $r/R = 0.0$ and $\theta = 0$, for three different values of η_0/h_1, with their respective power spectral density of the local potential energy, $E_p(t) = \int_0^H \rho(t,z)g\mathrm{d}z$ (in the right panels); while figures 2.6.1(g) to 2.6.1(l) show the same information but at $r/R = 0.98$ and $\theta = 0$. The results show the existence of a local transition from laminar to turbulent regime (T.R.) in the center of domain for $\eta_0/h_1 = 0.15$ and $\min\{J\} \approx 0.34 > \mathcal{J}_c = 0.25$, which is not observed in the perimeter. In fact, in the perimeter it is only observed the signal of a Poincaré wave, with a single energy peak at the Poincaré-wave frequency in the PSDs of figures 2.6.2(h, j, l). In the PSDs of the interior region, wider frequency bands are observed as η_0/h_1 increases, even with higher frequencies than the initial interfacial buoyancy frequency $\mathcal{N}_0$ (dash-line) in the case of the transition regime, as shown in figure 2.6.2(f).

The dynamics of Poincare wave has been studied by de la Fuente *et al.* (2008) and Sakai & Redekopp (2010), both authors have found that Poincare wave does not exhibit the nonlinear degeneration and the hyperbolic characteristics observed in the Kelvin wave. In the shore region, we observe similar results than previous studies (de la Fuente *et al.*, 2008; Sakai & Redekopp, 2010); however, we observe

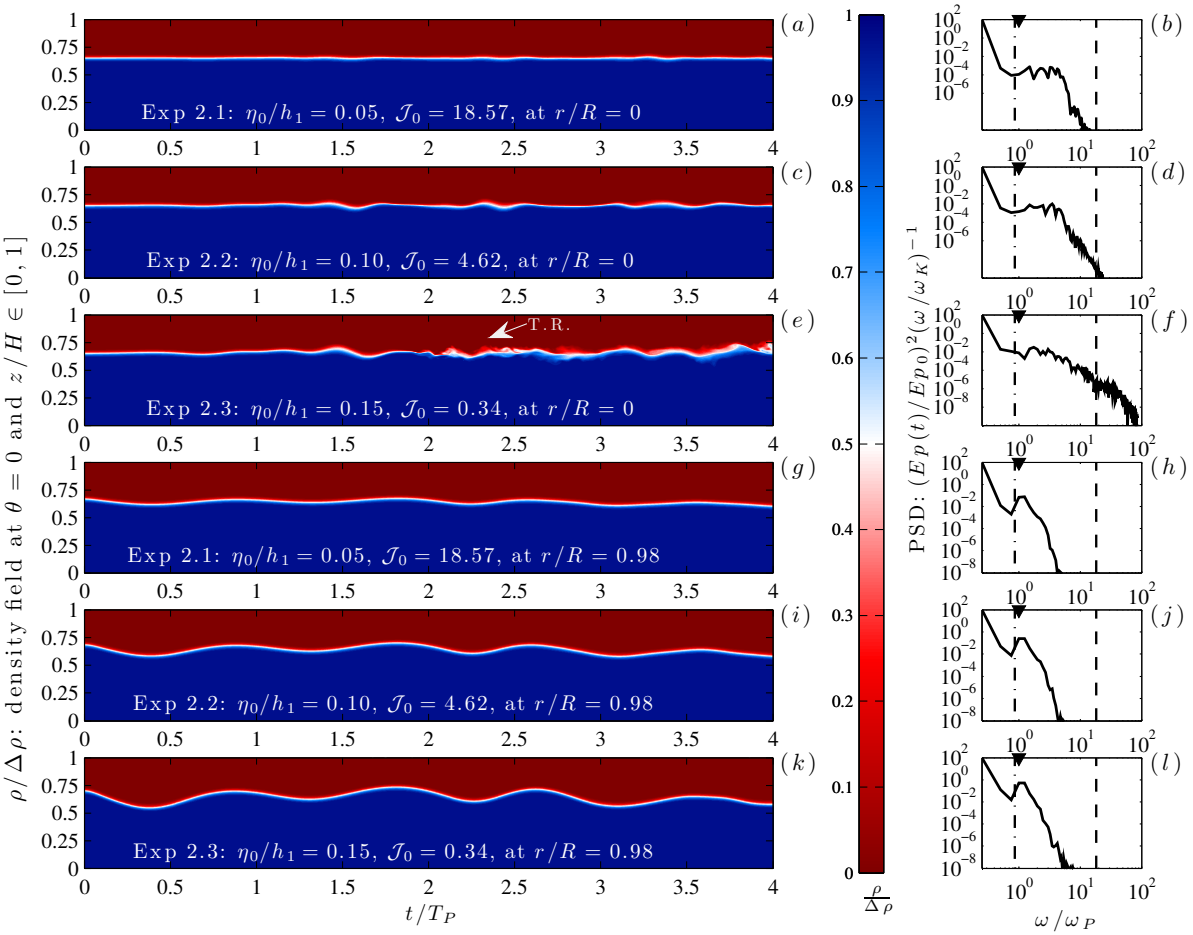

Figure 2.6.2: Left panels exhibit time series of density field along the vertical profile near where the maximum Poincaré wave amplitude is achieved. **T.R.**: region where interfacial instabilities grow. Right panels exhibit the power spectral density of the local potential energy, $E_p(t)$. Legend: $\blacktriangledown : \omega_p/\omega_p$; *dash-line*: $\mathcal{N}_0/\omega_p$; *dot-dash line*: f/ω_p

a transition to turbulence in the interior region, where Poincaré wave has the strongest interfacial shear flow. Indeed, recent field studies in large stratified lakes (Bouffard *et al.*, 2012, 2014; Valipour *et al.*, 2015) have suggested that the gravest internal Poincaré waves induce vertical mixing in offshore regions via shear instabilities.

2.7 Discussion

Previous numerical studies have explored the evolution of Kelvin and Poincaré waves in confined rotating stratified fluids via linear and weakly nonlinear equations (de la Fuente *et al.*, 2008; Sakai & Redekopp, 2010). Consequently, these studies have analyzed the linear and weakly nonlinear dynamics of the Kelvin and Poincaré waves. Here we have introduced an analytical approach to construct smooth lineal normal modes (SLNMs) of Kelvin and Poincaré waves in a smooth two-layer stratification, starting from the linear normal modes derived by Csanady (1967) in a discontinuous two-layer stratification. Unlike the linear normal modes derived directly from continuous stratifications

(e.g., Kundu *et al.*, 2012), the wave amplitude of SLNMs, η_0, can be taken as a significant fraction of the thinner layer thickness. This property allows storing enough energy as to induce strong nonlinear flows if proper nonlinear equations are solved. We have used the SLNMs as initial conditions to compute the free evolution of the gravest internal Kelvin and Poincaré waves via DNS of the fully nonlinear Boussinesq equations of motion. This approach allowed obtaining strong nonlinear regimes of Kelvin and Poincaré waves.

Our numerical experiments show important physical processes associated to turbulent events and vertical mixing in the density interface region, when the minimum gradient Richardson number in the density interface region is close to the critical value $\mathcal{J}_c = 0.25$. In the case of internal Kelvin wave, we observed the emergence of interfacial instabilities when $\min\{J\} \leq \mathcal{J}_c$, whereas in the case of internal Poincaré waves, we observed the emergence of interfacial instabilities at partially-higher values than $\mathcal{J}_c$. Similar results have been recently observed in large stratified lakes (e.g., Preusse *et al.*, 2010; Bouffard *et al.*, 2012). Preusse *et al.* (2010) have shown that internal Kelvin waves degenerate into nonlinear internal waves with high amplitudes that drive interfacial instabilities and turbulent patches near the crests and troughs of waves, in the shore region, as it is shown in the numerical experiments of the internal Kelvin wave (see figure 2.6.1). On the other hand, Bouffard *et al.* (2012) have shown that internal Poincaré waves induce intensive shear flow in the interior region of large lakes, driving turbulent events and vertical mixing in the density interface region, as it is shown in the numerical experiments of the internal Poincaré wave (see figure 2.6.2).

The numerical experiments presented here showed the individual evolution of the gravest internal Kelvin and Poincaré waves. However, these waves can coexist and interact with each other in large stratified lakes (Rozas *et al.*, 2014). Therefore we could expect, at least, two sources of turbulence and mixing driven by basin-scale internal gravity waves. To analyse these scenarios further studies are required.

Acknowledgement

The authors acknowledge support from the Civil Engineering Department, University de Chile, and the Scripps Institution of Oceanography, University of California San Diego. This work was partially supported by the U.S. National Science Foundation (grant number OCE-1155121) and XSEDE computing resources (grant TG-OCE 120004). Powered@NLHPC: This research was partially supported by the supercomputing infrastructure of the NLHPC (ECM-02), Center for Mathematical Modeling, Universidad de Chile. KBW acknowledges support from a Fulbright Fellowship. The first author acknowledges financial support from the CONICYT Doctoral Fellowship No. 21110069 and the Postgraduate Department Scholarship, Universidad de Chile (Research Internship Abroad, 2012).

Chapter 3

Degeneration of internal gravity waves in a stratified rotating basin. Laboratory experiments

This chapter has been published as research paper, authored by Hugo Ulloa, Alberto de la Fuente and Yarko Niño, in Journal of Fluid Mechanics (2014), http://dx.doi.org/10.1017/jfm.2014.10.

Abstract

The temporal evolution of nonlinear large-scale internal gravity waves, in a two-layer flow affected by background rotation, is studied via laboratory experiments conducted in a cylindrical tank, mounted on a rotating turntable. The internal wave field is excited by the relaxation of an initial forced tilt of the density interface (η_{i}), which generates internal waves, such as Kelvin and Poincaré waves, in response to rotation effects. The behaviour of η_{i}, in the shore region, is analysed in terms of the background rotation and the nonlinear steepening of the basin-scale waves. The results show that the degeneration of the fundamental Kelvin wave into a solitary-type wave packet is caused by nonlinear steepening and it is influenced by the background rotation. In addition, the physical scales of the leading solitary-type wave are closer to Korteweg-de Vries theory as the rotation increases. Moreover, the nonlinear interaction between the Kelvin wave and the Poincaré wave can transfer energy to higher or lower frequencies than the frequency of the fundamental Kelvin wave, as a function of the background rotation. In particular, a specific normal mode in the off-shore region could be energized by this interaction. Finally, the bulk decay rate of the fundamental Kelvin wave, $\tau_{\mathrm{d}k}$, was investigated. The results exhibit that $\tau_{\mathrm{d}k}$ is concordant with the Ekman damping time scale when there is no evidence of steepening in the basin-scale waves. However, as nonlinear processes increase, $\tau_{\mathrm{d}k}$ shows a strong decrease. In this context, the nonlinear processes play an important role in the decay of the fundamental Kelvin wave, via the energy radiation to other modes. The results reported demonstrate that the background rotation and nonlinear processes are essential aspects in understanding the degeneration and the decay of large-scale internal gravity waves on enclosed basins.

3.1 Introduction

The nonlinear and non-hydrostatic degeneration of large-scale internal gravity waves has been observed in environmental stratified flows (Staquet & Sommeria, 2002; MacIntyre *et al.*, 2009; Preusse *et al.*, 2010, 2012b; Rozas *et al.*, 2014). It plays an important role in the energy distribution and mass transport in stratified waterbodies, such as lakes and reservoirs (Wüest & Lorke, 2003; Lorke, 2007; Ivey *et al.*, 2008; Bouffard *et al.*, 2012). When waterbodies are large enough to be affected by the rotation of the Earth (Antenucci & Imberger, 2001), a wide variety of types of internal waves can coexist (Shimizu *et al.*, 2007), among which are the well-known Kelvin and Poincaré gravity waves (Csanady, 1967; Stocker & Imberger, 2003). Recent inviscid numerical studies (de la Fuente *et al.*, 2008, 2010; Sakai & Redekopp, 2010, 2011) have shown that in stratified lakes affected by background rotation, the nonlinear evolution of internal gravity waves is wave dependent: Kelvin waves can degenerate into a package of solitary-type waves, Poincaré waves show a periodic back-and-forth radiation of energy, and nonlinear interaction between Kelvin and Poincaré waves triggers the transfer of energy to

higher-frequency modes (de la Fuente *et al.*, 2010). These nonlinear processes are strongly influenced by the available potential energy (Horn *et al.*, 2001; Boegman *et al.*, 2005b). In addition, theoretical, numerical and recent experimental studies (Helfrich & Grimshaw, 2008; Grimshaw & Helfrich, 2008, 2012; Grimshaw *et al.*, 2013) have shown that, in the absence of lateral boundaries, the effect of the background rotation can strongly influence the evolution of solitary waves. The results show that the background rotation is responsible for the radiation of energy from the solitary waves to long inertial-gravity waves, giving rise the emergence of a new short solitary wave packet. However, these theoretical and numerical studies are based on inviscid assumptions, and they must be investigated from the experimental point of view, where viscous energy loss also occurs (Shimizu & Imberger, 2009, 2010).

Early experimental studies, performed by Maxworthy (1983), reported the formation of solitary-type waves in a two-layer stratified rotating channel. The celerity of solitary-type waves is independent of rotation and depends on only the stratification and wave amplitude. Furthermore, the wave amplitude decays exponentially across the channel, proportional to the internal Rossby ratio of deformation. Motivated by the experiments of Maxworthy (1983) experiments, Grimshaw (1985) derived the evolution equations for a weakly nonlinear internal Kelvin wave from a Korteweg-de Vries (KdV)-type equation, including the rotation effect. This theoretical result shows that in a strong rotating regime, the amplitude of the internal Kelvin wave at the wall is described by KdV theory, while its transverse structure is that of a linear internal Kelvin wave. Subsequent investigations found important similarities between solitary-type waves in a rotating frame and the solitary wave described by the KdV equation (Renouard *et al.*, 1987; Grimshaw *et al.*, 1998; Ostrovsky & Stepanyants, 2005; Helfrich & Melville, 2006). Moreover, Renouard *et al.* (1993) showed that the principal effects of weak rotation on the evolution of weakly nonlinear long waves are caused by the resonant interaction between Kelvin and Poincaré waves, previously described by Melville *et al.* (1989). Experimental studies conducted by Wake *et al.* (2004, 2005) analysed the energy dissipation of an internal wave field affected by rotation in a linear regime, showing that in the absence of topographic effects, it was controlled by viscous dissipation in the bottom Ekman layer.

The aim of this study is to analyse experimentally the free evolution of basin-scale internal gravity waves in a two-layer stratification, when nonlinear processes and background rotation are involved in the flow dynamics. We are particularly interested in (1) investigating the fundamental Kelvin wave response as a function of the initial displacement of the density interface, the aspect ratio of stratification and the background rotation; (2) characterizing the conditions in which it is possible to identify a nonlinear interaction among the fundamental modes of Kelvin waves and Poincaré waves; and (3) studying the influence of rotation, the aspect ratio of the stratification and the initial displacement of the density interface on the decay of the fundamental Kelvin wave. The conceptual model adopted by Csanady (1967, 1968) was used to develop the experimental facility and to characterize the initial internal gravity-wave field in a rotating cylindrical geometry with a two-layer stratified fluid.

Figure 3.2.1 shows a schematic of the conceptual model. The model defines the thickness and density of each layer (ρ_ℓ and h_ℓ, with $\ell = 1, 2$); the horizontal and vertical length scales, characterized by the diameter $D = 2R$ and the total depth $H = h_1 + h_2$, respectively; and the angular velocity $\Omega_z = f/2$ (in the direction of gravity), where f is the inertial frequency. From this set of parameters is defined the long internal gravity wave celerity $c_\mathrm{i} = \sqrt{g' h_1 h_2 / H}$, where $g' = (\Delta\rho/\rho_0)g$ is the reduced gravity, $\Delta\rho = \rho_2 - \rho_1$ is the density difference between the bottom and top layer, and ρ_0 is the ambient reference density. Csanady (1967) obtained the linear normal modes of the density interface, $\eta_\mathrm{i}(t, \vec{x})$, in the limit in which the internal Rossby radius of deformation $R_\mathrm{i} = c_\mathrm{i}/f$ is smaller than the radius of the

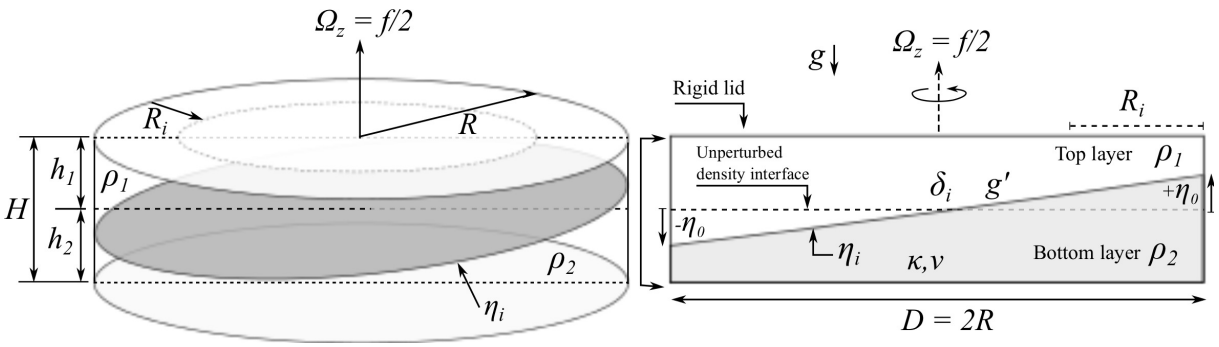

Figure 3.2.1: Schematic of the conceptual model and the experimental setup,. Figure exhibit the cylindrical domain and the physical parameters involved in the study and the theoretical initial condition of the density interface (dark gray colour), which is characterized by an initial vertical displacement η_0.

basin, R. In this context, the effect of the background rotation ($\Omega_z = f/2$) modulates the basin-scale internal wave dynamics. From this model, an analytical description of the Kelvin and Poincaré waves can be obtained. A Kelvin wave is a subinertial cyclonic boundary-trapped wave whose amplitude $\eta_i(t, \vec{x})$ decays exponentially from the horizontal boundary towards the centre of the domain, and its horizontal flow has a strong azimuthal component. A Poincaré wave is a superinertial anticyclonic wave characterized by a cell structure on the horizontal plane, whose maximum amplitude is located at the centre of the cell, and its horizontal flow has a strong radial component. For use henceforth, we define $\eta_0 = \max\{\eta_i(t = 0, \vec{x})\}$. Taking into account the physical parameters of the conceptual model and the fluid properties, a set of dimensionless numbers that allow the characterization of the behaviour of the basin-scale internal gravity waves are derived. In this study, the internal wave field is excited via an initial straight tilt of the density interface, and its temporal evolution is analysed in terms of three dimensionless parameters: the initial Wedderburn number $W_0 = h_1/(2\eta_0)$ (Horn *et al.*, 2001; Boegman *et al.*, 2005b), the aspect ratio of the stratification $h_* = h_1/H$ (Horn *et al.*, 2001) and the Burger number $S = R_i/R$ (Antenucci & Imberger, 2001). Here (W_0, h_*) and S describe the nonlinear response and the effect of the background rotation on the basin-scale internal gravity waves, respectively.

The outline of the paper is as follows. Section 3.2 presents the dimensionless parameters adopted to characterize the experimental sets, the dominant normal modes in a stratified cylindrical basin and the frequencies and characteristic time scales for studying the internal wave field. Section 3.3 presents the experimental facility, the set of conducted experiments, the data analysis used and a brief qualitative description of the results. In 3.4, the experimental results are analysed. First, the linear response of the internal gravity wave field is characterized. Second, the nonlinear response of the basin-scale waves is studied. Third, the parameters that control the bulk decay rate of the Kelvin wave are identified. Finally, 3.5 presents a discussion of the results and the conclusions of the investigation.

3.2 Dimensionless numbers, normal modes and time scales

3.2.1 Dimensionless numbers

First, this study assumes that the density interface is located below the mid-depth position (except when $h_1 = h_2$) so that the bottom layer is the thinner layer, contrary to what is usually observed in most lakes. Similarly to the laboratory experiments performed by Horn *et al.* (2001), this inverse condition does not alter the physics of the problem because the experimental tank uses a rigid lid on top of the water column (see figure 3.2.2). It allows better experimental measurements of the density interface to be obtained because of the optical method used, which is explained in 3.3. Therefore, henceforth, the following definitions of dimensionless parameters are used to describe this reverse stratification type.

The flow of the basin-scale internal gravity waves is characterized by the parameters presented in the conceptual model (see figure 3.2.1), specifically, by the following set: $\{R_\mathrm{i}, R, h_1, H, \eta_0, g', \nu, \kappa\}$. From this set, six dimensionless parameters are obtained, which the authors have chosen as follows.

The first dimensionless parameter is the Burger number (Antenucci & Imberger, 2001), defined as the ratio between the internal Rossby radius of deformation, $R_\mathrm{i} = c_\mathrm{i}/f$, and the length scale of the water basin, or the radius of the cylindrical basin, R, so that

$$S = \frac{R_\mathrm{i}}{R}. \tag{3.2.1}$$

This parameter quantifies the influence of the background rotation on the basin-scale internal gravity waves. In the laboratory experiments, the inertial frequency f is controlled by the angular velocity $\Omega_z = f/2$. The basin-scale internal gravity waves are affected by the background rotation when $0 < S < 1.0$, and the rotation influence increases as $S \to 0$ (Antenucci & Imberger, 2001). However, when $S \geq 1$, the rotation effects are weak.

The second dimensionless parameter is the initial Wedderburn number (Horn *et al.*, 2001; Boegman *et al.*, 2005b), defined as the ratio of the unperturbed thickness bottom layer, h_1, to twice the initial vertical displacement of the density interface, η_0:

$$W_0 = \frac{h_1}{2\eta_0}. \tag{3.2.2}$$

Here, the initial Wedderburn number is a measure of the initial available potential energy attributed to the initial straight tilt of the density interface. If $0 \leq \eta_0 \leq h_1$, then $0.5 \leq W_0 \leq \infty$, where $W_0 \to \infty$ denotes null initial available potential energy, whereas $W_0 = 0.5$ denotes the upwelling (or downwelling, for our experiments) condition of the density interface, which is associated with the maximum initial available potential energy for a specific h_1.

The third dimensionless parameter seeks to quantify the steepening of the basin-scale internal gravity waves, henceforth denoted by $\mathcal{C}_s$. This parameter is defined as the ratio of the linear long internal wave celerity, c_i, to the nonlinear internal wave celerity $c_{nl} = \eta_0\alpha_1$ derived from the KdV theory (Horn *et al.*, 2001; Boegman *et al.*, 2005b), where $\alpha_1 = (3/2)c_\mathrm{i}(H - 2h_1)/\{h_1(H - h_1)\}$ is the KdV nonlinear coefficient (Helfrich & Melville, 2006). Here $\mathcal{C}_s$ may be expressed in terms of W_0 and

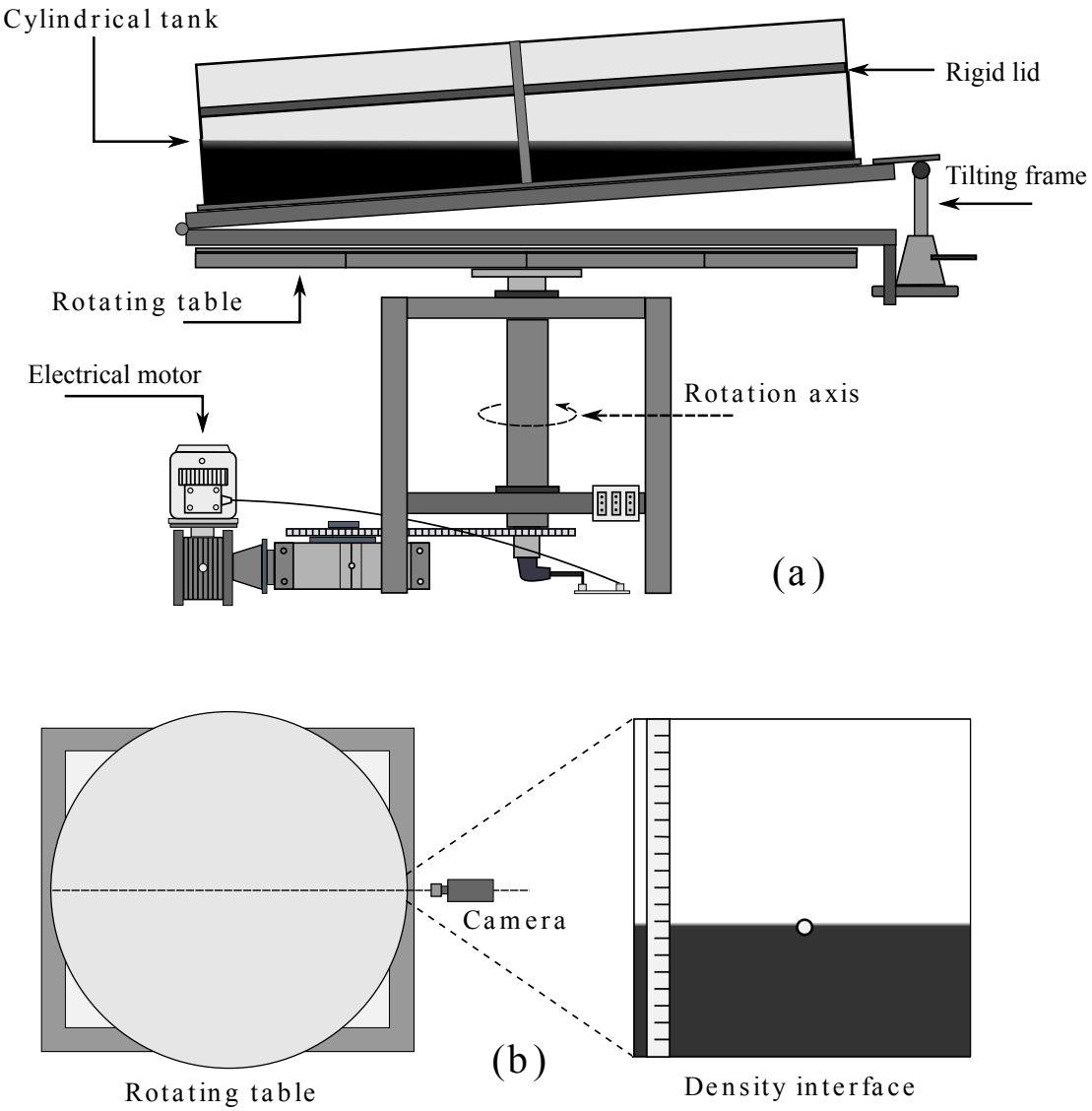

Figure 3.2.2: Experimental facility of the rotating turntable system.

the aspect ratio of the stratification $h_* = h_1/H$ as follows:

$$\mathcal{C}_s = \frac{c_\mathrm{i}}{\eta_0 \alpha_1} = \frac{2W_0}{3}\frac{1-h_*}{1-2h_*}. \tag{3.2.3}$$

As W_0 and h_* decrease, $\mathcal{C}_s$ decreases to a limiting value of $\mathcal{C}_s = 1/3$. In the range $(1/3) < \mathcal{C}_s < 1$, the nonlinear celerity c_{nl} is higher than the linear celerity c_i; hence, nonlinear steepening of the basin-scale internal gravity waves is expected, and this effect increases as $\mathcal{C}_s \to 1/3$. In contrast, when $\mathcal{C}_s \geq 1$, steepening takes too long to play an important role in the evolution of internal waves. This regime is related to two conditions: $\eta_0 \approx 0$ or $h_1 \approx h_2$. Consequently, if the initial Wedderburn number is set to a constant value, the nonlinear steepening may be controlled via the aspect ratio h_*; the nonlinear processes affecting the basin-scale internal gravity waves will increase as $h_* \to 0$ (Horn *et al.*, 2001).

The fourth dimensionless parameter is the Reynolds number, defined as follows:

$$Re = \frac{\eta_0 c_i}{\nu}, \tag{3.2.4}$$

where ν is the kinematic viscosity. In our experiments, $Re \sim \mathcal{O}(10^3)$.

Because a saline stratification is used, the fifth dimensionless parameter is the Schmidt number:

$$Sc = \frac{\nu}{\kappa}, \tag{3.2.5}$$

where κ is the mass diffusivity coefficient. In our experiments $Sc \approx 700$.

The last dimensionless parameter is the basin aspect ratio (Sakai & Redekopp, 2010), defined as the ratio of the vertical (λ_v) to the horizontal (λ_h) length scales of the basin-scale waves:

$$\Lambda = \frac{\lambda_v}{\lambda_h} = \frac{H}{2R} \tag{3.2.6}$$

where $2R$ is the diameter, D, of the cylindrical basin. In our experiments, $\Lambda \sim \mathcal{O}(10^{-2})$. This parameter is a measure of the hydrostaticity of the basin-scale waves. However, this flow characteristic does not mean that the vertical acceleration will always be small; nonlinear processes (steepening, breaking, dispersion) may transfer energy from large scales ($\sim \lambda_h$) to smaller scales ($\sim \lambda_v$), so that the horizontal and vertical wave length scales may be of the same order, thereby causing the hydrostatic pressure hypothesis to be invalid (de la Fuente *et al.*, 2008, 2010).

3.2.2 Normal modes in a stratified cylindrical basin

We are interested in identifying the presence of Kelvin and Poincaré waves in an internal wave field developed in a cylindrical domain with a two-layer stratified fluid. Csanady (1967) studied linear dynamics of the rotating internal gravity waves in a two-layer cylindrical basin via the analysis of natural normal modes derived from the linear hydrostatic inviscid equation of motion and continuity:

$$\frac{\partial}{\partial t}\begin{pmatrix} U_r \\ U_\theta \end{pmatrix} + \begin{pmatrix} -U_\theta \\ U_r \end{pmatrix} - \nabla_H \eta_i = 0, \tag{3.2.7}$$

$$\frac{\partial \eta_i}{\partial t} + \frac{1}{r}\left\{\frac{\partial (rU_r)}{\partial r} + \frac{\partial U_\theta}{\partial \theta}\right\} = 0. \tag{3.2.8}$$

These equations are presented in their dimensionless form ($*$ in the superscript indicates a dimensional variable only for velocities, time, radial coordinate and displacement of density interface), where $(U_r, U_\theta) = (U_r^*, U_\theta^*)c_i^{-1}$ are the radial and azimuthal velocity components, $t = t^* f$ is the time, $r = r^* R_i^{-1} \in [0, S^{-1}]$ is the radial coordinate, $\theta \in [0, 2\pi]$ is the azimuthal coordinate, $\nabla_H = R_i \nabla^*$ is the horizontal gradient, and $\eta_i = \eta_i^*/h_1$ is the dimensionless vertical displacement of the density interface. This model supposes that there is no flux through the walls as a boundary condition (Csanady, 1967). From the momentum equation (3.2.7), the continuity equation (3.2.8) and the boundary condition, one

can derive the boundary condition for η_{i} (Csanady, 1967):

$$\frac{\partial^2 \eta_{\mathrm{i}}}{\partial r \partial t} + \frac{1}{r}\frac{\partial \eta_{\mathrm{i}}}{\partial \theta} = 0 \ \text{ at } r = S^{-1}. \tag{3.2.9}$$

To obtain the radial and azimuthal structure of the first baroclinic normal mode, it is assumed that η_{i} has the following modal pressure form:

$$\eta_{\mathrm{i}} = \mathcal{R}(r)\cos\left(\theta \cdot n_\theta - \sigma t\right), \tag{3.2.10}$$

where $\mathcal{R}(r)$ is an arbitrary radial function of the modal pressure, $n_\theta \in \{1, 2, 3, ...\}$ is the azimuthal mode, and $\sigma = \omega/f$ and ω are the dimensionless and dimensional wave frequencies, respectively. We are looking for periodic solutions in θ. The radial structure of the modal pressure satisfies the wave equation:

$$\frac{\partial^2 \mathcal{R}}{\partial r^2} + \frac{1}{r}\frac{\partial \mathcal{R}}{\partial r} + \left(\sigma^2 - 1 - \frac{n_\theta^2}{r^2}\right)\mathcal{R} = 0. \tag{3.2.11}$$

Equation (3.2.11) is a Bessel equation if $\sigma^2 - 1 > 0$ and is a modified Bessel equation if $\sigma^2 - 1 < 0$. The solutions of theses equations are traditionally denoted by J and I, respectively. Hence, the solution of $\mathcal{R}$ depends on σ and n_θ:

$$\mathcal{R}_{n_\theta} = \begin{cases} I_{n_\theta}\left(r\sqrt{|\sigma^2 - 1|}\right), & \sigma^2 - 1 < 0, \\ J_{n_\theta}\left(r\sqrt{|\sigma^2 - 1|}\right), & \sigma^2 - 1 > 0. \end{cases} \tag{3.2.12}$$

Two types of gravity-wave modes are obtained from these equations: for subinertial frequencies ($\sigma^2 - 1 < 0$), the solutions are cyclonic Kelvin waves (Antenucci & Imberger, 2001), while for superinertial frequencies ($\sigma^2 - 1 > 0$), the solutions are anticyclonic Poincaré waves, higher azimuthal Kelvin wave and other radial modes (Antenucci & Imberger, 2001; Stocker & Imberger, 2003). In general, the horizontal structure of these modes can be characterized by the Burger number. Each type of wave is characterized by a radial-mode component and an azimuthal-mode component, $M(n_r, n_\theta)$, where n_r denotes the radial mode number. Hereafter, Kelvin or cyclonic modes (Antenucci & Imberger, 2001) are denoted by $K(n_r, n_\theta)$, Poincaré or anticyclonic modes (Antenucci & Imberger, 2001) are denoted by $P(n_r, n_\theta)$.

As we know the radial structure $\mathcal{R}_{n_\theta}$, we use equation (3.2.9) to calculate the theoretical natural frequencies σ of each type of wave:

$$S^{-1}\sqrt{|\sigma^2 - 1|}\mathcal{R}_{n_\theta - 1}\left(S^{-1}\sqrt{|\sigma^2 - 1|}\right) + n_\theta\left(\sigma^{-1} - 1\right)\mathcal{R}_{n_\theta}\left(S^{-1}\sqrt{|\sigma^2 - 1|}\right) = 0. \tag{3.2.13}$$

This result is useful for identifying the types of basin-scale internal gravity waves presented in a spectral signature (Wake *et al.*, 2005). Figure 3.2.3 shows the interface displacement of the main modes $M(n_r, n_\theta)$ of the internal gravity waves, along with corresponding symbols (triangles, circles, diamonds, squares), which will be used later in the experimental results presented in section 3.3. The internal wave field is excited by an initial straight tilt of the density interface (see figure 3.2.1). This initial condition excites all radial modes and the first azimuthal mode (Stocker & Imberger, 2003).

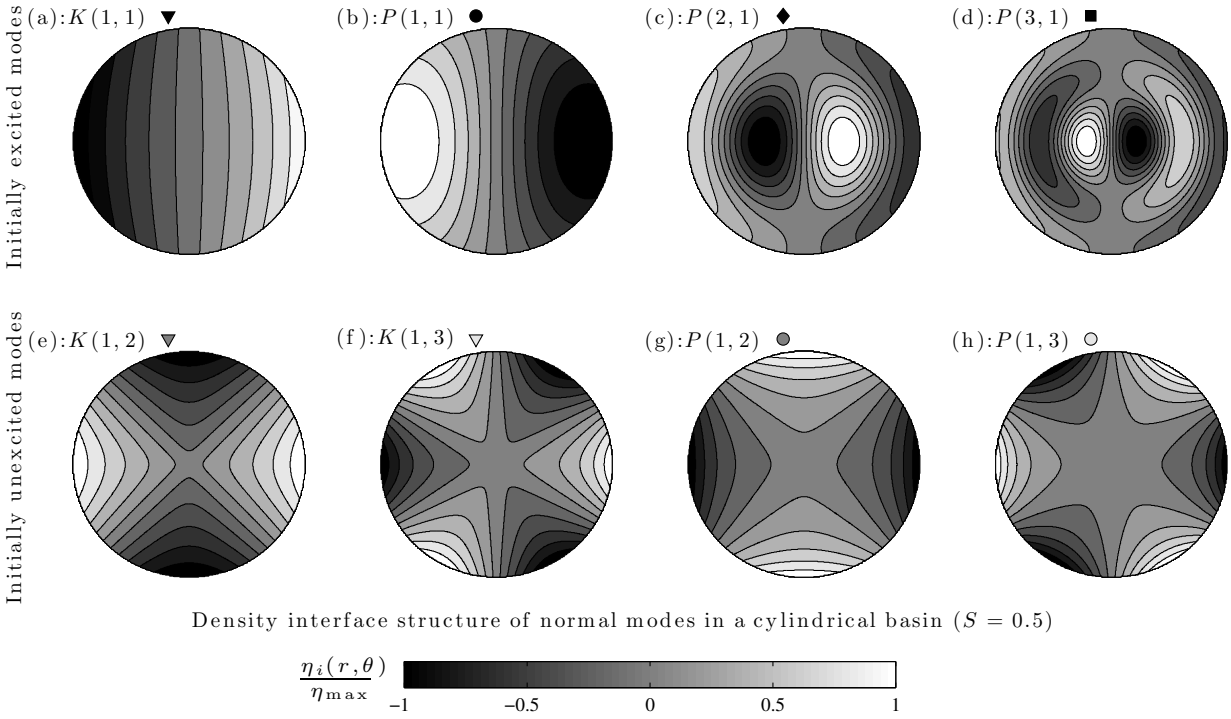

Figure 3.2.3: Spatial structure of the density interface $\eta_{\rm i}(r,\theta)/\eta_0$ of the main initially excited modes (top row) and unexcited modes (bottom row).

3.2.3 Frequency/time scales

First, we use the theoretical frequencies derived from equation (3.2.13) to identify the fundamental modes of the Kelvin and Poincaré waves, whose dimensionless frequencies are denoted by $\sigma_k = \omega_k/f$ and $\sigma_p = \omega_p/f$, respectively, where ω_k and ω_p are their dimensional frequencies, respectively.

Second, the nonlinear interaction between waves of frequencies σ_k and σ_p produces two characteristic frequencies $\sigma_k \pm \sigma_p$ (Hammack & Henderson, 1993). These type of characteristic frequencies have been called Kelvin–Poincaré waves, $\sigma_{kp} = \sigma_p + \sigma_k$, and Poincaré–Kelvin waves, $\sigma_{pk} = \sigma_p - \sigma_k$, respectively (de la Fuente *et al.*, 2008). Their existence in the frequency spectrum is attributable to nonlinear processes involving Kelvin and Poincaré waves.

Third, the time scale associated with the emergence of nonlinear steepening of internal Kelvin waves may be studied in terms of the steepening time scale, T_s, derived from the KdV theory (Horn *et al.*, 2001; Boegman *et al.*, 2005a; de la Fuente *et al.*, 2008) and the Kelvin wave period:

$$\tau_s = \frac{T_s}{T_k}, \tag{3.2.14}$$

where $T_s = 2\pi R/(\eta_0\alpha_1)$, and $T_k = 2\pi R/\omega_k$ is the Kelvin wave period. It is observed that if $h_* \to 0.5$ ($h_1 \to h_2$), then $\tau_s \to \infty$, so the steepening of internal gravity waves it is not expected. A similar dimensional analysis can be performed for the nonlinear behaviour of the fundamental Poincaré wave.

Finally, a dimensionless time scale associated with the bulk decay rate of the vertical displacement,

τ_{d}, of a specific internal gravity wave can be described using the ratio $\tau_{\mathrm{d}} = T_{\mathrm{d}}/T_{\mathrm{i}}$, where T_{d} is a decay time scale obtained from experimental measurements of $\eta_{\mathrm{i}}(t)$ associated with the internal gravity waves. The aim is to quantify the decay rate of the fundamental Kelvin wave; therefore, the following ratio is considered:

$$\tau_{\mathrm{d}k} = \frac{T_{\mathrm{d}}}{T_k} \tag{3.2.15}$$

Lower values of $\tau_{\mathrm{d}k}$ imply greater decay of the fundamental Kelvin wave in one period.

3.3 Methods

3.3.1 Experimental set-up

The experimental study was conducted on a rotating table whose rotation speed varied between 0 and 6 rpm (figure 3.2.2). On top of the rotating table was mounted a circular tank made of transparent acrylic glass, with a diameter of 1.8 m. The rotating table was set up with a frame that can be tilted and then released into the horizontal position in a very short time ($t_r \sim 1$ s). This time scale is one or two orders of magnitude smaller than the period of the waves of interest.

A two-layer stratification was created inside this experimental tank using a freshwater layer with density ρ_1 on top and a dyed saltwater layer of density ρ_2 on the bottom, with a characteristic density difference $\Delta\rho = \rho_2 - \rho_1$. To create the two-layer system, the salt water was first placed in the tank, and fresh water was then gently poured on top of the saltwater layer through a low-porosity sponge, which is required to reduce vertical mixing. Finally, a rigid lid closed the free surface of the water to prevent the generation of barotropic waves. In this step, the aspect ratio of the stratification, h_*, was defined.

The initial thickness of the density interface, δ_{i}, was estimated optically to be $\delta_{\mathrm{i}} \approx 1.0$ cm (± 0.05 cm); its thickening because of vertical mass diffusion has a characteristic time scale $T_{m\mathrm{d}}$, which is much longer than the time scale of the internal gravity waves of interest, T_k, and the measurement time, T_r:

$$T_{m\mathrm{d}} \sim \left(\frac{\delta_{\mathrm{i}}^2}{\kappa}\right) > T_r \sim 10 T_k, \tag{3.3.1}$$

where the mass diffusion coefficient for salt water is $\kappa \sim 10^{-9}$ m^{2}s^{-1} (Csanady, 1975), leading to $T_{m\mathrm{d}} \sim 10^5$ s, while the measurement time is $T_r \approx 5 \times 10^2$ s, and the Kelvin wave period, T_k, takes values between 40 s and 80 s, depending on the set of parameters used. Therefore, the thickness of the density interface achieved during an experiment is $\delta_{\mathrm{i}} \ll H$, even if turbulent mixing affects the density interface. If we increase the effective diffusivity to 100κ, then $T_{m\mathrm{d}} \geq T_r$. Consequently, the vertical mass diffusion present in the experiments does not affect the conceptual problem of the two-layer flow.

Once the two-layer stratification was created, each experiment was conducted in two steps. First, the desired Burger and the initial Wedderburn numbers for the experiment were set. The Burger number was achieved by gradually increasing the angular velocity until the desired value of Ω_z was obtained. This process was executed slowly to avoid high azimuthal accelerations ($t \sim 1 - 2$ hrs). Afterwards, to achieve the initial Wedderburn number, the density interface was gradually tilted with respect to the horizontal bottom tank direction (see Horn *et al.*, 2001; Boegman *et al.*, 2005b); this

displacement was induced using a mechanical arm located at the edge of the frame (see figure 3.2.2). Gentle operation of the table was required to avoid significant accelerations of the flow that would induce vertical mixing. Second, once the dimensionless numbers (h_*, S, W_0) were set, the experiment was begun by suddenly releasing the tank, allowing it to return to the horizontal position, which induced an adjustment of the interface as well as the excitation of all radial modes and only the first azimuthal mode of the internal gravity waves.

The vertical response and free evolution of the density interface was captured using a video camera that rotated with the table. It was located in the zone where the initial vertical displacement was $-\eta_0$ with respect to the equilibrium position, so the density interface is close to the bottom boundary of the tank (see figure 3.2.1). The video camera was programmed to measure one frame per second ($f_r = 1$ Hz), because our interest was to record internal gravity waves whose frequencies are in the range $\omega \sim [O(10^{-1}), O(10^{-2})]$ Hz. The video camera image resolution was 512×512 pixels, with a recording area that covered the entire range of vertical displacements of the density interface (approximately 10 cm). As the salt water was dyed and the fresh water was not, the registered images were composed of two colours: black and white. The pycnocline was located at the boundary between the two colours. The accuracy of the measurements was ± 0.05 cm.

3.3.2 Experimental set

The physical variables to be controlled were the initial thicknesses of the bottom layer and top layer, h_1 and h_2; the initial vertical displacement of the density interface, η_0; the relative density between the top layer and the bottom layer, $\varepsilon = \Delta\rho/\rho_1$; the radius of the circular tank, R; and the inertial frequency $f = 2\Omega_z$. Using these external variables, the six dimensionless parameters were controlled. However, the focus of this study is the following three parameters: W_0, $\mathcal{C}_s(W_0, h_*)$ and S. A total of 26 experiments were conducted, and Table 3.1 summarizes the experimental conditions of each one.

The experiments were grouped into three sets. Set 1 contains 16 experiments and was conducted to analyse the influence of the background rotation on a nonlinear internal wave field. In set 1, $h_* \approx 0.2$ and $S \in (0.2 - 0.8) \cup \infty$ ($S \to \infty$ when $f \to 0$), and two different values of the initial Wedderburn number, $W_0 = 0.5$ and $W_0 = 1.0$, were used for each Burger number.

Set 2 contains 10 experiments and was conducted with the objective of studying the response of the density interface for different aspect ratios in the range $h_* \in (0.09 - 0.53)$. Using this set of experiments, the influence of the aspect ratio on the nonlinear behaviour of the basin-scale internal gravity waves was analysed.

Set 3 contains three experiments. Its intent is to study the influence of the background rotation on the decay rate in the absence of nonlinear steepening in basin-scale internal gravity waves. In this set, $h_* \approx 0.5$, $W_0 = 1.0$ and the Burger number was in the range of $S \in (0.2 - 0.8)$.

3.3.3 Data analysis

The internal gravity wave field was studied via the analysis of the time series of the perturbed density interface at the boundary, $\eta_{\mathrm{i}}(t_n)$. The energy and frequency properties of the main internal gravity waves excited in the experiments were analysed using the power spectral density (PSD) function via

Set n.	Run n.	h_1 (cm)	h_2 (cm)	η_0 (cm)	ε (%)	c_i (cm/s)	f (hz)	h_* (-)	W_0 (-)	$\mathcal{C}_s$ (-)	S (-)	$R\mathrm{e}$ (-)
	1.1	4.5	19.5	2.3	1.96	8.39	0.46	0.19	1.0	0.87	0.20	1887
	1.2	5.0	19.0	5.0	1.96	8.73	0.46	0.21	0.5	0.45	0.21	4363
	1.3	4.1	20.0	2.1	1.96	8.09	0.30	0.17	1.0	0.84	0.30	1658
	1.4	4.5	19.5	4.5	1.96	8.39	0.30	0.19	0.5	0.43	0.31	3774
	1.5	5.0	19.0	2.5	1.96	8.73	0.21	0.21	1.0	0.90	0.46	2181
	1.6	5.5	18.5	5.5	1.96	9.03	0.21	0.23	0.5	0.47	0.48	4967
	1.7	4.5	19.5	2.3	1.96	8.39	0.21	0.19	1.0	0.87	0.45	1887
1^{st}	1.8	4.5	19.5	4.5	1.96	8.39	0.21	0.19	0.5	0.43	0.46	3774
	1.9	4.5	19.0	2.3	1.96	8.37	0.18	0.19	1.0	0.87	0.52	1882
	1.10	5.0	19.0	5.0	1.96	8.73	0.18	0.21	0.5	0.45	0.54	4363
	1.11	4.5	19.5	2.3	1.96	8.39	0.15	0.19	1.0	0.87	0.63	1887
	1.12	4.0	20.0	4.0	1.96	8.01	0.15	0.17	0.5	0.42	0.60	3203
	1.13	4.0	20.0	2.0	1.96	8.01	0.11	0.17	1.0	0.83	0.80	1601
	1.14	4.0	19.0	4.0	1.96	7.97	0.11	0.17	0.5	0.42	0.80	3189
	1.15	4.0	20.0	2.0	1.96	8.01	0.00	0.17	1.0	0.83	∞	1601
	1.16	4.5	19.5	4.5	1.96	8.39	0.00	0.19	0.5	0.43	∞	3774
	2.1	2.5	21.5	2.5	1.96	6.56	0.21	0.10	0.5	0.38	0.35	1641
	2.2	2.2	21.8	1.1	1.96	6.20	0.21	0.09	1.0	0.74	0.33	682
	2.3	4.5	19.5	2.3	1.96	8.39	0.21	0.19	1.0	0.87	0.45	1887
	2.4	4.5	19.5	4.5	1.96	8.39	0.21	0.19	0.5	0.43	0.46	3774
2^{nd}	2.5	6.5	17.5	6.5	1.96	9.55	0.21	0.27	0.5	0.53	0.51	6206
	2.6	6.5	17.5	3.3	1.96	9.55	0.21	0.27	1.0	1.06	0.51	3103
	2.7	8.0	16.0	8.0	1.96	10.13	0.21	0.33	0.5	0.67	0.54	8103
	2.8	8.0	16.0	4.0	1.96	10.13	0.21	0.33	1.0	1.33	0.54	4051
	2.9	7.5	7.5	7.5	1.96	8.49	0.21	0.50	0.5	∞	0.45	6370
	2.10	8.0	7.0	4.0	1.96	8.47	0.21	0.53	1.0	4.67	0.45	3390
	3.1	8.0	7.0	4.0	1.96	8.47	0.47	0.53	1.0	4.67	0.20	3390
3^{rd}	3.2	8.0	7.0	4.0	1.96	8.47	0.21	0.53	1.0	4.67	0.45	3390
	3.3	7.5	7.5	3.8	1.96	8.49	0.12	0.50	1.0	∞	0.80	3003

Table 3.1: Experimental set.

finite Fourier transforms (FFTs) (e.g., Bendat & Piersol, 2000):

$$\hat{G}_{\eta_i}(f_k) = \frac{2}{T_r} \sum_{\ell=0}^{N_s-1} |\hat{\Pi}_{\eta_i}(\omega_\ell, T_r)|^2, \tag{3.3.2}$$

where N_s is the number of samplings in T_r; $\omega_\ell = \ell/N_s$ is the ℓth discrete frequency calculated using $\ell = 0, 1, ..., [N_s/2 - 1]$; and $\hat{\Pi}_{\eta_i}(\omega_\ell, T_r)$ is the discrete spectral signal obtained by applying the discrete FFT to $\eta_i(t_n)$ over the recording length T_r. To use the PSD, it is necessary to have a periodic or quasi-periodic signals (Garcia *et al.*, 2005), and two tests were used to validate the use of PSD on the measured time series. (i) The frequency under study, ω_m, was identified, and the PSD was computed for various sampling frequencies in the range $\omega_s \geq 2\omega_m$. For each PSD, the frequency of the studied signal was identified, and if it did not vary as a function of ω_s it was concluded that this mode had periodic characteristics. If ω_m changed with ω_s but by less than 10%, it was considered a quasi-periodic type wave, for which the PSD is an acceptable tool. In any other case, the PSD is a useless tool. (ii) The time series was divided into several segments, and the PSD was computed in each segment. The studied signal was again identified, and the same criterion used for test (i) was considered to define whether the PSD could be used to study the measured time series. For the first test, the used sampling frequencies were $\omega_s = 1$, 0.5 and 0.1 Hz, and percentage changes between 0 and 3.98 % were obtained for ω_m. Two segments were used for the second test ($0 : T_r/2$, $T_r/2 : T_r$), and percentage changes between 0 and 9.86 % were obtained for ω_m. The results demonstrated that the frequencies of the dominant energy peaks are quasi-invariant, thereby establishing that the PSD could be used to identify the frequencies of the large-scale internal gravity waves.

A normal mode identified by the PSD has an associated frequency and an associated amount of energy, which can be analysed using a band-pass decomposition around the frequency that defines its energy peak in the spectral signal. The spectral signal of the specific normal mode is obtained by multiplying $\hat{\Pi}_i(\omega_\ell)$ by the frequency response function, H_m, of the band-pass filter:

$$\hat{\Pi}_{\eta_m}(\omega_\ell) = H_m(\omega_\ell)\hat{\Pi}_{\eta_i}(\omega_\ell), \tag{3.3.3}$$

where the frequency response function is a linear superposition of two discrete Heaviside functions:

$$H_m(\omega_\ell) = \mathcal{H}(\omega_\ell - \omega_m^{(l)}) - \mathcal{H}(\omega_\ell - \omega_m^{(u)}), \tag{3.3.4}$$

with

$$\mathcal{H}(\omega_\ell - \omega_*) = \begin{cases} 0 & \omega_\ell < \omega_*, \\ 1 & \omega_\ell \geq \omega_*, \end{cases} \tag{3.3.5}$$

whose resonant frequency is ω_m, and its characteristic bandwidth is $B_m = \omega_h - \omega_l$, where $\omega_m^{(u)} = \omega_m + B_m/2$ is the upper cut-off frequency, and $\omega_m^{(l)} = \omega_m - B_m/2$ is the lower cut-off frequency. The frequency band that characterizes the energy content of an internal gravity wave is therefore $\left[\omega_m^{(l)}, \omega_m^{(u)}\right]$. Following Bendat & Piersol (2000), this bandwidth can be defined with the quadratic bias error of the PSD estimator taken into consideration, which provides:

$$B_m \approx c \left(\frac{\omega_m^4}{T_r}\right)^{1/5} \tag{3.3.6}$$

where $c \approx 1.18$. Then, a synthetic time series associated with ω_m can be obtained by taking the real

part of the inverse FFT formula of $\hat{\Pi}_{\eta_m}$:

$$\eta_m(t_n) = \Re\left\{\frac{1}{N_s}\sum_{\ell=0}^{N_s-1}\hat{\Pi}_{\eta_m}(\omega_\ell)\exp\left(j\frac{2\pi n\omega_\ell}{N_s}\right)\right\} \tag{3.3.7}$$

where $\eta_m(t_n)$ is the discrete vertical displacement of the oscillation mode m, and j is the complex unit. This method makes it possible to isolate the temporal evolution of a single normal mode.

It is noteworthy that in the experiments only the interface displacement signals at the tank perimeter are measured and used for the analysis. This implies that only the Kelvin wave modes, of radial mode one, can be associated with their maximum energy amplitude in the PSD. However, although Poincaré modes can be identified in the spectral signal, these are not associated to their maximum energy amplitudes, because their maximum vertical displacements are located in the off-shore region.

3.3.4 Preliminary description of measurements

Representative results obtained from each experimental set are shown in figures 3.3.1, 3.3.2 and 3.3.3. The left column of each figure shows the measured vertical displacements of the density interface as a function of time, while the right column shows the corresponding PSD.

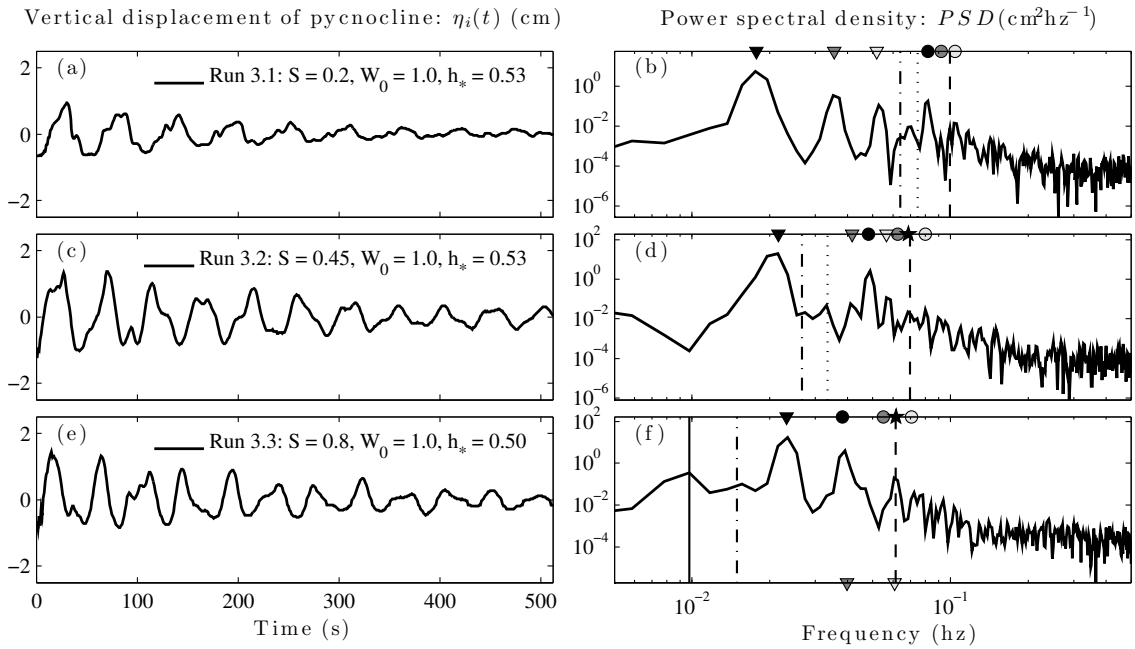

Figure 3.3.1: Representative results of set 3: left panels present time series of the vertical displacement of the density interface, $\eta_i(t)$, whereas right panels present the PSD of $\eta_i(t)$. The triangles and the circles identify the Kelvin and Poincaré waves, respectively (see Symbols presented in figure 3.2.3. Furthermore, the dot line marks the inertial frequency, f, the dashed line marks the theoretical position of the Kelvin–Poincaré frequency ω_{kp}, the dot-dashed line marks the theoretical position of the Kelvin–Poincaré frequency ω_{pk}, and the continuos line denotes an unclassified lowest frequency.

Figure 3.3.1 shows results from set 3 of experiments, which had a steepening parameter $\mathcal{C}_s > 1$

($h_* \approx 0.5$), so the linear response of the basin-scale internal waves is expected. In fact, the time series of $\eta_i(t)$ (figures 3.3.1$a, c,$ e) exhibit damped oscillatory waves with no evidence of steepening. However, higher azimuthal Kelvin modes are clearly identified of Figure 3.3.1(b) (grey and white triangles), which, according to de la Fuente *et al.* (2010), indicates the steepening of the Kelvin wave. This apparent contradiction is because the $\mathcal{C}_s$ is defined based on the first-order nonlinear terms, whereas in the presence of large vertical displacements of the density interface, higher-order nonlinear effects may become important (see the extended KdV equation in, e.g., Helfrich & Melville (2006)). More discussion on this aspect is provided in subsection 3.4.4.

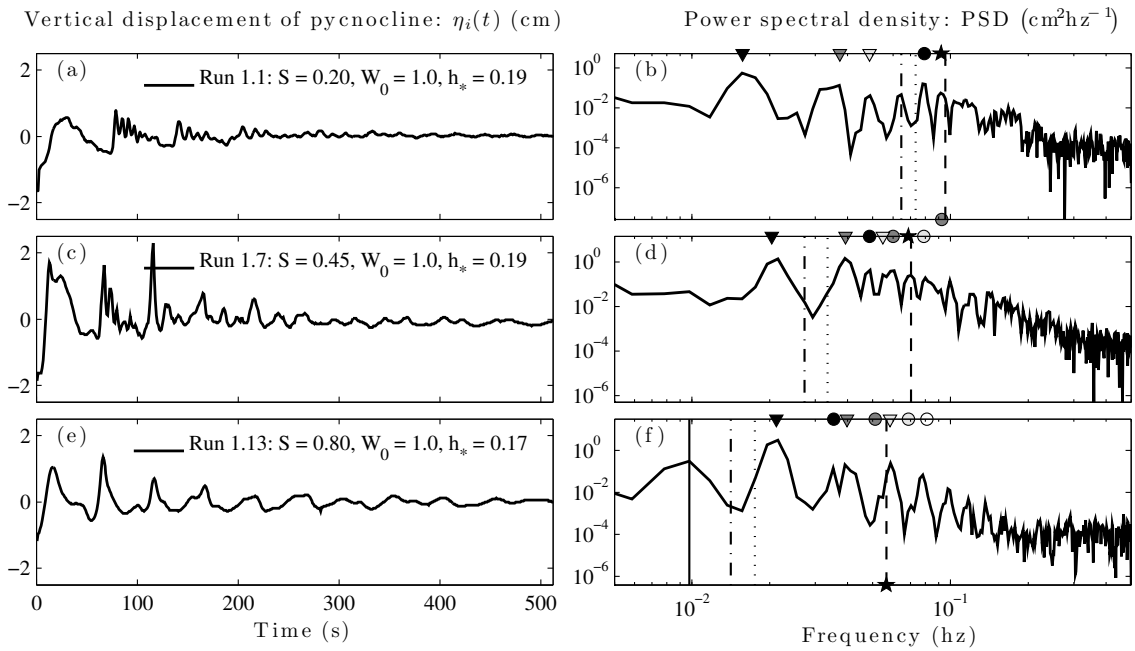

Figure 3.3.2: Representative results of set 1: idem to figure 3.3.1.

Figure 3.3.2 shows results from the set 1 of experiments, which had an aspect ratio of $h_* \approx 0.2$ and a steepening parameter $\mathcal{C}_s < 1$, so nonlinear response of the basin-scale internal waves is expected. The time series of $\eta_i(t)$ exhibits a strong steepening of the wave front in the first three periods. Moreover, figures 3.3.2a ($S = 0.20$) and 3.3.2c ($S = 0.45$) show that, after the first period, the wave front is followed by a train of waves. This is the result of the balance between nonlinear steepening and non-hydrostatic acceleration, which causes the dispersion of the main wave into a package of solitary-type waves. However, there is no evidence of wave dispersion in the time series with $S = 0.8$ (see figure 3.3.2e). In general, we observe that as S decreases, the number of solitary waves (in the tail) increases. These results suggest that rotation promotes the formation of KdV-type undular bore structures (EI *et al.*, 2005, 2006; Kamchatnov *et al.*, 2012), as it is shown in the top two panels of figure 3.3.2. However, recent studies have shown that the background rotation inhibits the existence of permanent solitary-type wave solution (Helfrich & Grimshaw, 2008; Grimshaw & Helfrich, 2008, 2012) and undular bore structures (Grimshaw *et al.*, 2012; Johnson & Grimshaw, 2013); this apparent contradiction may be due to a time-scale effect: while rotation inhibits the existence of permanent solitary-type wave solution (Helfrich & Grimshaw, 2008; Grimshaw & Helfrich, 2008), the steepening of the Kelvin wave and its subsequence degeneration in a train of undular bore may operate in a much smaller time scale. Further theoretical studies are required to elucidate this apparent contradiction, which was also discussed in de la Fuente *et al.* (2008). In addition, the PSDs of figure 3.3.2 exhibit

a wide range of frequencies associated with important energy peaks of higher azimuthal modes of Kelvin and Poincaré waves (grey and white triangles/circles). In addition, it is observed that the Kelvin–Poincaré frequency, $\omega_{kp} = \sigma_{kp} f$, is correlated with an energy peak (dashed line) and the internal mode $M(1,0)$ ($\star$), which is characterized as well as discussed in subsection 3.4.2. Moreover, the PSD of figure 3.3.2(f) exhibits an energy peak whose frequency (marked with a black solid line) is lower than the lowest Kelvin mode $K(1,1)$.

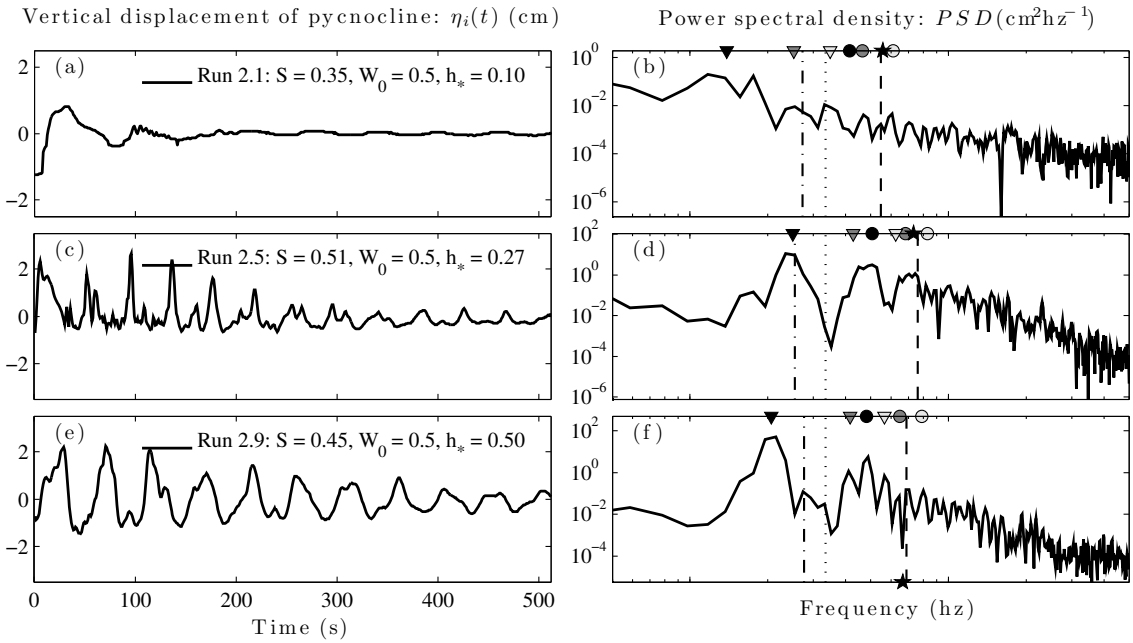

Figure 3.3.3: Representative results of set 2: idem to figure 3.3.1.

Finally, figure 3.3.3 presents the results of set 2 of experiments, which exhibit important differences among themselves. The time series with $h_* = 0.10$ (see figure 3.3.3a) exhibits an intensive degenerative and damping evolution of the large-scale internal gravity wave in the first wave periods, and after approximately the fourth period, $\eta_i(t)$ exhibits a small-amplitude linear seiche. However, the time series with $h_* = 0.27$ (see figure 3.3.3c) indicates that large-scale internal gravity waves are affected by nonlinear steepening and non-hydrostatic dispersion in the first three wave periods, with high wave amplitudes throughout the first six wave periods. After that, a damped linear seiche is observed. In contrast, the time series with $h_* = 0.53$ (see figure 3.3.3e) does not show evidence of steepening or non-hydrostatic dispersion of the internal waves. In contrast to the results shown in figures 3.3.3(a) and 3.3.3(c), the decay of $\eta_i(t)$ is weak. The PSDs of figure 3.3.3 exhibit important contrasts; the PSD of figure 3.3.3(b) exhibits energy peaks in a wide range of frequencies, with a poorly defined energy peak at the $K(1,1)$ frequency. Moreover, the PSDs of figures 3.3.3(d) and 3.3.3(f) indicate that most of the energy of the internal wave field is contained in the $K(1,1)$ and $P(1,1)$ frequencies, but weaker energy peaks associated with higher azimuthal modes of Kelvin and Poincaré waves are also observed.

3.4 Results

3.4.1 Internal gravity wave field

The PSD of the experimental time series of the interface displacement (e.g. Bendat & Piersol, 2000; Garcia *et al.*, 2005) was computed and used to characterize the internal gravity wave field; the highest energy peaks of each PSD were attributed to particular internal gravity waves, and the experimental frequencies were compared with the theoretical normal-mode frequencies (Antenucci & Imberger, 2001; Stocker & Imberger, 2003; Wake *et al.*, 2005). An example of this comparison is shown in the right-hand panels of figures 3.3.1–3.3.3, where the PSD of $\eta_{\mathrm{i}}(t)$ is plotted, and the natural frequencies of the highest-energy peaks are marked on the horizontal axes. A summary of this classification is shown in table 3.2, where T_w denotes the wave period; σ_t and σ_{e} denote the theoretical and experimental wave frequencies, respectively, scaled by the inertial frequency, f; and $\varepsilon_r = 100|\sigma_t - \sigma_{\mathrm{e}}|/|\sigma_t|$ denotes the relative difference between the experimental and theoretical frequencies of the corresponding wave.

Figures 3.4.1 and 3.4.2 show the decomposition of the time series of the interface displacement into the five largest modes $M(n_r, n_\theta) \in \{K(1,1), K(1,2), P(1,1), P(1,2), M(1,0)\}$, for runs 1.7 and 3.2, respectively. These two experiments had the same initial Wedderburn and Burger number, but they differed significantly in the steepening parameter; the first had $\mathcal{C}_s(W_0 = 1.0, h_* = 0.19) = 0.87$, and the second had $\mathcal{C}_s(W_0 = 1.0, h_* = 0.53) = 4.67$. The synthetic time series of the interface displacements associated with these modes was computed using a band-pass filter in a bandwidth frequency that was dependent on the internal wave frequencies, $\omega_{M(n_r,n_\theta)}$, and the recording time, T_r (see Bendat & Piersol, 2000, chap. 8). Figures 3.4.1 and 3.4.2 exhibit several aspects of the free evolution of internal waves that were previously defined based on theoretical and numerical studies (Stocker & Imberger, 2003; de la Fuente *et al.*, 2008; Sakai & Redekopp, 2010). First of all, significant vertical excursions of the density interface are observed between 100 and 150 s in figure 3.4.1, and it is attributed to $K(1,1)$ and $P(1,1)$ nonlinear interaction. This lapse of time coincides to the time in which the maximum of both Kelvin and Poincaré are in phase. However, the linear superposition of maximum displacements of $K(1,1)$ and $P(1,1)$ does not totally explain the observed vertical displacements, so it is argued that this observation is due to non-hydrostatic accelerations occurring when $K(1,1)$ and $P(1,1)$ are in phase. Second, in both cases shown in figures 3.4.1 and 3.4.2, the fundamental Kelvin wave, $K(1,1)$ exhibits a decay of its amplitude as function of time, while the fundamental Poincaré wave, $P(1,1)$, exhibits intermittent decay and amplification of the amplitude of the wave. Finally, azimuthal modes with $n_\theta > 1$ are not excited by the initial condition, so their presence can be attributed to nonlinearities in the flow dynamics.

The aforementioned aspects of the free evolution of internal gravity waves can be understood by invoking the results of previous studies (Wake *et al.*, 2005; de la Fuente *et al.*, 2008; Sakai & Redekopp, 2010). Nonlinear coupling between fundamental Kelvin and Poincaré waves and the energy dissipation of the large-scale waves of a viscous flow are two particular aspects that affect the measurements that require further analysis.

Run n.	T_w (s)	S (-)	Mode (rad, azm)	σ_t (-)	σ_e (-)	ε_r (%)	Run n.	T_w (s)	S (-)	Mode (rad, azm)	σ_t (-)	σ_e (-)	ε_r (%)
	64.0		$K(1,1)$	0.22	0.21	3.02		48.8		$K(1,1)$	0.58	0.61	5.65
	27.7		$K(1,2)$	0.45	0.49	9.61		25.6		$K(1,2)$	1.12	1.17	4.35
	20.5		$K(1,3)$	0.67	0.67	0.06		20.5		$P(1,1)$	1.43	1.46	2.17
1.1	12.5	0.20	$P(1,1)$	1.11	1.09	1.11	1.7	18.3	0.45	$K(1,3)$	1.64	1.64	0.22
	10.9		$P(1,2)$	1.25	1.25	0.31		16.2		$P(1,2)$	1.88	1.84	2.04
	10.8		$M(1,0)$	1.26	1.26	0.21		14.5		$M(1,0)$	1.99	2.06	3.74
	9.5		$P(1,3)$	1.41	1.44	2.13		12.5		$P(1,3)$	2.34	2.39	2.29
	73.2		$K(1,1)$	0.43	0.41	4.88		41.0		$K(1,1)$	0.67	0.73	8.92
	37.9		$K(1,2)$	0.84	0.79	6.00		23.3		$K(1,2)$	1.29	1.29	0.34
	26.2		$K(1,3)$	1.24	1.14	7.92		19.7		$P(1,1)$	1.52	1.52	0.04
2.1	23.8	0.35	$P(1,1)$	1.29	1.26	2.54	2.5	15.5	0.51	$K(1,3)$	1.88	1.93	2.57
	19.7		$P(1,2)$	1.61	1.52	5.59		14.2		$P(1,2)$	2.05	2.10	2.62
	18.3		$M(1,0)$	1.67	1.64	2.02		13.3		$M(1,0)$	2.20	2.25	2.23
	16.2		$P(1,3)$	1.95	1.84	5.56		12.0		$P(1,3)$	2.58	2.48	3.75
	56.9		$K(1,1)$	0.22	0.24	6.83		48.8		$K(1,1)$	0.58	0.61	5.65
	28.4		$K(1,2)$	0.45	0.47	4.45		25.0		$K(1,2)$	1.12	1.20	6.91
	19.0		$K(1,3)$	0.67	0.70	5.21		20.5		$P(1,1)$	1.43	1.46	2.17
3.1	12.5	0.20	$P(1,1)$	1.11	1.07	3.55	3.2	17.9	0.45	$K(1,3)$	1.64	1.68	2.17
	10.9		$P(1,2)$	1.25	1.23	1.82		15.3		$P(1,2)$	1.88	1.96	4.02
	9.5		$P(1,3)$	1.41	1.41	0.03		14.6		$M(1,0)$	1.99	2.05	2.78
	10.8		$M(1,0)$	1.26	1.25	0.26		12.5		$P(1,3)$	2.34	2.40	2.39

Table 3.2: Classification of the linear internal gravity wave field using a frequency criterion.

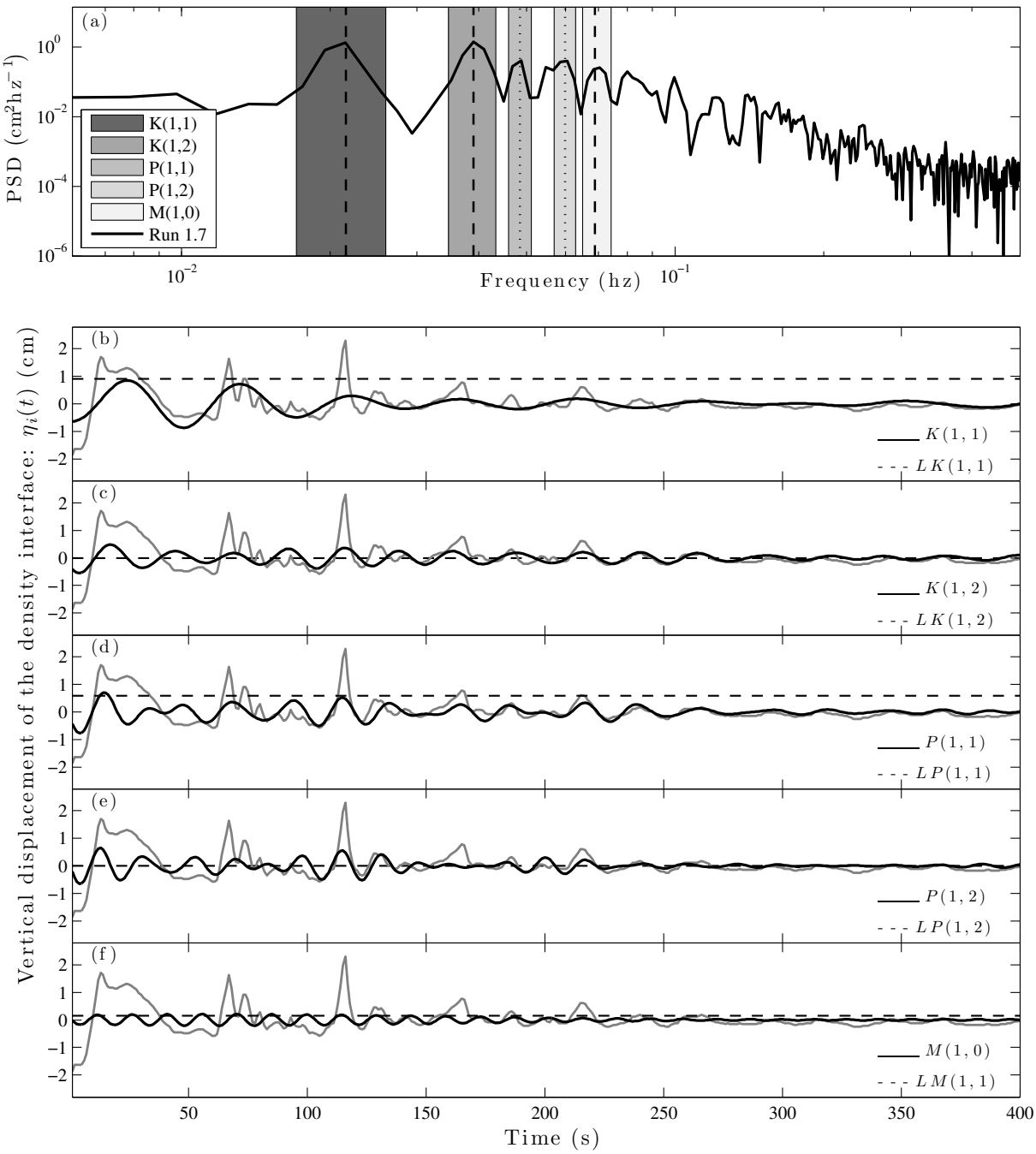

Figure 3.4.1: Panel (a) exhibits the PSD of run 1.7, with the frequency bands allocated to $K(1,1)$, $K(1,2)$, $P(1,1)$, $P(1,2)$ and $M(1,0)$. $(b-f)$ Time series of the dominant waves identified in the PSD, which were synthetically reconstructed by using a band-pass filter and the inverse Fourier transform. The horizontal dashed line in panels $(b-f)$ denotes the maximum theoretical amplitude achieved by the normal modes ($LK(1,1)$, $LP(1,1)$ and $LM(1,0)$) via the initial tilt of the density interface condition. In addition, the grey curve denotes the original time series of η_i.

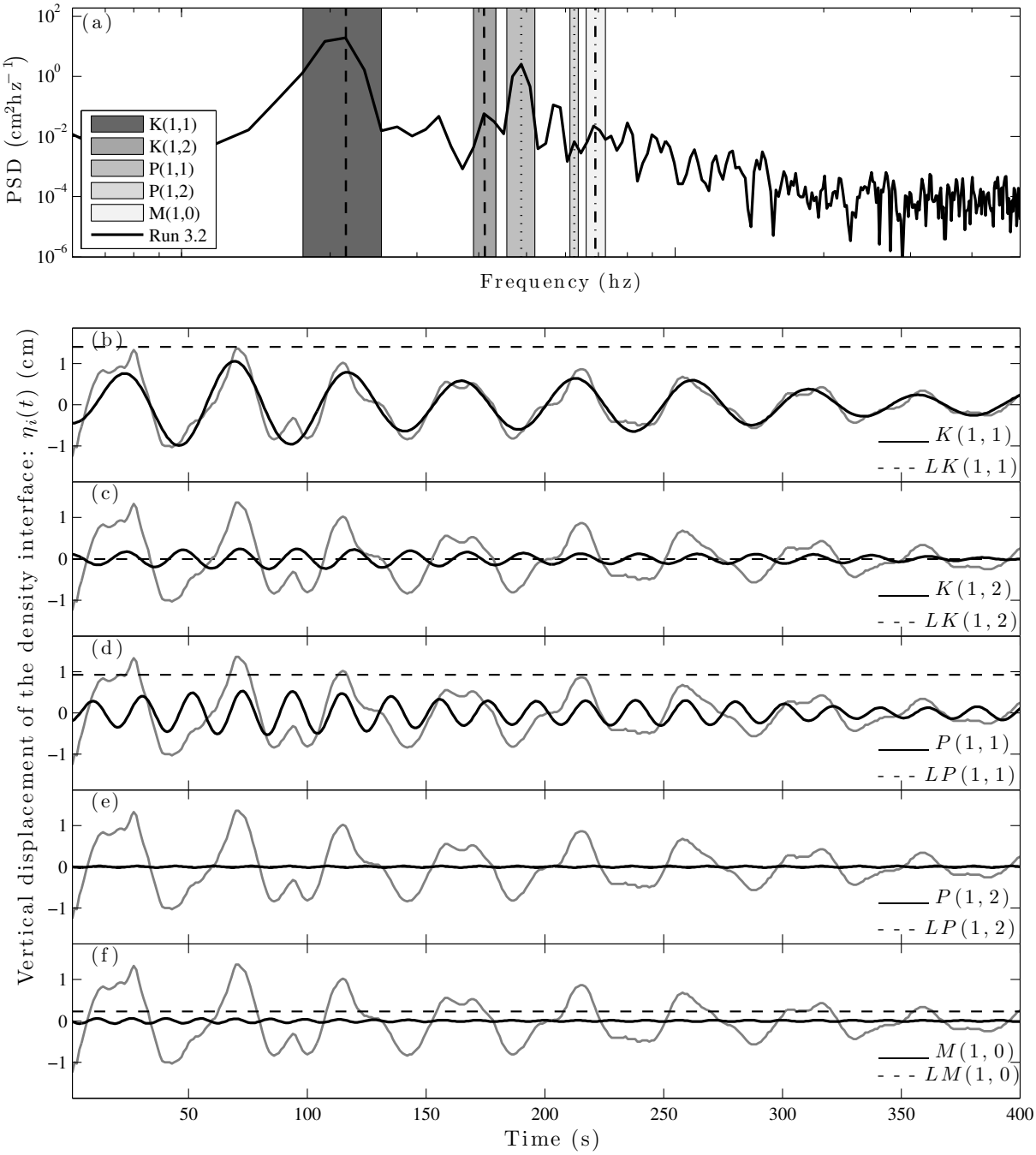

Figure 3.4.2: (a) The PSD of run 3.2, with the frequency bands allocated to $K(1,1)$, $K(1,2)$, $P(1,1)$, $P(1,2)$ and $M(1,0)$. Panels (c) to (i) idem to figure 3.4.1. $(b-f)$ idem to figure 3.4.1

3.4.2 Kelvin–Poincaré interaction

The nonlinear interaction among Kelvin and Poincaré waves generates waves whose frequencies are $\omega_{kp} = \omega_p + \omega_k$ and $\omega_{pk} = \omega_p - \omega_k$ (de la Fuente *et al.*, 2008), which can be identified in the PSD (see figures 3.3.1–3.3.3) as the structures indicated by the dashed lines and dot-dashed lines, respectively. It is observed that the frequencies ω_{kp} (dashed lines) and ω_{pk} (dot-dashed lines) are attributed to

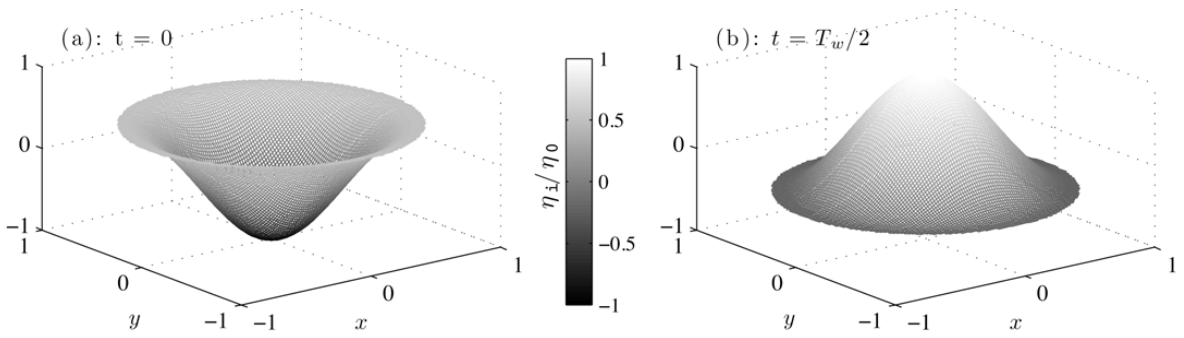

Figure 3.4.3: Spatial structure of a internal gravity wave $M(1,0)$. showing the interface displacement at (a) $t = 0$ and (b) $t = T_w/2$ (half of period).

different energy levels for each experiment. de la Fuente *et al.* (2008) observed that at the centre of the basin, a standing oscillation with a frequency ω_{kp} was excited when both the $K(1,1)$ and $P(1,1)$ waves were in phase. However, from (3.2.12) and (3.2.13), an internal gravity wave whose maximum amplitude is located at the centre of the basin, is obtained if $R_{n_\theta} = J_{n_\theta}$ and $n_\theta = 0$ and $n_r = 1$. Therefore, the wave frequency is obtained from the solution of the dispersion equation:

$$S^{-1}\sqrt{|\sigma^2 - 1|}J_{-1}\left(S^{-1}\sqrt{|\sigma^2 - 1|}\right) = 0. \tag{3.4.1}$$

We look for the root σ of (3.4.1) that corresponds to the dimensionless frequency of the first radial mode $n_r = 1$, which can be numerically calculated for a specific S. Figure 3.4.3 shows the modal structure of the density interface of the mode $M(1,0)$, which is characterized by a standing radial oscillation. $M(1,0)$ achieves its maximum amplitude at the centre of the basin and the edges of the basin. The frequency of $M(1,0)$ is indicated on the PSD by a star $(\star)$ (see figures 3.2.3–3.3.1); its frequency is quite similar to ω_{kp}. Figure 3.4.4 shows the theoretical frequency differences between $\omega_{M(1,0)}$ and ω_{kp} (black line) as a function of S; the theoretical frequencies are very similar, with a maximum difference of approximately 6%. The circles, squares and triangles in Figure 3.4.4 denote the relative error ε_r between the theoretical frequency $\omega_{M(1,0)}$ and the experimental frequency observed from the PSD. The results demonstrate that the experimental error is on the order of the theoretical difference between ω_{kp} and $\omega_{M(1,0)}$. It is possible that the nonlinear Kelvin–Poincaré interaction transfers energy to $M(1,0)$. To reinforce this idea, the spectral energy that can be attributed to the range of frequencies of $M(1,0)$ in run 1.7 was $\mathrm{e}_p = 1.40 \times 10^{-3}$ cm^2 (see figure 3.4.1a), while the energy associated with the range of frequencies of $M(1,0)$ in run 3.2 was $\mathrm{e}_p = 9.90 \times 10^{-5}$ cm^2 (see figure 3.4.2a). As a consequence, part of the energy attributed to $M(1,0)$ in run 1.7 may be related to the nonlinear interaction between $K(1,1)$ and $P(1,1)$.

The amount of energy contained in $M(1,0)$, was calculated to study its behaviour as a function of the dimensionless numbers, h_*, W_0 and S. The results are presented in dimensionless terms:

$$\mathrm{e}^*_{M(1,0)} = \frac{1}{\eta_0^2}\int_{\omega_1}^{\omega_2} \hat{\Pi}_{M(1,0)}\mathrm{d}\omega \tag{3.4.2}$$

where $\mathrm{e}^*_{M(1,0)}$ is the amount of energy contained in the characteristic frequency band $[\omega_1, \omega_2]$ of mode $M(1,0)$, and η_0 is the initial amplitude of the pycnocline. Figure 3.4.5(a) presents $\mathrm{e}^*_{M(1,0)}$ as a function of h_*, where it is observed that $\mathrm{e}^*_{M(1,0)}$ increases as h_* decreases for similar values of the Burger number $(S \approx 0.5)$. In addition, both sets of experiments $(W_0 = 0.5, W_0 = 1.0)$ show that the amount of energy

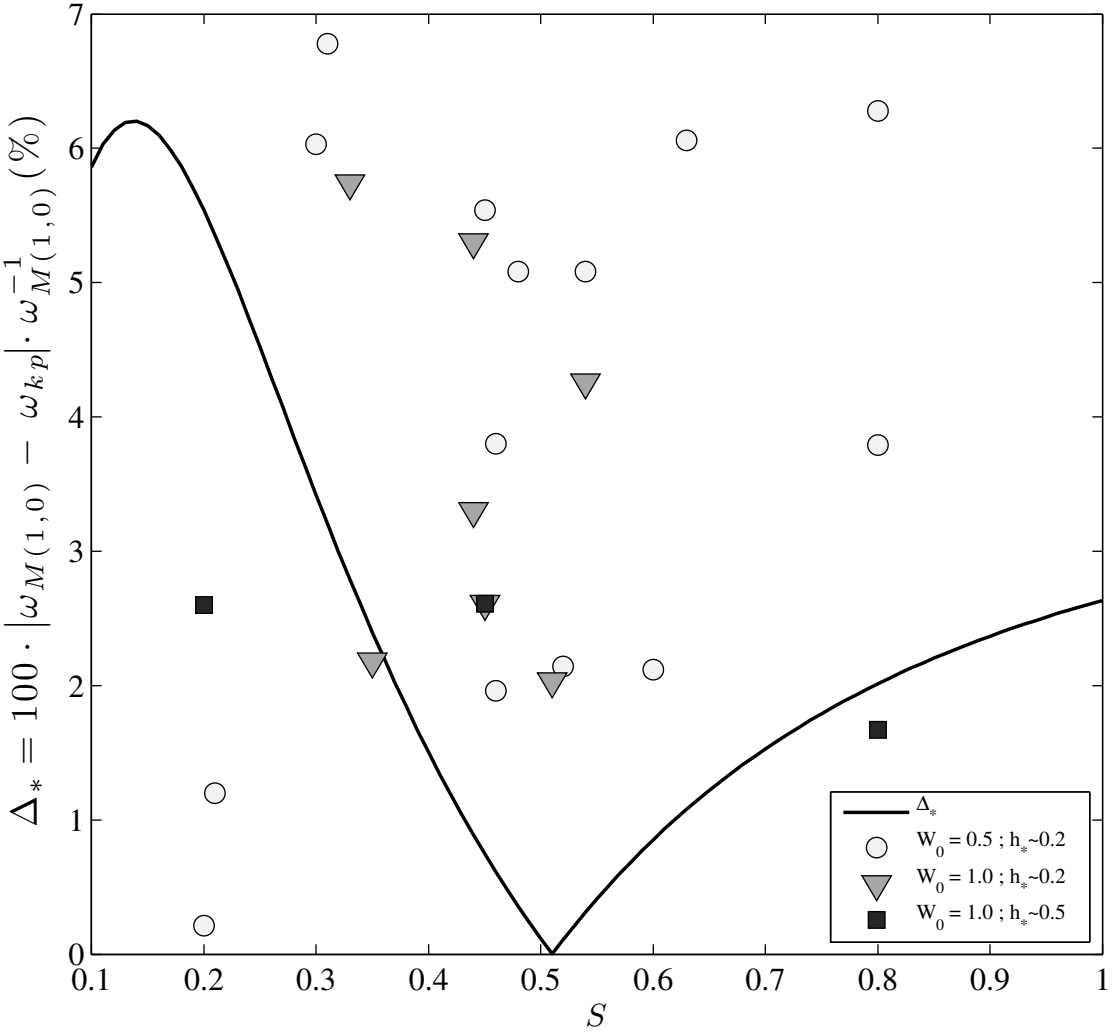

Figure 3.4.4: Plot (continuous line) of the theoretical relative difference between the fundamental geostrophic frequency, $\omega_{M(1,0)}$, and ω_{kp} frequency, as a function of Burger number, S. The white circles, the gray triangles, and the black squares denote the relative difference between the experimental and theoretical frequencies of $\omega_{M(1,0)}$, for different conditions of W_0 and h_*, as a function of S.

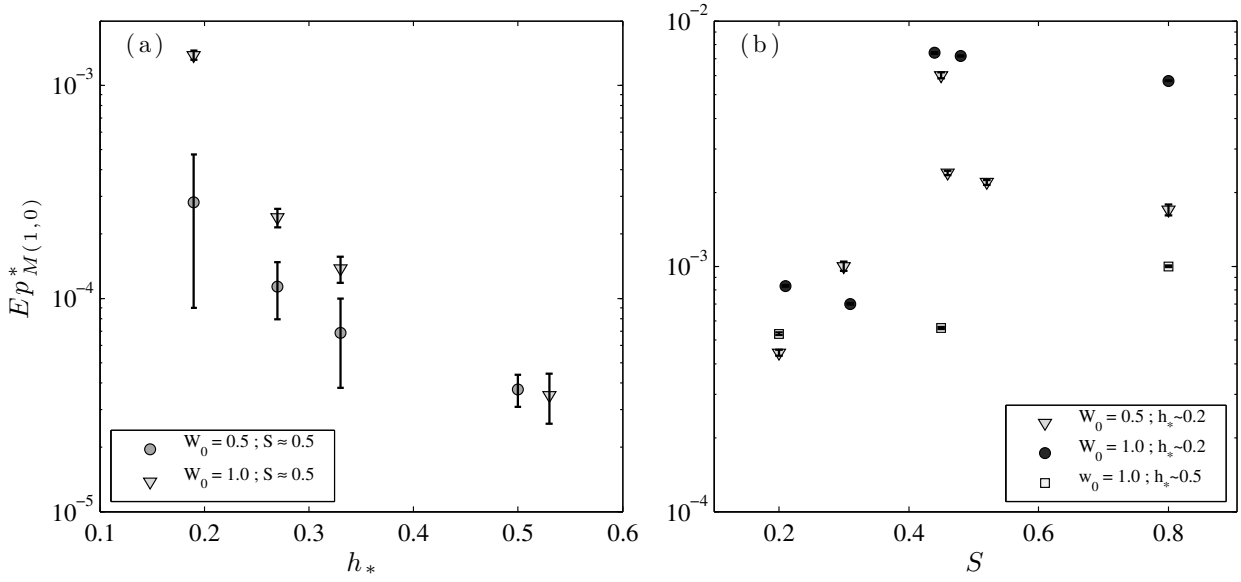

Figure 3.4.5: (a) The dimensionless potential energy of $M(1,0)$ as a function of the aspect ratio, h_*, for two initial Wedderburn numbers ($W_0 = 0.5$ and $W_0 = 1.0$), and Burger numbers approximately $S \approx 0.5 \pm 0.05$. (b) The dimensionless potential energy of mode $M(1,0)$ as a function of S, for three combinations of (W_0, h_*).

allocated in the mode $M(1,0)$ increases as the aspect ratio decreases. Furthermore, it is observed that $\mathrm{e}^*_{M(1,0)}$ exhibit a lower rate of increasing when $W_0 = 0.5$. In this condition, the steepening and the non-hydrostatic dispersion of the basin-scale wave is enhanced; therefore, the fundamental Kelvin wave evolves into a solitary-type wave. During this processes the transfer of energy from the fundamental Kelvin wave to subazimuthal Kelvin and Poincar waves can be more important than the irradiation of energy to the centre of the basin. However, no clear correlation was observed between $\mathrm{e}^*_{M(1,0)}$ and S. Results indicate that the amount of energy in $M(1,0)$ is related to the nonlinear steepening ($\mathcal{C}_s(W_0, h_*)$).

Sakai & Redekopp (2010) numerically studied the wind-forced problem, considering both a linear hydrostatic model and a nonlinear, non-hydrostatic model. The evolution of the initial internal wave field should be uncoupled unless nonlinear interactions arise among the internal gravity waves, which may produce temporal changes in the amplitude, phase speed and frequency of the waves (de la Fuente *et al.*, 2010). Figure 26 of Sakai & Redekopp (2010) compares the PSD of η_i of both models. The results demonstrate that large-scale waves irradiate energy to subazimuthal modes ($n_\theta > 1$) when a nonlinear and non-hydrostatic model is used. In this case, our results (e.g., PSD of figures 3.4.1a and 3.4.2a) show good agreement with the results of Sakai & Redekopp (2010). Nevertheless, our results indicate that even when a linear response is expected ($\mathcal{C}_s \to \infty$ as $h_* \to 0.5$), as in the case of run 3.2 (see figure 3.4.2a), it is possible to identify subazimuthal modes of Kelvin and Poincaré waves with a low energy level. In general, the evolution of $\eta_\mathrm{i}(t)$ is modulated by the most energetic modes $K(1,1)$ and $P(1,1)$; however, if $K(1,1)$ and $P(1,1)$ transfer energy to other waves via nonlinear interaction, $\eta_\mathrm{i}(t)$ will be a superposition of a rich diversity of waves.

To evaluate how much influence the linear superposition of $K(1,1)$ and $P(1,1)$ has over the evolution

of $\eta_{\rm i}(t)$, the correlation coefficient

$$R(\eta_{\rm i}, \eta_{kp}) = C(\eta_{\rm i}, \eta_{kp}) / \sqrt{C(\eta_{\rm i}, \eta_{\rm i}) C(\eta_{kp}, \eta_{kp})} \tag{3.4.3}$$

was calculated. Here C corresponds to the covariance and $\eta_{kp} = \eta_{k(1,1)} + \eta_{p(1,1)}$, where $\eta_{k(1,1)}$ and $\eta_{p(1,1)}$ correspond to the synthetic time series of $K(1,1)$ and $P(1,1)$, respectively, that were obtained by using the band-pass filter. The correlation coefficient as a function of h_* is shown in figure 3.4.6(a), with $S \approx 0.5$. The correlation coefficient as a function of S is shown in figure 3.4.6(b), with $h_* \approx 0.2$. In figure 3.4.6, the grey triangles correspond to experiments with ($W_0 = 1.0, h_* \approx 0.2$), the black circles correspond to experiments with ($W_0 = 0.5, h_* \approx 0.2$), and the white squares correspond to experiments with ($W_0 = 1.0, h_* \approx 0.5$). From figure 3.4.6, three trends in evidence: (i) as h_* increases, $R(\eta_{\rm i}, \eta_{kp})$ increases, and better correlations are achieved when $W_0 = 1.0$ (see figure 3.4.6a); (ii) no clear relationship between $R(\eta_{\rm i}, \eta_{kp})$ and S is obtained when $h_* \approx 0.2$ (see figure 3.4.6b); and (iii) the highest values of $R(\eta_{\rm i}, \eta_{kp})$ are achieved when $h_* \approx 0.5$ and $W_0 = 1.0$ (see the white squares of figure 3.4.6b). The results indicate that when the internal gravity wave field is characterized by a linear response, the linear superposition of $K(1,1)$ and $P(1,1)$ dominates the dynamics of the density interface, $0.94 \leq R(\eta_{\rm i}, \eta_{kp}) < 1$.

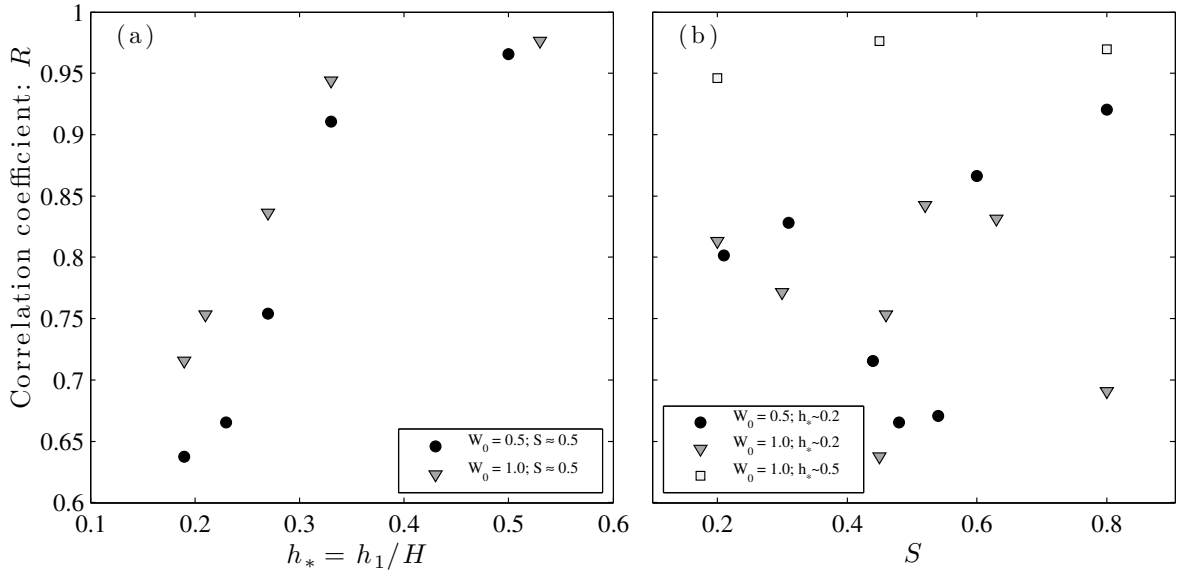

Figure 3.4.6: (a) The correlation coefficient, $R(\eta_{\rm i}, \eta_{kp})$, as a function of aspect ratio, h_*, for two values of Wedderburn numbers ($W_0 = 0.5$ and $W_0 = 1.0$), and Burger numbers approximately $S \approx 0.5 \pm 0.05$. (b) The correlation coefficient, $R(\eta_{\rm i}, \eta_{kp})$, as a of the Burger number, S.

3.4.3 Degeneration of the basin-scale internal gravity waves

The degeneration or irreversible distortion of the large-scale gravity waves is triggered by nonlinear processes. If we set W_0 to a constant value, the wave steepening is controlled by h_* (see $\mathcal{C}_s(W_0, h_*)$). Figure 3.4.7 shows the effect of the reduction of $\mathcal{C}_s(h_*)$ ($h_* \in [0.19, 0.5]$), starting from an initial Wedderburn number of $W_0 = 0.5$ and a Burger number of $S \approx 0.50 \pm 0.05$. When $\mathcal{C}_s \to \infty$ ($h_* = 0.50$), it is not possible to distinguish the formation of nonlinear waves (see figure 3.4.7a). Nevertheless, as $\mathcal{C}_s$ decreases, the degeneration of the basin-scale internal gravity waves increases; it is observed that

the leading wave evolves into a solitary-type package (see grey area on plots of figures 3.4.7*b*–e), and $\eta_i(t)$ exhibits high amplitudes and steep slopes.

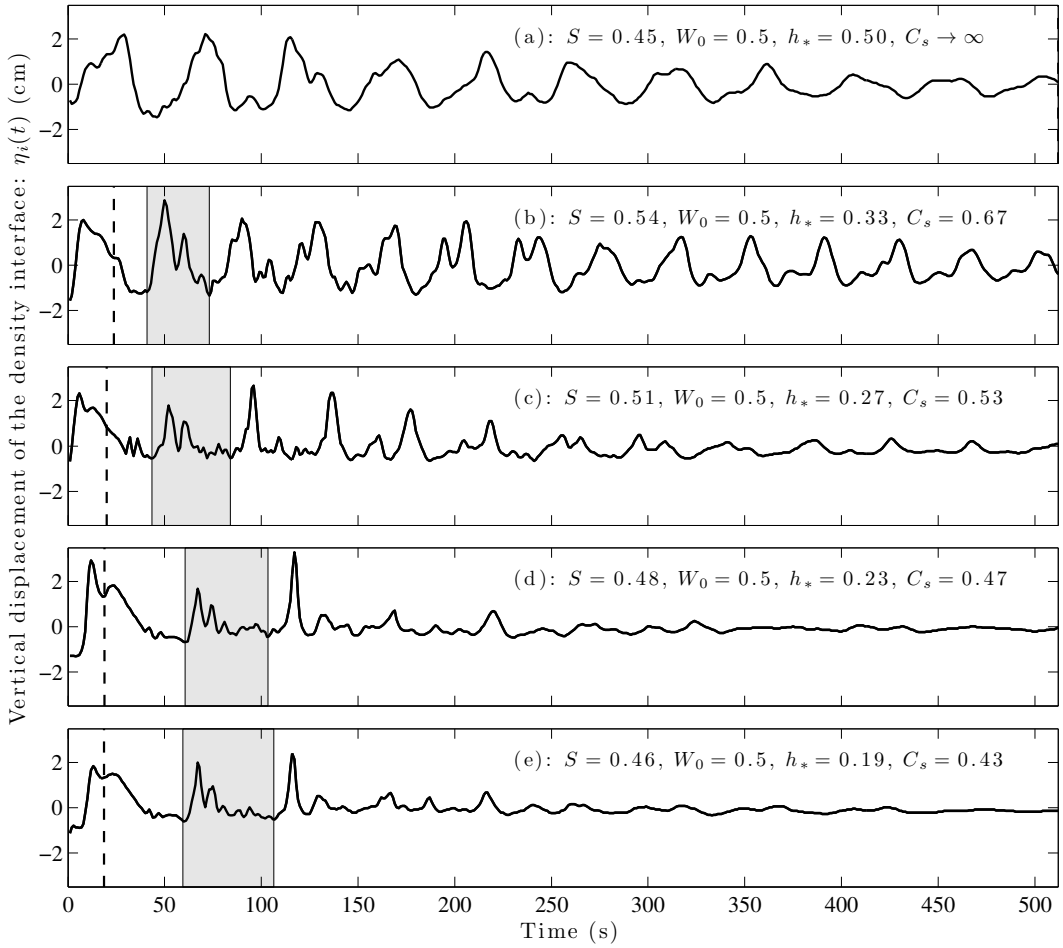

Figure 3.4.7: Time series of the density interface that show the effect of the steepening process in the basin-scale waves as a function of $\mathcal{C}_s(h_*)$ ($W = 0.5$ and $S = 0.50 \pm 0.05$). In (a) a time series with $\mathcal{C}_s(h_* = 0.5) \to \infty$, therefore a linear behaviour of the interface density is expected. In (b–e) the dashed line marks the steepening time scale, T_s, of the basin-scale waves. Moreover, in the grey region the first solitary-type wave packet is identified.

Figure 3.4.8 shows a summary of the geometrical properties of the leading solitary-type waves located in the grey regions of figure 3.4.7. Figure 3.4.8(a) presents changes in the dimensionless amplitude of the leading solitary wave at the time $t = T_s$, a_{s0}/η_0, as a function of the steepening parameter $\mathcal{C}_s$, where the dimensional wave amplitude, a_{s0}, was normalized to the time T_s by fitting the peaks of the density interface to the curve:

$$a_{s0}(t) = A_s \exp(-\gamma_s t), \tag{3.4.4}$$

to obtain the decay timescale, γ_s, and the initial amplitude A_s. As $\mathcal{C}_s$ decreases, there is a significant reduction in the ratio $a_{s0}(T_s)/\eta_0$. Figure 3.4.8(b) presents similar results for the dimensionless wavelength λ_{s0}/λ_t of the leading solitary-type wave observed in each grey region of figure 3.4.6, where λ_{s0} denotes the experimental wavelength and λ_t the theoretical wavelength of a solitary wave. The experimental wavelengths were estimated to be $\lambda_{s0} \approx c_s \Delta T_{s0}$, where c_s is the average Kelvin wave celerity calculated

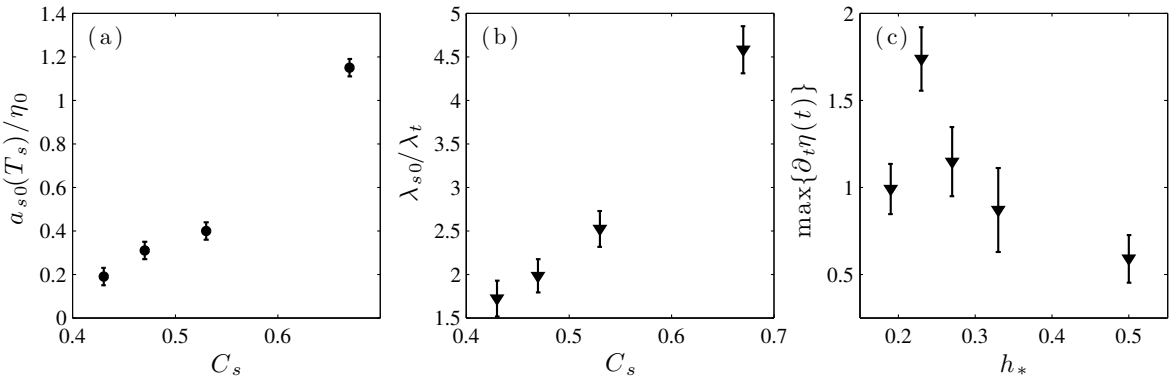

Figure 3.4.8: A summary of geometrical properties of the leading solitary-type wave observed in figure 3.4.7. (a) exhibits the dimensionless amplitude of the leading solitary wave, a_{s0}/η_0, as a function of dimensionless steepening parameter $\mathcal{C}_s$. Panel (b) exhibits the dimensionless wavelength, λ_{s0}/λ_t, as a function of $\mathcal{C}_s$. Panel (c) exhibits the maximum vertical velocity of the density interface, $\max(\partial_t\eta_{\rm i}(t))$, as a function of the aspect ratio, h_*.

as $2\pi R\omega_k$, and ΔT_{s0} is the time window of the first leading solitary wave. The theoretical wavelengths were estimated using the following expression:

$$\lambda_t^2 = \frac{12\beta}{a_{s0}\left(\alpha_1 + \frac{1}{2}\alpha_2 a_{s0}\right)}, \tag{3.4.5}$$

where α_1, α_2 and β are standard second-order KdV equation coefficients (Helfrich & Melville, 2006):

$$\alpha_1 = \frac{3}{2}c_{\rm i}\frac{h_1 - h_2}{h_1 h_2}, \quad \alpha_2 = \frac{3c_{\rm i}}{(h_1 h_2)^2}\left[\frac{7}{8}(h_1 - h_2)^2 - \left(\frac{h_2^3 + h_1^3}{h_1 + h_2}\right)\right], \quad \beta = \frac{c_{\rm i}}{6}h_1 h_2. \tag{3.4.6}$$

Finally, figure 3.4.8(c) shows the value of $\max(\partial_t\eta_{\rm i}(t))$ as a function of h_*, which demonstrates that the maximum vertical velocity of the density interface tends to decrease as h_* increases.

The characteristics of the solitary-type waves observed in the experiments follow the unidirectional steepening of the fundamental Kelvin wave along the perimeter of the tank. This suggests that the geometry of these observed solitary-type waves follows the theoretical results obtained for unidirectional waves. In particular, the second-order KdV scale was used to investigate the influence of rotation on the solitary-type wavelength (Helfrich & Melville, 2006). This wavelength, λ_s, can be written in a dimensionless form as (Helfrich & Melville, 2006)

$$\left(\frac{\lambda_s}{h_1}\right)^2 = \frac{K_s(1 - h_*)^2}{\eta_{s0}^*\left(1 - 2h_*\right) + \frac{\left(\eta_{s0}^*\right)^2}{2}\left(\frac{1-h_*}{h_*}\right)}, \tag{3.4.7}$$

where K_s is a coefficient with a value equal to 12 in the case of a unidirectional wave that is not affected by rotation (Helfrich & Melville, 2006), and $\eta_{s0}^* = a_{s0}/H$, where a_{s0} is the amplitude of the wave. It is considered that K_s is a bulk parameter that accounts for all influences of the rotation on the solitary-type wavelength. Figure 3.4.9 shows the experimental dependence of K_s in terms of S^{-1}, where it is observed that the wavelength of the solitary-type waves decreases as the rotation increases. No influence of the Wedderburn number was observed on the value of K_s, which indicates that length

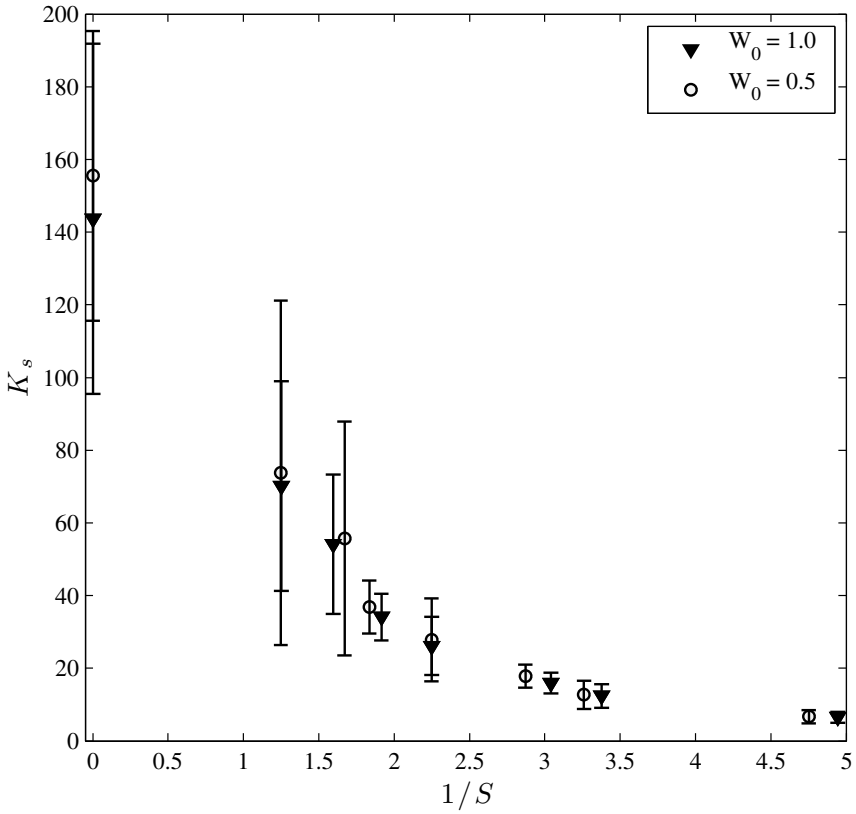

Figure 3.4.9: Panel of K_s as a function of the Burger number, S, for two initial Wedderburn numbers ($W_0 = 0.5$ and $W_0 = 1.0$).

Set	h_*	W_0	a_i	b_i	R^2
•	0.2	0.5	0.24	-0.53	0.90
△	0.2	1.0	0.19	-0.49	0.68
□	0.5	1.0	0.11	-0.48	0.99

Table 3.3: Fitting parameters of the experimental decay rate in terms of Burger number.

scales in the second-order KdV equations are suitable to characterize this flow. In the limit of $S \to 0$, the value of K_s seems to be asymptotic to a value close to $K_s = 12$, which is in good agreement with the prediction of the second-order KdV equation, whereas K_s takes on values that are one order of magnitude larger than $K_s = 12$, as the influence of the rotation decreases.

3.4.4 Bulk decay of the fundamental Kelvin wave: $K(1,1)$

The results indicate that $\eta_\mathrm{i}(t)$ is characterized by a composition of oscillatory motions that are affected by a continuous decay of the vertical displacement. The most energetic mode in the initial wave field is $K(1,1)$, which is damped in time by viscous dissipation and the nonlinear energy transfer from $K(1,1)$ to other modes (de la Fuente *et al.*, 2008; Shimizu & Imberger, 2009; Sakai & Redekopp, 2010).

The influence of friction on the wave dynamics can be included using a linearized equation for the

rotating Rayleigh bottom shear stress, which is proportional to the flow velocity (Martinsen & Weber, 1981; Wake *et al.*, 2005). Following this approach, Stocker *et al.* (2000) determined that the waves of the density interface decay exponentially over time in a circular basin, with the following form: $\eta \sim \eta_0 \exp(-kt)$. Based on this finding, a bulk decay time scale of the fundamental Kelvin wave, $K(1,1)$, can be obtained by fitting the filtered amplitudes of $K(1,1)$ and η_k with an harmonic damped function as follows:

$$\frac{\eta_k(t^*)}{\eta_0} = \cos(\omega_k t^* + \phi) \exp\left(-\frac{t^*}{T_k}\frac{1}{\tau_{\mathrm{dk}}}\right), \tag{3.4.8}$$

where η_0 is the initial amplitude of the pycnocline, ω_k is the natural frequency of $K(1,1)$, ϕ is the wave phase to be fitted, t^* is the dimensional time. T_k is the Kelvin wave period and τ_{dk}^{-1} is the dimensionless bulk decay coefficient that was obtained for each experiment. Figure 3.4.10a shows the dependence of τ_{dk}^{-1} on the Burger number. The results were grouped into three classes: the curves described by circles and triangles correspond to experiments with $h_* \sim 0.2$ and either $W_0 = 0.5$ or $W_0 = 1.0$, respectively, and the curve described by squares corresponds to experiments with $h_* = 0.5$ and $W = 1.0$. All three sets of experiments show that the decay rate increases as the rotation becomes more important to the dynamics of the flow. Potential functions were fitted to each set, $a_{\mathrm{i}} S^{b_{\mathrm{i}}}$, with coefficients a_{i} and b_{i}, to estimate the experimental relation between S and the decay rate of $K(1,1)$. The coefficients of figure 3.4.10(a) are presented in Table 3.3. It is observed that $\tau_{\mathrm{dk}}^{-1} \propto 1/\sqrt{S}$ or $\tau_{\mathrm{dk}}^{-1} \propto \sqrt{f}$, which may indicate that the decay mechanism can be attributed to the friction developed in a non-stationary Ekman-type layer (Pedlosky, 1987; Wake *et al.*, 2005). Figure 3.4.11(a) shows the experimental Ekman damping time scale (τ_{Ek}^{e}) as a function of the theoretical Ekman damping time scale (τ_{Ek}^{t}), which is defined as

$$\tau_{Ek}^{t} = \frac{T_{Ek}}{T_f} = \frac{h_1}{\pi}\sqrt{\frac{f}{2\nu}}, \tag{3.4.9}$$

where $T_f = 2\pi/f$ is the inertial period and ν corresponds to the kinetic viscosity of the fluid. The

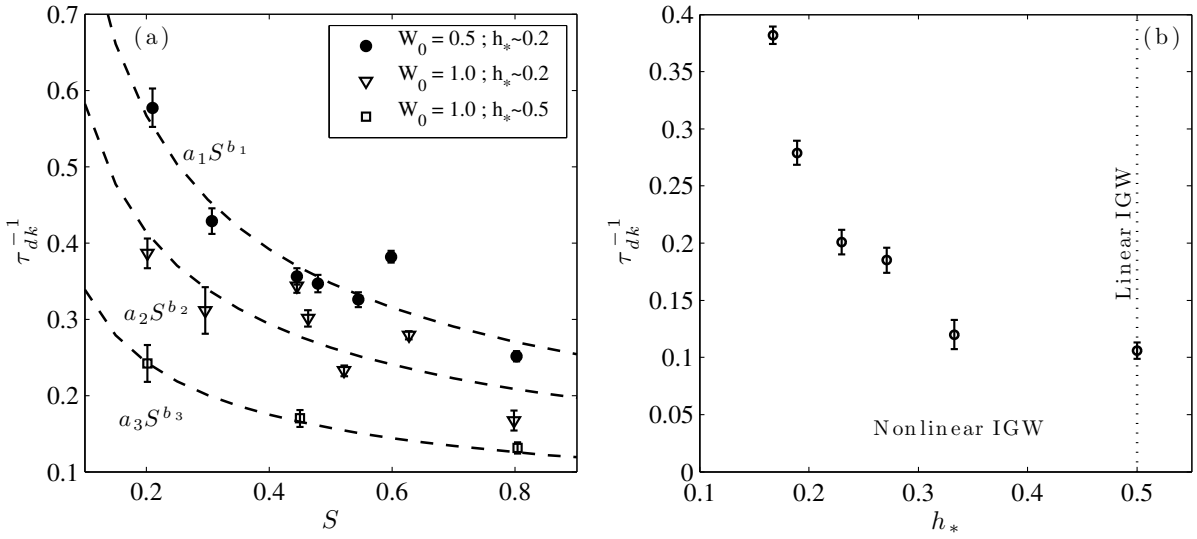

Figure 3.4.10: (a) The relation between the rate of decay of the fundamental Kelvin wave, τ_{dk}^{-1}, with the initial Wedderburn number, W_0, the Burger number, S, and the aspect ratio, h_*. (b) The rate of decay of the fundamental Kelvin wave. τ_{dk}^{-1}, as a function of the aspect ratio, h_*, with $W_0 = 0.5$ and $S \approx 0.50 \pm 0.05$.

results show that $\tau^{\mathrm{e}}_{Ek} \approx \tau^{t}_{Ek}$ when $W_0 = 1.0$ and $h_* \approx 0.5$. However, it was not possible to identify any significant correlation between τ^{t}_{Ek} and τ^{e}_{Ek} when $h_* \sim 0.2$ (triangles and circles in figure 3.4.11a); this result suggests that the decay of $K(1,1)$ is influenced by the nonlinear processes. Indeed, figure 3.4.10(b) shows the relation between the aspect ratio h_* and the decay rate of $K(1,1)$. These results indicate that the bulk decay of $K(1,1)$ is strongly dependent on the nonlinear steepening. When $h_* = 0.5$, the decay coefficient, $\tau^{-1}_{\mathrm{d}k}$, takes on its minimum value, which is 5.5 times less than the maximum value measured at $h_* = 0.19$. Hence, a faster decay is expected when nonlinearities are involved in the evolution of $K(1,1)$. Moreover, Grimshaw *et al.* (1998) and Grimshaw & Helfrich (2012) have demonstrated that an initial solitary-type wave evolves into an oscillatory wave packet when background rotation affects the flow. Figure 3.3.2 suggests that the rotation plays an important role in the disintegration of the basin-scale wave. In this sense, Grimshaw *et al.* (1998) and Grimshaw & Helfrich (2012) have found an extinction time scale, $T_{\mathrm{e}x}$, associated with the solitary wave, which depends on the initial amplitude, the KdV coefficients and the rotation; this scale can be written in terms of the Kelvin wave period as follows:

$$\tau_{\mathrm{e}x} = \frac{T_{\mathrm{e}x}}{T_k} = \frac{c_{\mathrm{i}}}{\lambda_s f^2} T_k^{-1}, \tag{3.4.10}$$

where λ_s is the wavelength of the solitary wave (see 3.4.5), which depends of the KdV coefficients (Helfrich & Melville, 2006). The extinction time scale was estimated via the experimental wavelength of the first leading solitary-type wave λ_{s0}, calculated in the previous subsection. Figure 3.4.11(b) shows the bulk decay time scale $\tau_{\mathrm{d}k}$ as a function of the extinction time scale $\tau_{\mathrm{e}x}$. Results show that the bulk decay time scales decreases as the extinction time scale decreases, indicating a direct relationship between the bulk decay rate of $K(1,1)$ and the extinction rate of the solitary waves into radiating waves.

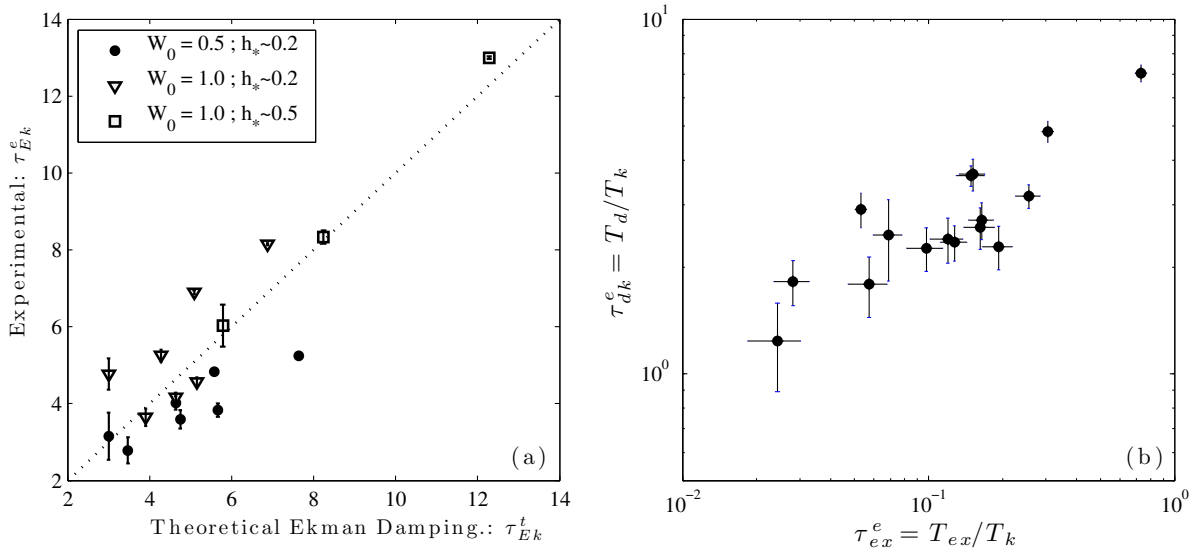

Figure 3.4.11: (a) The experimental Ekman damping time scale as a function of the theoretical Ekman damping time scale. (b) The bulk decay rate of the fundamental Kelvin wave, $\tau_{\mathrm{d}k}$, as a function of the extinction time scale, $\tau_{\mathrm{e}x}$, made dimensionless with T_k.

3.5 Discussion and conclusions

The free evolution of basin-scale gravity waves affected by background rotation and nonlinear processes was studied via laboratory experiments.

First, the frequencies of the lowest Kelvin and Poincaré waves ($n_\theta \leq 3$) were well predicted ($\varepsilon_r < 10\%$, see table 3.2) by the theoretical frequencies that were derived from the linear governing equations (Csanady, 1967; Stocker & Imberger, 2003). The evolution of the internal wave field associated with $\mathcal{C}_s(h_* \sim 0.5) \to \infty$ exhibits good similarity with previous laboratory studies (Wake *et al.*, 2004, 2005); under these conditions, no steepening or solitary-type waves were observed. However, the experimental results confirm the steepening and the subsequent degeneration of the Kelvin wave into a solitary-type wave package when $\mathcal{C}_s < 1$; this behaviour has been previously identified by de la Fuente *et al.* (2008) and Sakai & Redekopp (2010) using weakly nonlinear and non-hydrostatic numerical models. Nevertheless, the number of solitary-type waves generated from the degeneration of a Kelvin wave was larger in our experiments than in the numerical results of de la Fuente *et al.* (2008) and Sakai & Redekopp (2010); this difference may be attributable to the weakly nonlinear numerical schemes used by the authors. In general, the internal wave-field response appears to be strongly influenced by the aspect ratio of the stratification (h_*) and the background rotation (S), in agreement with the early experiments of Renouard *et al.* (1993). Results presented in figure 3.3.1 propound that the increment of background rotation may influence the energy transfer and distribution when weakly nonlinear processes are involved on evolution of basin-scale internal waves; nonetheless further studies are required.

Second, the results suggest that the nonlinear Kelvin–Poincaré interaction could be transferring energy to the mode $M(1,0)$ (see figure 3.4.3), because its modal frequency is $\omega_{M(1,0)} \sim (\omega_{kp})$; in addition, de la Fuente *et al.* (2008) observed that, in this context, a standing internal gravity wave was excited at the centre of basin with a frequency ω_{kp}. The results demonstrate that the energy of $M(1,0)$ increases as the nonlinear effects increase. Furthermore, the results obtained from the decomposition of the main modes indicate that the linear superposition of $K(1,1)$ and $P(1,1)$ almost completely restores the dynamics of the density interface, when the aspect ratio is $h_* \approx 0.5$. However, as h_* decreases, the linear superposition of $K(1,1)$ and $P(1,1)$ loses its correlation with respect the full signal of η_i (see figure 3.4.6*a*); this result is related to the energy transfer from $K(1,1)$ and $P(1,1)$ to other subazimuthal modes of higher frequencies. Furthermore, energy peaks of ω_{kp} and ω_{pk} indicate that, depending on the value of the Burger number, the nonlinear interaction between the $K(1,1)$ and $P(1,1)$ modes may transfer energy to lower frequencies than ω_k, when $S \geq 0.5$ (see figures 3.3.2*f*, 3.3.3d and 3.3.3*f*), thus generating an energy cascade in two directions simultaneously, as has also been observed by Wake *et al.* (2005). Energy peaks associated with lower-frequency waves than ω_{pk} were also observed when $S \geq 0.51$, although it was not possible to identify with which pair of interacting modes these could be associated.

Third, it was shown that the azimuthal length scale of the first solitary wave is affected by both the aspect ratio of stratification and the rotation. The relation between the wavelength λ_t and S is well described by the length scales predicted by the second-order unidirectional KdV equation (Helfrich & Melville, 2006) when S approaches zero, which suggests that driven azimuthal flow can be represented by unidirectional waves propagating along the perimeter of the basin, as the Kelvin wave is more strongly trapped on the edge when S approaches zero (Stocker & Imberger, 2003). In this context, Grimshaw (1985) and Katsis & Akylas (1987) showed via theoretical and numerical analysis, respectively, that nonlinearities and background rotation play an important role in the evolution of

Kelvin and solitary waves. The theoretical and numerical results show that for strong rotation, a Kelvin wave can evolve as a KdV-type wave at the boundary and as a linear Kelvin wave in the offshore region. Moreover, the front of the wave is curved backward and this process can transfer energy from Kelvin to Poincaré waves as well as a resonant state between above waves, as shown by Melville *et al.* (1989). Our work does not explore the evolution of the density interface in the offshore region, however the evidence of a nonlinear interaction between the fundamental modes of the Kelvin and Poincaré waves may help to support the above theoretical results.

Fourth, the experimental decay-rate measurements exhibit a good correlation with the time scale associated with viscous dissipation mechanisms induced by the rotation of the system for a quasi-linear response of the density interface ($h_* \approx 0.5$), and its differences may be related with the fact that the experimental tank has an upper lid, which generates an additional energy sink. However, when the nonlinear processes are act of the basin-scale waves, the decay of $K(1,1)$ can be controlled by the transfer of energy to other modes in the off-shore region, as is the case of mode $M(1,0)$, but also to modes and waves in the azimuthal shore region via the degeneration of $K(1,1)$ into a solitary-type wave package. The correlation between the extinction time scale, τ_{ex}, and the decay time scale of τ_{dk}, suggest that the decay of the fundamental Kelvin wave could be controlled by the disintegration of the solitary-type waves.

Recent field studies have identified the passage of basin-scale internal Kelvin waves associated with strong steepening as well as to solitary-type waves in large lakes (Boegman *et al.*, 2003; Appt *et al.*, 2004; de la Fuente *et al.*, 2010; Preusse *et al.*, 2010, 2012b). However, the role played by the background rotation in the degeneration and dissipation of basin-scale internal gravity waves, in enclosed basins, has not been well characterized; therefore, further investigations are required. The results presented in the study identify different mechanisms that enhanced the damping of the basin-scale internal waves in large stratified lakes. For example, seasonal changes on stratification (h_* and S) of Lake Kinneret, Israel, are correlated with significant differences in the damping evolution of large-scale internal waves affected by rotation (Shimizu & Imberger, 2010). Furthermore, seasonal changes of the stratification (h_* and S) may change the response of solitary-type waves in large lakes (Preusse *et al.*, 2012b). The steeping and degeneration of basin-scale waves has been associated with instabilities and breaking of internal waves, which can generate turbulent and mixing patches (Boegman & Ivey, 2009; Preusse *et al.*, 2010, 2012b; Bouffard *et al.*, 2012). In the most energetic experiments ($W_0 = 0.5$), small interfacial instabilities and the ejection of vortices from the basin-scale wave to the upper layer were observed during the steepening process ($h_* < 0.5$), but only in the first period. These processes enhance the vertical mixing; therefore, the modal structure of the internal gravity waves can evolve in time, which is indicated by the discrepancy between the theoretical and the experimental wave frequencies.

Acknowledgements

The authors acknowledge support of the Civil Engineering Department, Universidad de Chile and the FONDECYT Project 1080617. We thank Carlos Rozas, Carlos M. García and Kraig B. Winters for helpful comments and discussions. The authors would like to thank three anonymous referees whose constructive criticisms and comments have led to improvements in the paper. The first author acknowledges financial support from the CONICYT doctoral fellowship *No.* 21110069.

Chapter 4

Degeneration of internal Kelvin waves in a stratified rotating basin. Numerical experiments

This chapter has been published as research paper, authored by Hugo Ulloa, Kraig Winters, Alberto de la Fuente and Yarko Niño, in Journal of Fluid Mechanics (2015), http://dx.doi.org/10.1017/jfm.2015.311.

Abstract

We explore the evolution of the gravest internal Kelvin wave in a two-layer rotating cylindrical basin, using direct numerical simulations with a hyper-viscosity/diffusion approach to illustrate different dynamic and energetic regimes. The initial condition is derived from Csanady's (*J. Geophys. Res.* Vol. 72, 1967, pp. 4151-4162) conceptual model, which is adapted by allowing molecular diffusion to smooth the discontinuous idealized solution over a transition scale, $\delta_{\rm i}$, taken to be small compared to both layer thicknesses h_ℓ, $\ell = 1, 2$. The different regimes are obtained by varying the initial wave amplitude, η_0, for the same stratification and rotation. Increasing η_0 increases both the tendency for wave steepening and the shear in the vicinity of the density interface. We present results across several regimes: from the damped, linear-laminar regime (DLR), for which $\eta_0 \sim \delta_{\rm i}$ and the Kelvin wave retains its linear character, to the nonlinear-turbulent transition regime (TR), for which the amplitude η_0 approaches the thickness of the (thinner) upper layer h_1, and nonlinearity and dispersion become significant, leading to hydrodynamic instabilities at the interface. In the TR, localized turbulent patches are produced by Kelvin wave breaking, i.e. shear and convective instabilities that occur at the front and tail of energetic waves within an internal Rossby radius of deformation from the boundary. The mixing and dissipation associated with the patches are characterized in terms of dimensionless turbulence intensity parameters that quantify the locally elevated dissipation rates of kinetic energy and buoyancy variance.

4.1 Introduction

Physical processes that control the degeneration of basin-scale internal gravity waves (IGW) in stratified lakes affected by earth's rotation have been subject of considerable interest for several decades, owing to their impact on transport and water quality (Wüest & Lorke, 2003; Boehrer & Schultze, 2008). In these aquatic systems, the fundamental IGWs are the known Poincaré and Kelvin waves (Lamb, 1932; Csanady, 1967), where the latter IGW is usually the most energetic mode (Antenucci & Imberger, 2001; Stocker & Imberger, 2003). Field measurements have shown that the passage of internal Kelvin waves is correlated with high-frequency internal waves (Boegman *et al.*, 2003; Lorke *et al.*, 2006; de la Fuente *et al.*, 2010), shear instabilities and local overturns near the wave troughs in the near-shore regions (Preusse *et al.*, 2010, 2012b). These processes lead to significant localized turbulence and mixing in the pelagic thermocline (Lorke, 2007; Bouffard & Lemmin, 2013). Over the course of the stratified season, dynamical changes in the wave regime can alter the spatial and temporal distribution of turbulent activity induced by Kelvin waves.

Previous numerical and laboratory studies have analysed the internal Kelvin wave evolution in laminar and weakly nonlinear regimes, obtaining that the wave amplitude, stratification and rotation play an important role in the degeneration and damping processes (de la Fuente *et al.*, 2008; Shimizu & Imberger, 2009; Sakai & Redekopp, 2010; Rozas *et al.*, 2014; Ulloa *et al.*, 2014). Here we extend the study of the internal Kelvin waves to nonlinear regimes at which turbulence starts to emerge, using continuous and smooth solutions that allow control the wavefront steepening and the interfacial shear flow through the initial wave amplitude.

In this study we analyse the degeneration of the 'gravest internal Kelvin wave' (hereinafter IKW) in a two-layer stratified basin under different dynamic regimes; from a laminar, linear flow to a nonlinear regime characterized by the transition to turbulence. To this end, we have performed three-dimensional direct numerical simulations (DNS) of the governing equations in a cylindrical domain. The governing equations are the standard three-dimensional Boussinesq equations with m-order hyper-viscosity/diffusion operators (Winters & D'Asaro, 1997; Waite & Bartello, 2004). The use of a hyper-viscosity/diffusion approach enabled us to increase the scale separation between the forcing and dissipation length scales, producing a larger inertial subrange in the model while confining the dissipation length scales as close as possible to the grid spacing (Spyksma *et al.*, 2012). The use of a cylindrical domain permits the derivation of the linear modal structure of IKWs for a discontinuous two-layer stratification (Csanady, 1967). This solution was then allowed to diffuse vertically via Laplacian diffusion and molecular diffusivities for mass and momentum for a finite time interval producing slightly smoothed versions of linear normal modes in a continuous, nearly two-layer stratification. The length scale δ_{i} defines the thickness of the sharp pycnocline, which is constrained to be smaller than the thinner upper layer thickness h_1. The advantage of this approach is twofold. First, continuous representations of the model solutions are required for the initialization of the numerical model. Second, in calculating the modal solutions, the amplitude of the interface displacement can be taken as a significant fraction of the upper layer thickness without introducing density overturns, whereas if the equations are first linearized about a smooth but sharp density interface, modal amplitudes are restricted to values significantly smaller than the interface scale δ_{i}.

Figure 4.1.1 shows a schematic of the conceptual model, where the subscripts 1 and 2 indicate the upper and lower layer, respectively. The horizontal and vertical length scales are the diameter D, equal to twice the radius R, and the sum of the two layer thicknesses $H = h_1 + h_2$, respectively; ρ_ℓ denotes the density of the ℓ^{th} layer. Rotation is characterized by the inertial frequency f, which, together with the linear internal celerity, $c_{\mathrm{i}} = \sqrt{g' h_1 h_2 / H}$, define the internal Rossby radius of deformation, $R_{\mathrm{i}} = c_{\mathrm{i}}/f$, from the boundary to the interior, where $g' = g\Delta\rho/\rho_1$ is the reduced gravity and $\Delta\rho = \rho_2 - \rho_1$. The vertical displacement of the density interface is defined as η_{i}, whose maximum initial amplitude is hereinafter denoted by $\eta_0 = \max\{\eta_{\mathrm{i}}(t=0,\vec{x})\}$. Note that because of the spatial structure of IKWs, η_0 occurs at the shoreline (Csanady, 1967), i.e. near the vertical sidewalls in our experiments. Our experiments consist of initializing the flow with instantaneous snapshots of smoothed IKW modal solutions at various initial amplitudes η_0 and allowing these initial conditions to evolve under the nonlinear, non-hydrostatic equation of motion. The outline of the paper is as follows. In S4.2 we introduce the equations of motion, dimensionless parameters and the set of numerical experiments. In S4.3 the IKW response is described in terms of dynamic regimes, while in S4.4 we analyse the spatiotemporal distribution of the turbulent activity, focusing on those IKWs in the laminar-turbulent transition regime. Finally, we summarize and discuss our results in S4.5.

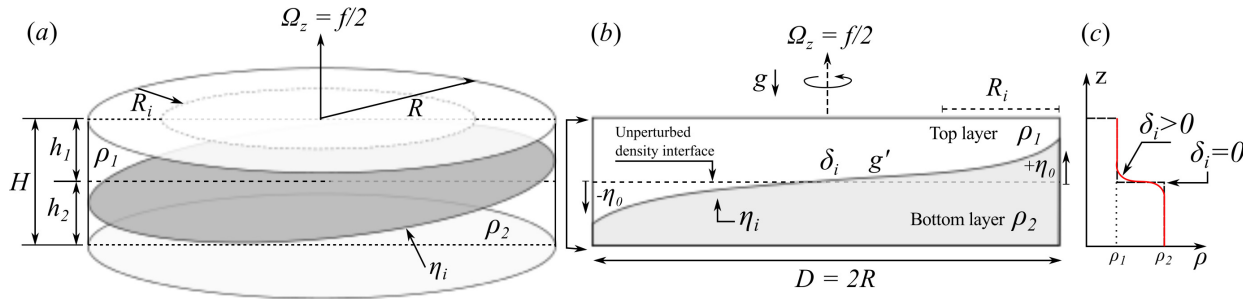

Figure 4.1.1: Schematic of conceptual model. (a) Three-dimensional view of the domain, a two-layer rotating cylindrical basin of radius R and total depth H. (b) Two-dimensional plane across a diameter of the basin. (c) Vertical density profile at the centre of the basin (continuous line denotes a smooth two-layer stratification).

4.2 Formulation

4.2.1 Governing equations and boundary conditions

We study the IKW flow via the numerical solution of the Boussinesq equations of motion for a rotating stratified fluid on an f-plane with a m-order viscosity/diffusion operator, written as

$$\frac{D\vec{v}}{Dt} + (f\hat{k}) \times \vec{v} + \frac{\rho}{\rho_0} g\hat{k} = -\frac{1}{\rho_0}\nabla p + \mathcal{D}_m(\vec{v}) \quad ; \quad \frac{D\rho}{Dt} = \mathcal{D}_m(\rho) \quad ; \quad \nabla \cdot \vec{v} = 0 \tag{4.2.1}$$

where D/Dt is the material derivative, $\vec{v} = (u, v, w)$ is the velocity vector, ρ_0 and ρ are the ambient reference density and the Boussinesq density difference from ρ_0. Further, p is the pressure field, $\hat{k}$ is the unit vertical vector (positive upward), whilst $\mathcal{D}_m$ represents an m-order viscosity/diffusion operator acting on the momentum and the mass transport, defined as follows (Winters & D'Asaro, 1997):

$$\mathcal{D}_m(\cdot) \equiv \begin{cases} \nu_{m,j}\partial_j^{2m} & \text{dissipation} \\ \kappa_{m,j}\partial_j^{2m} & \text{diffusion} \end{cases} ; \text{with } \nu_{m,j} = \kappa_{m,j} \equiv \frac{1}{T_{\mathcal{D}}}\left(\frac{L_j}{\pi n_j}\right)^{2m} ; \; j \in \{x, y, z\} \tag{4.2.2}$$

where $\nu_{m,j}$ and $\kappa_{m,j}$ are the m-order viscosity/diffusivity coefficient, respectively, whose physical dimensions are $\left[L^{2m}/T\right]$. The operator ∂_j^{2m} corresponds to the $2m$-order partial derivative with respect to the spatial coordinate j (with $j = x, y, z$). L_j and n_j are the computational domain size and the number of equally spaced grid points in the j^{th} direction. $T_{\mathcal{D}}$ is a time scale chosen by trial and error to minimize the range of damped scales while maintaining numerical stability (Winters & D'Asaro, 1997). The choice $m = 1$ results in the standard Navier-Stokes equations, which should be solved down to the Kolmogorov length scale which is barely possible given the available computing power. Alternatively, for example, the viscosity could be chosen by trial and error to be just large enough to damp the downscale energy transfer for a given problem resolved over a fixed number of grid points. However, if the goal is to allow the inertial subrange to be as broad as possible for a given grid resolution, then larger values of viscosity are inefficient and smaller values require finer grids to resolve the dissipative scales and maintain stability. Similar arguments apply for the m-order operators. We use $m = 3$ for this study and note that the use of this type of closure implicitly assumes a downscale energy cascade with the rate of energy transfer controlled by the nearly inviscid processes in the inertial subrange. This rate can then be measured at small scales by directly evaluating the kinetic energy dissipation

rate whose mathematical form depends on the value of m chosen as shown in the appendix 4.6.

We impose no-flux and free-slip boundary conditions on the top, bottom and sidewalls of the cylindrical domain to avoid having to resolve small viscous boundary layers. The initial condition of the IKW is constructed from the linear normal mode solution derived by Csanady (1967) for a discontinuous two-layer stratification in a cylindrical domain. This solution is written as

$$\eta_{\mathrm{i}}\left(t,r,\theta\right)/\eta_0 = I_1\left(\beta_1 \cdot r\right) \cdot \cos\left(\theta - \omega_1 t - \phi\right) \tag{4.2.3}$$

where $\eta_{\mathrm{i}}(t,r,\theta)$ is the modal structure of the interface displacement and $\beta_1 = R_{\mathrm{i}}^{-1}\sqrt{1-\sigma_1^2}$. The radial shape of the solution is characterized by the first-kind modified Bessel function of the azimuthal gravest mode, I_1 (Abramowitz & Stegun, 1965), while the temporal and azimuthal components are given by the cosine periodic function. The wave frequency, ω_1, and dimensionless frequency, $\sigma_1 = \omega_1/f$, of the IKW are obtained by solving the dispersion relation derived from the boundary condition for η_{i} at $r = R$ (Csanady, 1967; Stocker & Imberger, 2003):

$$1 - \sigma_1^2 \mathrm{M}^2 = 0 \;\; ; \;\; \text{with } \mathrm{M}^2 \equiv \beta_1 \cdot R \frac{I_0\left(\beta_1 \cdot R\right)}{I_1\left(\beta_1 \cdot R\right)} - 1. \tag{4.2.4}$$

From the linearized inviscid governing equations and solution (4.2.3), we obtain the density and velocity field for a discontinuous two-layer stratification (Csanady, 1982; Antenucci & Imberger, 2001). However, solution (4.2.3) cannot be directly used to specify the initial condition of an IKW in a smooth two-layer stratified fluid. Moreover, a derivation of continuous eigenfunctions after introducing a small transition scale δ_{i} into the density profile is also inconvenient because such solutions are both formally and practically restricted to have displacement amplitudes much smaller than δ_{i}. Here we wish to study the nonlinear transition regime, and waves in this regime have initial amplitudes substantially larger than δ_{i}.

For a given $\delta_{\mathrm{i}} \ll h_j, j = 1,2$, the linear, discontinuous solution (4.2.3) can be specified with an amplitude η_0 significantly larger than δ_{i}. We prescribe such a solution, expecting that its subsequent evolution will be nonlinear. We then smooth out the discontinuities by allowing the density and momentum to diffuse over a finite time scale such that the interface thickness is of $\mathcal{O}(\delta_{\mathrm{i}})$. In contrast, solving the linear equations for a continuously varying but sharply transitioning stratification produces overturns in the density field when η_0 approaches or exceeds δ_{i} (see e.g. Kundu *et al.* (2012): Chapter 13, on normal modes in a continuously stratified layer).

The equations of motion (4.2.1), with the smoothed version of the initial condition (4.2.3), are numerically solved using the three-dimensional spectral model **flow_solve** (Winters & de la Fuente, 2012). The model is based on expansions in terms of trigonometric functions of the dependent variables over regular meshes in a cubic domain (L_x, L_y, L_z), inside which a cylindrical domain (R, H) is immersed. The variables are expanded in cosine or sine series in each spatial component, depending on the boundary conditions to be satisfied. For example, in the vertical direction, the horizontal velocity components, u and v, and the density field, ρ, are expanded in cosine series while the vertical velocity component, w, is expanded in sine series to satisfy the free-slip wall and no-flux condition on the top and bottom boundaries. The boundary conditions on the curved sidewall are implemented using an immersed boundary approach introduced by Winters & de la Fuente (2012).

Symbol	Dimensions	Property	Definition	Location
$\eta_{\mathrm{i}}(t,\vec{x})$, $\eta_{\mathrm{i}}(t,r,\theta)$	m	Vertical displacement of density interface in Cartesian and polar coordinates		4.1, figure 4.1.1, (4.2.3)
η_0	m	Initial wave amplitude	$\max\{\eta_{\mathrm{i}}(t=0,\vec{x})\}$	4.1, figure 4.1.1
h_ℓ, $\ell=1,2$	m	Thickness of the ℓ^{th} layer	$h_1=0.07$, $h_2=0.13$	4.1, figure 4.1.1
H	m	Depth of the cylindrical basin	$h_1+h_2=0.2$	4.1, figure 4.1.1
η_0/h_1	–	Dimensionless amplitude	$\in[0.07,0.60]$	4.1, figure 4.1.1
δ_{i}	m	Length scale of the transition layer	≈ 0.02	4.2.1, figure 4.1.1
λ_k	m	wavelength of the internal Kelvin wave	$2\pi R$	4.2.2, (4.2.5)
ρ_ℓ, $\ell=1,2$	kg m^{-3}	Density of the ℓ^{th} layer	$\rho_1=1000$, $\rho_1=1015$	4.1, figure 4.1.1
$\Delta\rho$	kg m^{-3}	Density difference	$\rho_2-\rho_1=15$	4.1
g	m s^{-2}	Gravity acceleration	9.81	4.1, figure 4.1.1
g'	m s^{-2}	Reduced gravity acceleration	$(\Delta\rho/\rho_0)\,g\approx 0.147$	4.1
c_{i}	m s^{-1}	Linear internal celerity	$\sqrt{g'h_1h_2/H}\approx 0.082$	4.1
f	s^{-1}	Inertial frequency	0.361	4.1, figure 4.1.1
R	m	Radius of the cylindrical basin	0.9	4.1, figure 4.1.1
D	m	Diameter of the cylindrical basin	$2R=1.8$	4.1, figure 4.1.1
R_{i}	m	Internal Rossby radius of deformation	$c_{\mathrm{i}}/f\approx 0.225$	4.1, figure 4.1.1
$\vec{v}$	m s^{-1}	Velocity field	(u,v,w)	4.2.1, (4.2.1)
ρ_0	kg m^{-3}	Ambient reference density	1000	4.2.1, (4.2.1)
ρ	kg m^{-3}	Boussinesq density difference from ρ_0		4.2.1, (4.2.1)
p	Pa	Pressure field		4.2, (4.2.1)
L_j, $j=x,y,z$	m	Computational domain size in the j^{th} coordinate	$L_x\times L_y\times L_z=1.95\times 1.95\times 0.2$	4.2.1, (4.2.2)
n_j, $j=x,y,z$	–	Number of grid points in the j^{th} coordinate		4.2.1, (4.2.2), , Table 4.2
k_v	m^{-1}	Vertical grid wavenumber		4.2.3
k_r,k_θ	m^{-1}	Horizontal grid wavenumber in cylindrical coordinates		4.2.3
$k_{\delta_{\mathrm{i}}}$	m^{-1}	Wavenumber associated to the interfacial transition scale		4.2.3
k_h^{KH}	m^{-1}	Wavenumber of the most unstable interfacial wave	$\approx 2\pi/(7\delta_{\mathrm{i}})$	4.2.3
$\nu_{m,j}$	m^{2m} s^{-1}	Hyper-viscosity coefficient	$T_{\mathcal{D}}^{-1}\left(\frac{L_j}{\pi n_j}\right)^{2m}$	4.2.1, (4.2.2)
$\kappa_{m,j}$	m^{2m} s^{-1}	Hyper-diffusivity coefficient	$T_{\mathcal{D}}^{-1}\left(\frac{L_j}{\pi n_j}\right)^{2m}$	4.2.1, (4.2.2)
$T_{\mathcal{D}}$	s	Numerical damping time-scale		4.2.1, (4.2.2)
$\mathcal{D}_m(\cdot)$	s^{-1}	m-order viscosity/diffusion operator	$\begin{cases}\nu_{m,j}\partial_j^{2m} & \text{dissipation}\\ \kappa_{m,j}\partial_j^{2m} & \text{diffusion}\end{cases}$	4.2.1, (4.2.2)
I_1	–	First kind modified Bessel function of order 1		4.2.1, (4.2.3)
ϕ	rad	Phase of wave	0	4.2.1, (4.2.3)
ω_1	s^{-1}	Wave frequency of the Kelvin gravest mode	≈ 0.104	4.2.1, (4.2.3)
σ_1	–	Dimensionless wave frequency of the Kelvin gravest mode	$\omega_1/f\approx 0.288$	4.2.1, (4.2.4)
$\mathcal{B}_{\mathrm{i}}$	–	Burger number	$R_{\mathrm{i}}/R\approx 0.25$	4.2.2, (4.2.5)
T_k	s	Kelvin wave period	≈ 60.45	4.2.2, (4.2.5)
$\mathcal{T}_{sk}$	–	Steepening parameter	$\lambda_k/(\Delta c_{\mathrm{i}}T_k)\in[3.6,34.6]$	4.2.2, (4.2.5), Table 4.2
$\mathcal{T}_{\nu k}$	–	Damping parameter	$\eta_0^{2m}/(\nu_m T_k)\in[10^{-1},4\times10^4]$	4.2.2, Table 4.2
$\mathcal{T}_{\nu k}/\mathcal{T}_{sk}$	–	Ratio of advective to viscous forces	$\Delta c_{\mathrm{i}}\eta_0^{2m}/(\nu_m\lambda_k)\in[3\times10^{-3},10^4]$	4.2.2, Table 4.3
Re_m	–	Hyper-viscous Reynolds number	$\Delta c_{\mathrm{i}}\eta_0^{2m-1}/\nu_m$	4.2.2, (4.2.7)
Re	–	Reynolds number ($m=1$)	$\Delta c_{\mathrm{i}}\eta_0/\nu$	4.2.2, (4.2.8)
$\mathcal{N}$	s^{-1}	Buoyancy frequency	$\sqrt{g\rho_0^{-1}\partial_z\rho}$	4.2.2, (4.2.5)
$\mathcal{N}_0$	s^{-1}	Maximum buoyancy frequency	$\max\{\mathcal{N}(t=0,\vec{x})\}$	4.4.3
$T_{\mathcal{N}_0}$	s	Buoyancy period at the pycnocline	$2\pi/\mathcal{N}_0\approx 1$	4.2.3
$\mathcal{S}$	s^{-1}	Vertical shear in the horizontal velocity	$\sqrt{(\partial_z U)^2+(\partial_z V)^2}$	4.4.3
$\mathcal{J}$	–	Gradient Richardson number	$\mathcal{N}^2/\mathcal{S}^2$	4.2.2, (4.2.5)
$\mathcal{J}_0$	–	Gradient Richardson number at $t=0$	$\mathcal{J}(t=0,\vec{x})$	4.2.3, Table 4.2
T_{ns}	s	Total simulation time	$3T_k\approx 181.35$	4.2.3
ε_m	m^2 s^{-3}	Hyper-viscous kinetic energy dissipation rate	$\nu_m\lvert\nabla^m\vec{v}\rvert^2$	4.2.2, (4.2.10), Appendix 4.6, (4.6.4)
$\mathcal{I}_m$	–	Turbulence intensity parameter	$\mathcal{N}^{-1}\{(\varepsilon_m)^m/\nu_m\}^{2/(3m-1)}$	4.2.2, (4.2.10), Appendix 4.6, (4.6.9)
$\langle\mathcal{I}_m\rangle_H$	–	Vertical average of $\mathcal{I}_m$	$H^{-1}\int_0^H\mathcal{I}_m\mathrm{d}\tilde{z}$	4.4
$\langle\mathcal{I}_m\rangle_V$	–	Bulk average of $\mathcal{I}_m$	$V^{-1}\int_V\mathcal{I}_m\mathrm{d}\tilde{V}$	4.4.2, Table 4.3
$\langle\mathcal{I}_m\rangle_{V,T}$	–	Spatial and temporal average of $\mathcal{I}_m$	$(T_{ns})^{-1}\int_{T_{ns}}\left\{V^{-1}\int_V\mathcal{I}_m\mathrm{d}\tilde{V}\right\}\mathrm{d}\tilde{t}$	4.4.2
b	m s^{-2}	Buoyancy field	$(1-\rho/\rho_0)\,g$	4.2.2, (4.2.10), Appendix 4.7, (4.7.6)
z_*	m	Reference height in the minimum potential energy state of a fluid		4.2.2, (4.2.10), Appendix 4.7, (4.7.1)
$\mathcal{K}_m$	–	Diffusivity parameter	$\lvert\nabla^m b\rvert^2\cdot\lvert\mathrm{d}^m b/\mathrm{d}z_*^m\rvert^{-2}$	4.2.2, (4.2.10), Appendix 4.7, (4.6.8)
$\langle\mathcal{K}_m\rangle_V$	–	Bulk average of $\mathcal{K}_m$	$V^{-1}\int_V\mathcal{K}_m\mathrm{d}\tilde{V}$	4.4.2, Table 4.3
$\langle\mathcal{K}_m\rangle_{V,T}$	–	Spatial and temporal average of $\mathcal{K}_m$	$(T_{ns})^{-1}\int_{T_{ns}}\left\{V^{-1}\int_V\mathcal{K}_m\mathrm{d}\tilde{V}\right\}\mathrm{d}\tilde{t}$	4.4.2
z_{i}	m	Height of the density interface ($\rho(t,\vec{x})=\Delta\rho/2$)		4.4
$\mathcal{A}_\theta$	–	Area defined by $z/H\in[0,1]$, $\theta\in[0,2\pi]$ and $r/R=0.98$		4.4.3
$\vec{\omega}$	s^{-1}	Vorticity field	$\nabla\times\vec{v}$	4.4.3
ℓ_K	m	Hyper-viscous Kolmogorov length scale	$\{\nu_m^3/\varepsilon_m\}^{1/(6m-2)}$	Appendix 4.6, (4.6.5)
ℓ_O	m	Ozmidov length scale	$\{\varepsilon_m/\mathcal{N}^3\}^{1/2}$	Appendix 4.6, (4.6.6)

Table 4.1: Glossary of symbols used in text.

4.2.2 Dimensionless numbers

The initial dynamics of the IKW are parametrized by four dimensionless parameters:

$$\mathcal{B}_\mathrm{i} \equiv \frac{R_\mathrm{i}}{R} \quad ; \quad \mathcal{T}_{sk} \equiv \frac{\lambda_k}{\Delta c_\mathrm{i} T_k} \quad ; \quad \mathcal{T}_{\nu k} \equiv \frac{\eta_0^{2m}}{\nu_m T_k} \quad ; \quad \mathcal{J} \equiv \frac{\mathcal{N}^2}{\mathcal{S}^2}. \tag{4.2.5}$$

Here $\mathcal{B}_\mathrm{i}$ is the Burger number (Antenucci & Imberger, 2001) that characterizes the influence of rotation. If $\mathcal{B}_\mathrm{i} \geq 1$, rotation is weak while if $\mathcal{B}_\mathrm{i} < 1$, rotational effects are important. In the IKW case, as $\mathcal{B}_\mathrm{i} \to 0$, the wave energy becomes concentrated near the boundary with the fluid motions parallel to the shoreline.

$\mathcal{T}_{sk}$ is the steepening parameter and it is interpreted as the rate at which the spatial differences of the internal wave celerity induced by η_0 lead to wavefronts and nonlinearities, $T_s \sim \lambda_k/\Delta c_\mathrm{i}$, over an IKW period T_k. Therefore, $\mathcal{T}_{sk}$ quantifies how fast an IKW with amplitude η_0 tends to produce a nonlinear wavefront (Boegman *et al.*, 2005b; de la Fuente *et al.*, 2008) and thus to concentrate energy at smaller length scales in the near-shore region.

$T_{\nu k} \sim \eta_0^{2m}/\nu_m$ is the dissipation time scale for motions of vertical scale η_o and $\mathcal{T}_{\nu k}$ gives the ratio of this time scale to the Kelvin wave period. To quantify the relative importance of viscous to nonlinear effects in the context of this flow we have defined a dimensionless number that is the ratio of the (hyper-)viscous time scale to the nonlinear steepening time of the primary Kelvin wave:

$$\frac{\mathcal{T}_{\nu k}}{\mathcal{T}_{\nu k}} \equiv \frac{\Delta c_\mathrm{i} \eta_0^{2m-1}}{\nu_m} \left(\frac{\eta_0}{\lambda_k} \right). \tag{4.2.6}$$

In this sense, this ratio is similar to the standard Reynolds number that relates inertial to viscous forces. The definition of the m-order hyper-viscous Reynolds number is (Lamorgese *et al.*, 2005; Spyksma *et al.*, 2012)

$$Re_m \equiv \frac{\Delta c_\mathrm{i} \eta_0^{2m-1}}{\nu_m}, \tag{4.2.7}$$

which formally reduces to the classic viscous Reynolds number when $m = 1$:

$$Re \equiv \frac{\Delta c_\mathrm{i} \eta_0}{\nu_m}. \tag{4.2.8}$$

High values of Re_m imply energetic regimes, dominated by inertial forces, whereas low values of Re_m imply flow regimes dominated by (hyper-)viscous forces. The parameter $\mathcal{T}_{\nu k}/\mathcal{T}_{\nu k}$ can be written in terms of the hyper-viscous Reynolds number as follows:

$$\frac{\mathcal{T}_{\nu k}}{\mathcal{T}_{sk}} \equiv Re_m \left(\frac{\eta_0}{\lambda_k} \right). \tag{4.2.9}$$

Note that η_0/λ_k is the aspect ratio of the Kelvin wave and it is a measure of its hydrostaticity. Steeper, non-hydrostatic waves are more nonlinear and enhance the energy transfer to small scales.

$\mathcal{J}$ is the gradient Richardson number, with $\mathcal{N}$ the buoyancy frequency and $\mathcal{S}$ the vertical shear in the horizontal velocity (Miles, 1961). In our problem, both $\mathcal{N}$ and $\mathcal{S}$ have maxima at the height of the density interface but the magnitude and spatial distribution of $\mathcal{J}$ will depend both on η_0 and $\mathcal{B}_\mathrm{i}$. The maximal shear $\mathcal{S}$, for example, occurs in the shore region, near the maximum vertical displacement of

the interface. For a fixed rotation regime, the initial minimum value of $\mathcal{J}$ decreases as η_0 is increased.

The dissipation and mixing involved in the IKW evolution are characterized in terms of dimensionless turbulence activity parameters that quantify the dissipation rates of kinetic energy and buoyancy variance given by

$$\mathcal{I}_m \equiv \frac{1}{\mathcal{N}^2}\left\{\frac{(\varepsilon_m)^m}{\nu_m}\right\}^{2/(3m-1)} \quad , \quad \mathcal{K}_m \equiv |\nabla^m b|^2 \cdot \left|\frac{\mathrm{d}^m b}{\mathrm{d}z_*^m}\right|^{-2} , \tag{4.2.10}$$

where $\mathcal{I}_m$ denotes the turbulence intensity parameter expressed in terms of the hyper-viscosity approach of the kinetic energy dissipation rate, ε_m, and derived from the ratio of the Ozmidov and Kolmogorov scales (see Appendix 4.6). This parameter can be interpreted as the destabilizing effects of turbulent stirring compared to the stabilizing effects produced by the combined action of hyper-viscosity and buoyancy. Finally, $\mathcal{K}_m$ is the ratio of the diapycnal flux and a reference laminar diffusive flux, both in terms of the hyper-diffusion approach and the buoyancy, b. This diffusivity parameter measures the increase in diffusive flux due to turbulent stirring and straining relative to the laminar, diffusive flux with the same background buoyancy that is not stirred or strained (see appendix 4.7).

4.2.3 Set of numerical experiments

We consider a single rotation regime, $\mathcal{B}_\mathrm{i} = 0.25$, and a range of dimensionless amplitudes $\eta_0/h_1 \in [0.07, 0.60]$ and aspect ratios $\eta_0/\lambda_k \in [8.8\times10^{-4}, 7.5\times10^{-3}]$ that allow $\mathcal{T}_{sk} \in [3.6, 34.6]$, $\mathcal{T}_{\nu k} \in [10^{-1}, 4\times10^4]$ and initial minimum values of $\mathcal{J}$ between $\min\{\mathcal{J}_0\} = 31.86$, for $\eta_0/h_1 = 0.07$, and $\min\{\mathcal{J}_0\} = 0.13$, for $\eta_0/h_1 = 0.60$. With these parameters, we have performed six numerical experiments using spatial and temporal scales similar to those used in recent laboratory experiments carried out in a rotating table by Ulloa *et al.* (2014). The dimensions of the domain are $L_x \times L_y \times L_z = 1.95\times1.95\times0.2\,\mathrm{m}^3$, and in its interior there is a circumscribed cylinder of radius $R = 0.9$ m and depth $H = h_1 + h_2 = 0.07\,\mathrm{m} + 0.13\,\mathrm{m} = 0.2\,\mathrm{m}$. The difference of densities is $\Delta\rho = \rho_2 - \rho_1 = 15\,\mathrm{kg/m}^3$, the effective thickness of the interfacial transition is $\delta_\mathrm{i} \approx 0.02\,\mathrm{m}$, and the inertial frequency $f = 0.361\,\mathrm{hz}$, with an IKW period of $T_k = 60.45\,\mathrm{s}$ and a total simulation time $T_{ns} = 3T_k = 182\,\mathrm{s}$. Figure 4.2.1 shows that the initial transition layer is resolved by about 12 - 14 grid points. The horizontal wavelength of the most unstable mode for a smooth, sheared density transition is about π times the interface thickness (see e.g., Kundu *et al.*, 2012, Section 11.7, p. 506). This corresponds to about 10 - 11 times our horizontal grid spacing and so the most unstable mode is resolved on our spatial grid, though significantly smaller motions are not. Table 4.2 summarizes the parameters used in the numerical experiments.

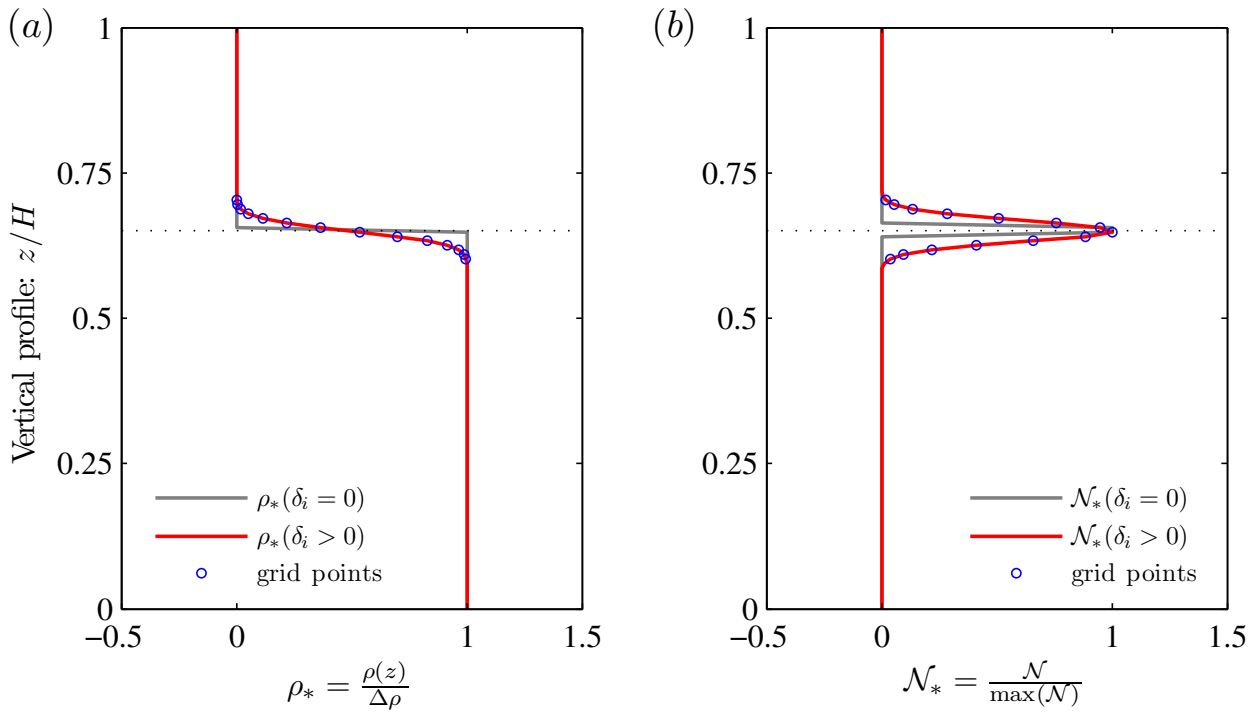

Figure 4.2.1: Density, $\rho(z)/\rho$, and buoyancy frequency, $\mathcal{N}(z)/\max(\mathcal{N})$, profiles in the initial condition of a discontinuous two-layer stratification $\delta_\mathrm{i} = 0$ (grey line) and a smooth two-layer stratification $\delta_\mathrm{i} > 0$ (red line) after a vertical diffusion over a time interval t_{δ_i}. The blue circles denote the equidistant grid points along the transition layer.

Exp	η_0/δ_i	η_0/h_1	η_0/λ_k	$\mathcal{B}_\mathrm{i}$	$\mathcal{T}_{sk}$	$\mathcal{T}_{\nu k}$	$\mathcal{T}_{\nu k}/\mathcal{T}_{sk}$	$\min_{z\sim z_\mathrm{i}}\{\mathcal{J}_0\}$	$\{n_x, n_y, \mathrm{n_z}\}$
1	1.0	0.07	8.8×10^{-4}	0.25	3.5×10^{1}	10^{-1}	3×10^{-3}	31.86	$321, 321, 129$
2	2.5	0.18	2.2×10^{-3}	0.25	1.4×10^{1}	2.7×10^{1}	2×10^{0}	3.04	$321, 321, 129$
3	5.3	0.38	4.7×10^{-3}	0.25	6.2×10^{0}	2.5×10^{3}	4×10^{2}	0.58	$321, 321, 129$
4	6.6	0.47	5.8×10^{-3}	0.25	4.9×10^{0}	8.8×10^{3}	2×10^{3}	0.30	$321, 321, 129$
5	7.5	0.54	6.7×10^{-3}	0.25	4.2×10^{0}	2.0×10^{4}	5×10^{3}	0.19	$321, 321, 129$
6	8.4	0.60	7.5×10^{-3}	0.25	3.6×10^{0}	4.0×10^{4}	10^{4}	0.13	$513, 513, 129$

Table 4.2: Summary of dimensionless parameter of experimental set.

4.3 Dynamic regimes

Figure 4.3.1 illustrates time series of a density profile at $r/R = 0.98$ and $\theta = 0$ where $\eta_i\,(t=0) \approx \eta_0$, and the power spectral density (PSD) of the density interface displacement $\eta_i\,(t, 0.98 \cdot R, 0)$. The IKW response is classified in four distinct regimes: damped linear (DLR), nonlinear (NLR), nonlinear/ non-hydrostatic (NHR) and laminar-turbulent transition regime (TR). The regimes have been defined in terms of their dynamics characteristics $(\mathcal{T}_{sk}, \mathcal{T}_{\nu k}, \mathcal{J})$ and through the visual inspection of the density field evolution, in similar terms as Horn *et al.* (2001) classified the degeneration of large scale internal waves in a non-rotating basin. We examine each regime in the follow subsections.

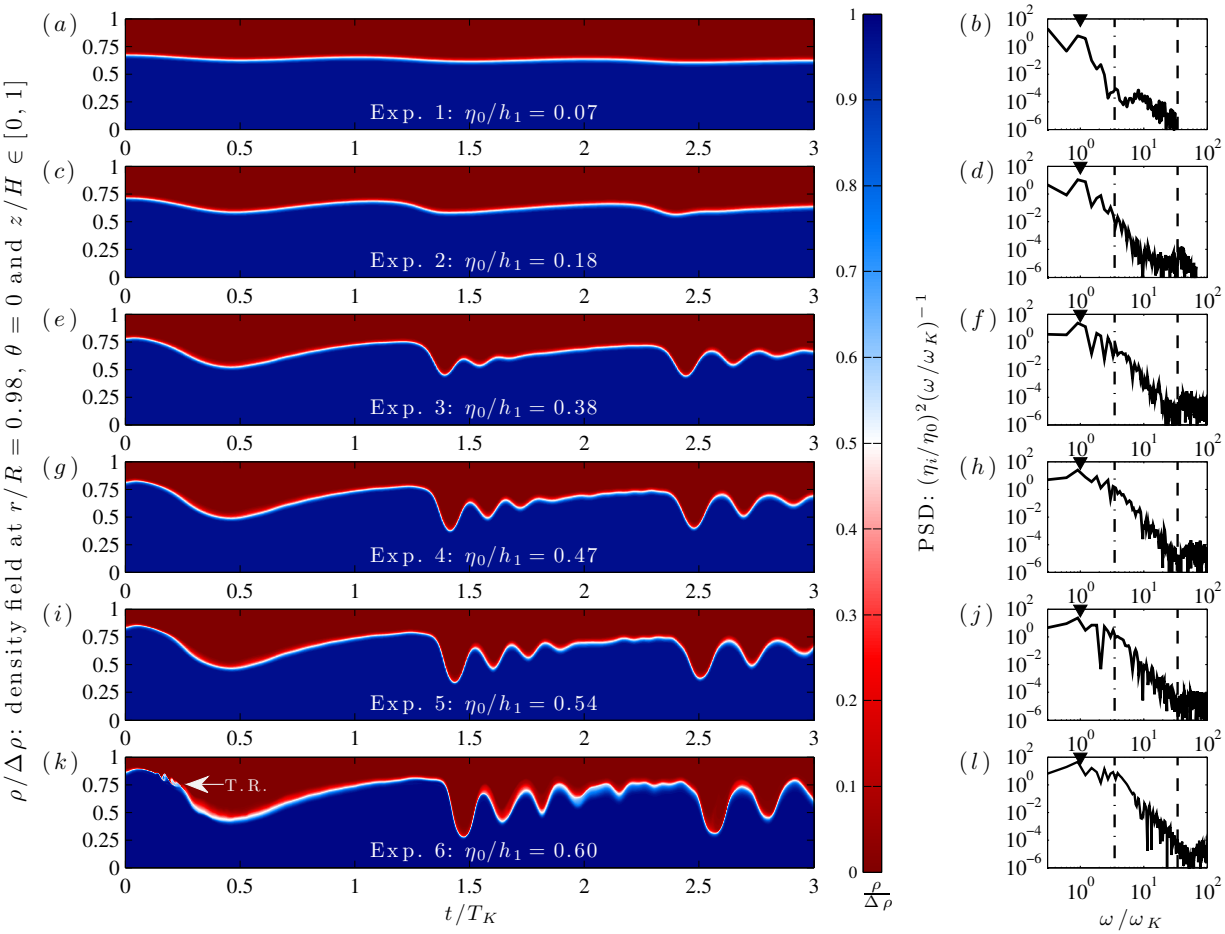

Figure 4.3.1: Left panels: time series of density field along the vertical profile where the maximum wave amplitude is achieved. Right panels: power spectral density of vertical displacement of density interface η_i; Kelvin wave frequency: ▼, Inertial frequency (f/ω_k): $\cdot-$ (dot-dash line), Initial buoyancy frequency $(\mathcal{N}_0/\omega_K)$:$--$(dash line). T.R., transition regime.

4.3.1 Damped linear regime (DLR)

The DLR is characterized by the evolution of an IKW that retains most of its initial linear features, with negligible nonlinear steepening and strongly controlled by viscosity. This regime describes the

results of experiment 1 shown in figures 4.3.1(a, b); in this case, $\eta_0/h_1 = 0.07$ ($\eta_0/\delta_{\mathrm{i}} \approx 1.0$), $\mathcal{T}_{\nu k}/\mathcal{T}_{sk} \approx 3 \times 10^{-3} < 1$ and $\min\{\mathcal{J}_0\} \approx 31.86$, which suggests an extremely viscous flow with a negligible steepening capacity and a strong hydrodynamic stability in the density interface. Therefore a linear and damped IKW dynamics along the $3T_k$ periods is expected. The PSD in figure 4.3.1(b) shows a single strong energy peak at $\omega/\omega_k = 1$, indicating that the initial IKW mode stored the energy of the flow.

4.3.2 Nonlinear regime (NLR)

The NLR is characterized by weak nonlinear degeneration, without dispersion of the IKW (in the KdV theory sense). This regime starts with the IKW steepening, as a consequence of a wave amplitude large enough to induce significant changes in the wave celerity, leading the wavefront and the formation of a solitary-type wave (Fedorov & Melville, 1995; de la Fuente *et al.*, 2008). This regime describes the results of experiment 2 shown in figure 4.3.1(c, d); in this case $\eta_0/h_1 = 0.18$, $\mathcal{T}_{\nu k}/\mathcal{T}_{sk} \approx 1.9 > 1$ and $\min\{\mathcal{J}_0\} \approx 3.04$, and therefore we expect a weakly nonlinear steepening controlled by viscosity and a stable flow around the density interface. In fact, figure 4.3.1(c) shows a slightly steep wavefront after the first wave period and a solitary-type wave structure around $t/T_k \approx 2.45$. The PSD in figure 4.3.1(d) shows a wider energy cascade due to transfer of energy involved in the weakly nonlinear degeneration, with a main energy peak at $\omega/\omega_k = 1$, and two lower peaks of sub-inertial frequencies attributed to sub-azimuthal Kelvin waves (see the dash-dot line).

4.3.3 Nonlinear and non-hydrostatic regime (NHR)

Nonlinear steepening and non-hydrostatic dispersion of the initial IKW (in the KdV theory sense) characterize the NHR. As the wave steepens, its azimuthal length scale decreases until the non-hydrostatic terms can be important enough to balance the nonlinear steepening, avoiding the wave breaking (Helfrich & Melville, 2006) and leading the degeneration of the IKW into a package of solitary-type waves (Grimshaw, 1985). This process induces an important energy cascade from the basin scale to smaller scales. The NHR regime is identified in experiments 3, 4, 5 and 6 (see figures 4.3.1e$-l$). In these experiments the Reynolds number increases from $\mathcal{T}_\nu/\mathcal{T}_s \approx 4 \times 10^2$, for $\eta_0/h_1 = 0.38$, to $\mathcal{T}_{\nu k}/\mathcal{T}_{sk} \approx 10^4$, for $\eta_0/h_1 = 0.60$. Increasing $\mathcal{T}_\nu/\mathcal{T}_s$ corresponds to increasing nonlinearity and concentration of energy at smaller scales. Experiments 3 and 4 show hydrodynamic stable flows in the density interface region, with $\min\{\mathcal{J}_0\} \approx 0.58$ and $\min\{\mathcal{J}_0\} \approx 0.30$, respectively, whereas experiments 5 and 6 show evidence of the emergence of hydrodynamic interfacial instabilities, with $\min\{\mathcal{J}_0\} \approx 0.20$ and $\min\{\mathcal{J}_0\} \approx 0.13$, respectively.

4.3.4 Laminar-turbulent transition regime (TR)

The TR is characterized by the growth and occurrence of interfacial instabilities. Depending on how energetic the shear flow is, the instabilities can grow and generate turbulent patches in the density interface region or can be damped. The hydrodynamic stability of the IKW sheared flow can be studied via the gradient Richardson number, $\mathcal{J}$, whose critical value $\mathcal{J} = 0.25$ (Miles, 1961) is neither a necessary nor a sufficient condition to trigger interfacial instabilities in our sheared-type flow, but it is still a very useful criterion that can give us an order of magnitude. In our results only two

experiments show the presence of interfacial instabilities, experiments 5 and 6, with $\min\{\mathcal{J}_0\} \approx 0.20$ and $\min\{\mathcal{J}_0\} \approx 0.13$, respectively. Only they have initial $\mathcal{J} < 0.25$. Both experiments exhibit the emergence of Kelvin-Helmholtz-type billows on the wavefront of strongly nonlinear IKWs ($\mathcal{T}_{\nu k}/\mathcal{T}_{sk} \sim 5 \times 10^3 - 10^4$). However, the results of experiment 5 show fast damping of the interfacial instabilities, while the results of experiment 6 shows a complex spatial and temporal dynamic, in which large scales, attributed to the IKW and internal solitary-type waves, coexist and interplay with turbulent small scales, associated with interfacial instabilities/breaking and turbulent patches.

The first three regimes have been analysed in previous numerical (de la Fuente *et al.*, 2008; Sakai & Redekopp, 2010) and experimental studies (Wake *et al.*, 2005; Ulloa *et al.*, 2014), whereas the TR on IKWs has been observed only in field data (Lorke, 2007; Preusse *et al.*, 2010) and to date in numerical experiments.

4.4 Internal Kelvin wave: transition from laminar to turbulent regime

Hereafter we focus on the spatial and temporal evolution of the IKW in the TR (analysing results of experiment 6), aiming to link the dynamic wave response with turbulent activity. Figure 4.3.2 shows the evolution of the vertical velocity, $w(t, r, \theta, z)$, at the density interface z_i to illustrate the strongly nonlinear dynamics of the IKW in experiment 6. Here $z_\mathrm{i}(t)$ is defined as the vertical position of the $\rho\,(t, \vec{x}) = \Delta\rho/2$ iso-scalar surface. Figure 4.3.2(a) shows the initial condition of the IKW ($t/T_k = 0$). The degeneration of the IKW begins with the emergence of instabilities of Kelvin-Helmholtz (KH) type on the wavefront that starts to steepen at $t/T_k = 0.128$ (see figure 4.3.2b); it is in this region where the minimum Richardson number, $\mathcal{J} \approx 0.13$, is achieved. Figures 4.3.2(c) and 4.3.2(d) ($t/T_k \in [0.25, 0.5]$) show the formation of a turbulent patch induced by the breakdown of the KH type billows; this patch evidences a slight spread along the azimuthal and radial axes. Figure 4.3.2(d) shows the formation of the first solitary-type wave around $t/T_k \in [0.5, 0.625]$, while figures 4.3.2(e) and 4.3.2(f) show a solitary wave train confined to the near-shore region around $t/T_k \in [0.75, 1.0]$. After the first IKW period (see figures 4.3.2f, g) the leading wave starts to interact with the pre-existing turbulent patch. This interaction is accompanied by the regrowth of interfacial instabilities upstream of the wavefront and a subsequent interfacial turbulent wake on the solitary wave train (see figure 4.3.2g). The regrowth of interfacial instabilities generate a new turbulent patch that holds the same azimuthal location while it is vertically advected upward and downward by the solitary wave train (see figure 4.3.2h). During and after the interaction between the large internal waves and the turbulent patch, inertial waves of different scales are radiated to the offshore region (see figures 4.3.2$h-k$). At $t/T_k = 3$ (see figure 4.3.2l) there is no longer evidence of the initial IKW; the internal waves in the near shore region have decayed in amplitude, whilst a range of smaller length scales have been excited in the interior. During the first three IKW periods we observe that different nonlinear processes coexist, enhancing the degeneration of the initial long wave and promoting a forward energy cascade.

4.4.1 Spatialtemporal distribution of turbulence

Figure 4.4.1 shows the vertical average of the turbulence intensity parameter, $\langle \mathcal{I}_m \rangle_H$; the dashed line defines the radial position of the internal Rossby radius of deformation, R_i, from the boundary to the interior.

Figure 4.4.1(a) shows the initial distribution of $\langle \mathcal{I}_m \rangle_H$ induced by the IKW itself. Kinetic energy dissipation is concentrated within R_i and decays to low values towards the centre of the domain. The nonlinear dynamics of the IKW induces distinct zones of elevated values in the near-shore region, associated with turbulent patches produced by the breakdown of interfacial instabilities (see figures 4.4.1b – d). As the initial IKW degenerates, the turbulence intensity increases at the front of each

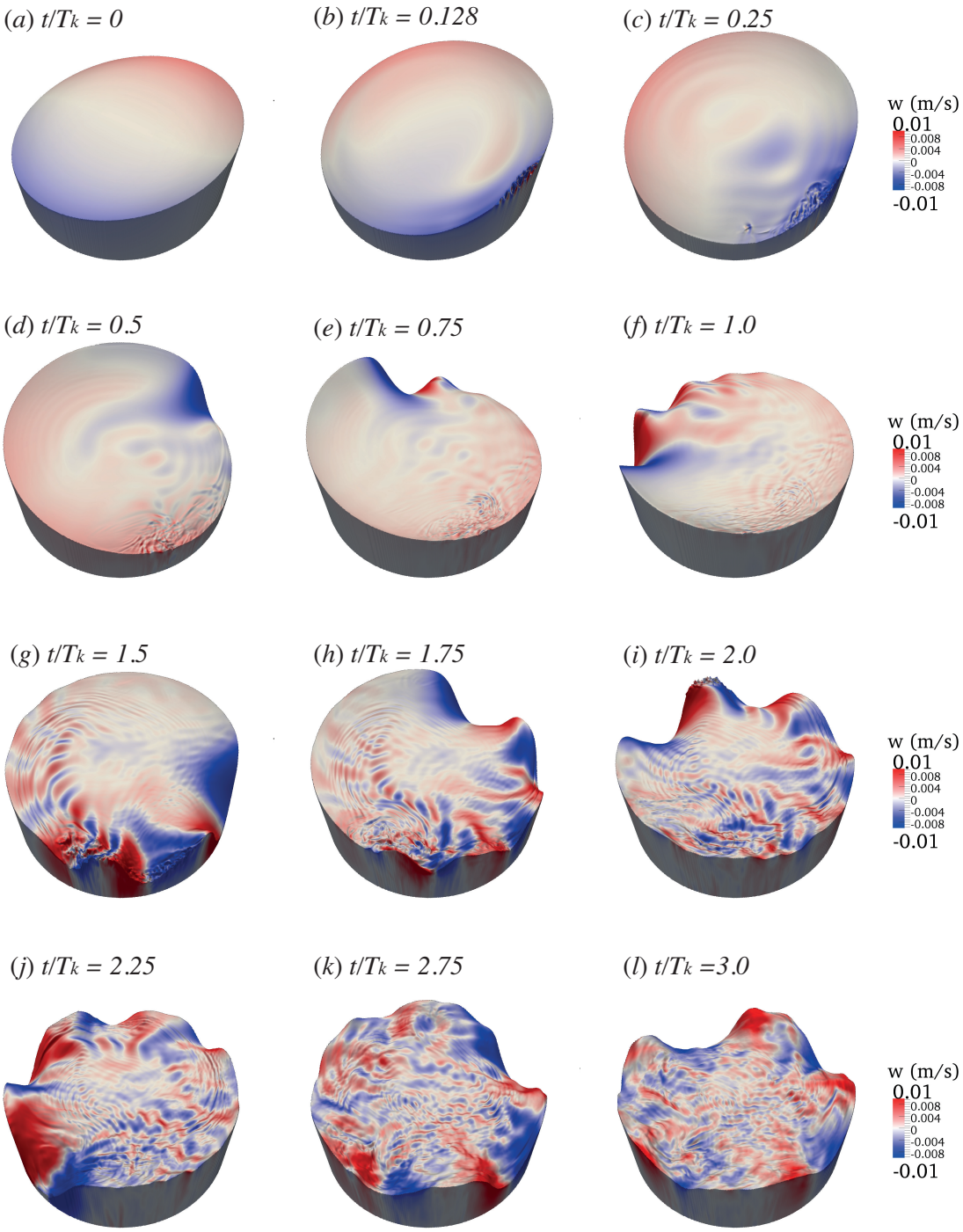

Figure 4.3.2: Results of Exp. 6: evolution in time $t/T_k \in [0, 3]$ of the vertical velocity w at the density interface region $\rho(t, \vec{x}) = \Delta\rho/2$.

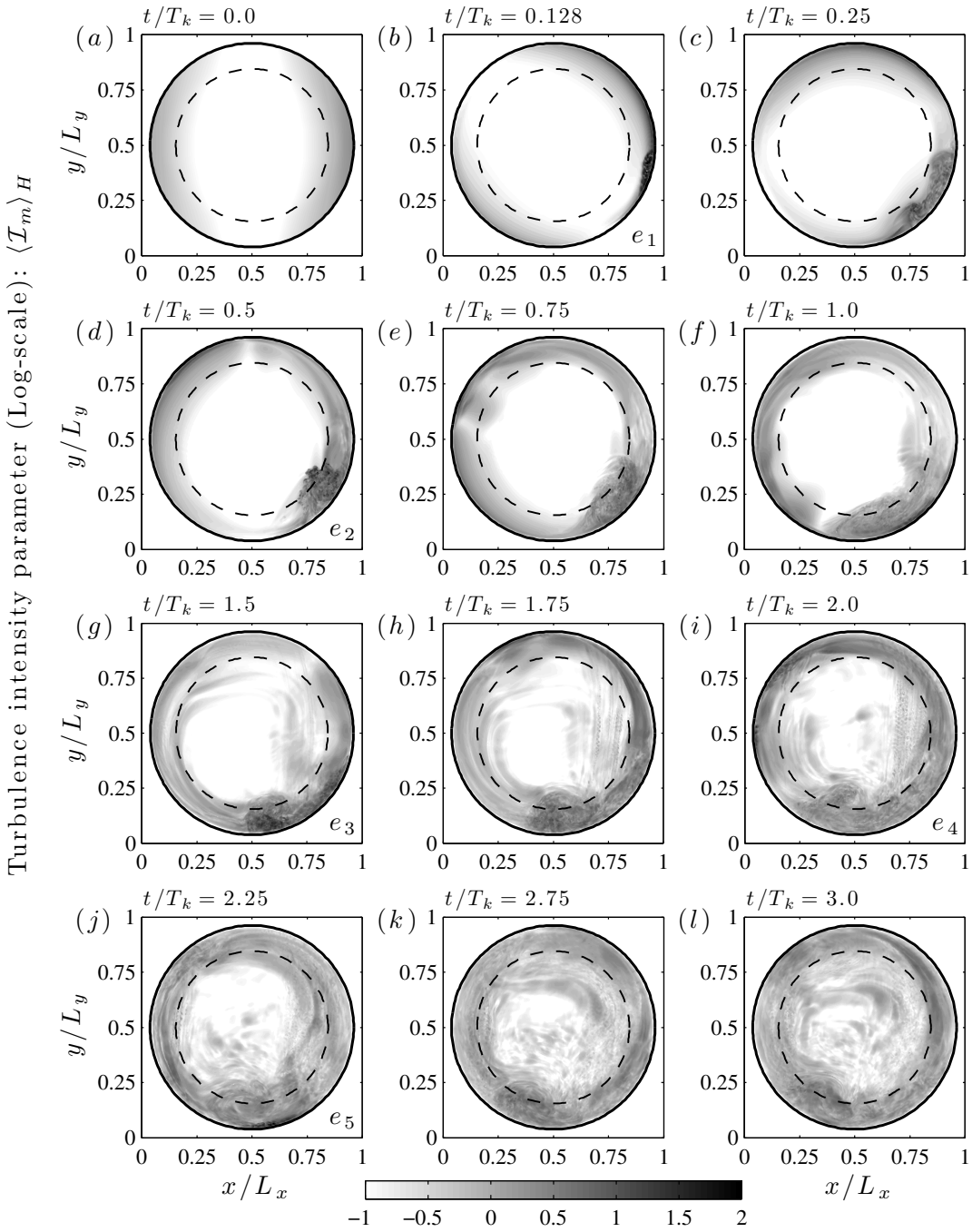

Figure 4.4.1: Results of experiment 6: spatialtemporal distribution of the turbulent intensity, $\langle \mathcal{I}_m \rangle_H$.

solitary-type wave along the shore region (see figures 4.4.1d $-$ f) achieving values of $\langle \mathcal{I}_m \rangle_H \sim \mathcal{O}\left(10^2\right)$, while most of the offshore region shows a low activity with values of $\langle \mathcal{I}_m \rangle_H \sim \mathcal{O}\left(10^{-1}\right)$. However, after the first period, and particularly after the strong reactivation of the pre-existing turbulent patch, there is a steady increase of $\langle \mathcal{I}_m \rangle_H$ to the interior of R_{i}, with values in the range $\mathcal{O}\left(10^0\right) \leq \langle \mathcal{I}_m \rangle_H \leq \mathcal{O}\left(10^1\right)$ (see figures 4.4.1$f-h$). This process is again observed after the second period (see figure 4.4.1j). After three periods elevated values of $\langle \mathcal{I}_m \rangle_H$ are distributed throughout the domain (see figures 4.4.1k, l). Nevertheless, there are clear differences in the intensity between the near-shore and interior regions,

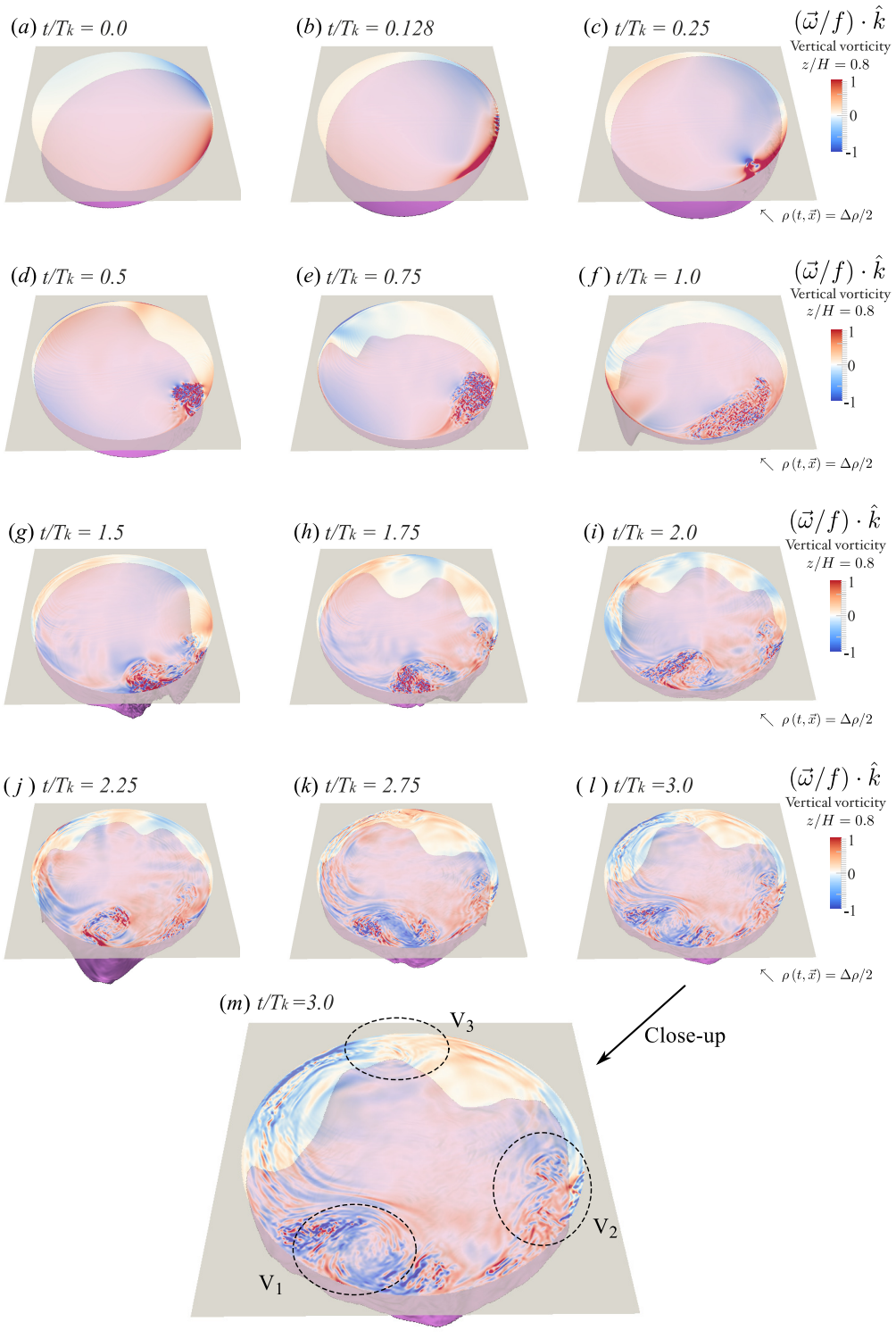

Figure 4.4.2: Results of experiment 6: spatialtemporal distribution of the vertical vorticity, $(\vec{\omega}/f)\cdot\hat{k}$, at $z/H = 0.80$.

where the internal Rossby radius of deformation (dashed-line) seems to define a transition length scale of the turbulent activity along the radial component.

The azimuthal distribution of the turbulence intensity parameter shows features of baroclinic instabilities. This is also observed in figure 4.4.2, which shows the relative vertical vorticity, $\vec{\omega} \cdot \hat{k}$, normalized by f at $z/H = 0.8$ (horizontal plane) and the density interface structure $\rho(t, \vec{x}) = \Delta\rho/2$ in purple. Initially we observe the formation of one turbulent patch in the shore region around $t/T_k = 0.25$ (see figure 4.4.2c), which grows and spreads along the shore until approximately the first period (see figure 4.4.2d $- f$). After the first period, the initial turbulent patch is separated into two (see figure 4.4.2d, h, i) that also remain trapped on the shore, and a third vortex structure grows on the shore region during the second period (see figure 4.4.2k, l). It is observed that turbulent patches tend to aggregate in large horizontal motions that scale with R_i. Figure 4.4.2(m) shows a close-up of the vertical vorticity at $t/T_k = 3$, where three large-scale vortex-type motions are identified in the near-shore region (see dashed ellipses). We can study the existence of baroclinic instability via a simplified model. Pedlosky (1970) considered a quasi-geostrophic two-layer model in an inviscid flow rotating on an f-plane, with uniform velocities U_1 and U_2 in each layer ($U_1 \neq U_2$). The flow is unstable to disturbances with horizontal wavelengths, λ, larger than πR_i (See e.g., Pedlosky, 1987, Chapter 7, p. 556). Then, considering the azimuthal wavelength of the IKW, $\lambda_k = 2\pi R$, and the internal Rossby radius here adopted, it is obtained that the flow induced by the IKW admits the growth of baroclinic instabilities because $\pi R_\mathrm{i}/\lambda_k = \mathcal{B}_\mathrm{i}/2 = 0.125$. In addition, the interaction between the vortex-type motions and the vertical shear flow driven by the internal gravity waves could be supporting the emergence of baroclinic instabilities (Sakai, 1989; Gula *et al.*, 2009; Flór *et al.*, 2011). Note that these large-scale vortex motions are not observed in the interior of the basin.

Figure 4.4.3 shows the time series of extreme and bulk values of the turbulence intensity parameter, within and outside R_i. The red vertical lines identify events ($\mathrm{e_i}$) with high turbulent activity (local maxima) in the time series of experiment 6 ($-\bullet-$), whose horizontal positions can be identified in figure 4.4.1(b, d, g, i, j). In figure 4.4.3(a) the values of $\min\{\mathcal{I}_m\}$ are comparable for all experiments except experiments 1 and 2 (blue lines), with $\min\{\mathcal{I}_m\} \sim \mathcal{O}(10^3)$. Values of $\max\{\mathcal{I}_m\}$, however, increase with increasing nonlinearity, causing the separation of the time series between $\mathcal{O}(10^{-1}) \leq \max\{\mathcal{I}_m\} \leq \mathcal{O}(10^2)$ (red lines). In the case of experiment 6, peak turbulence intensity values are $\mathcal{O}(10^5)$ times the background laminar value. These results show a significant heterogeneity of $\mathcal{I}_m$ in both time and space. We have divided the domain into two volumes: V_{in} and V_{out} denote the volumes within and outside R_i, respectively, and over these volumes bulk quantities of $\mathcal{I}_m$ have been calculated. Within R_i (see figure 4.4.3b), time series of $\langle\mathcal{I}_m\rangle_{V_{in}}$ show distinct differences between each experiments. The highest values and the most interesting temporal fluctuations are observed in experiment 6 ($-\bullet-$). Outside R_i (see figure 4.4.3c), time series show that $\langle\mathcal{I}_m\rangle_{V_{out}}$ tends to grow as a function of time, and shows only one peak at $\mathrm{e_2}$ attributed to the formation of the first turbulent patch; figure 4.4.1(d) shows that this event ($\mathrm{e_2}$) affects a small region outside R_i. Comparing both volumes, early in time, the distinction between the turbulent activity within and outside R_i is quite important, but by the later times in the experiments, $\mathcal{I}_m$ is only about a factor of 3 higher (see figures 4.4.3(b) and 4.4.3(c) for the most energetic case) and the tendency is to reduce the difference between both regions.

4.4.2 Turbulence intensity and effective diffusivity

Figures 4.4.4(a) 4.4.4(b) show time series of the bulk averages of the turbulence intensity parameter, $\langle\mathcal{I}_m\rangle_V$, and the diffusivity parameter, $\langle\mathcal{K}_m\rangle_V$, respectively.

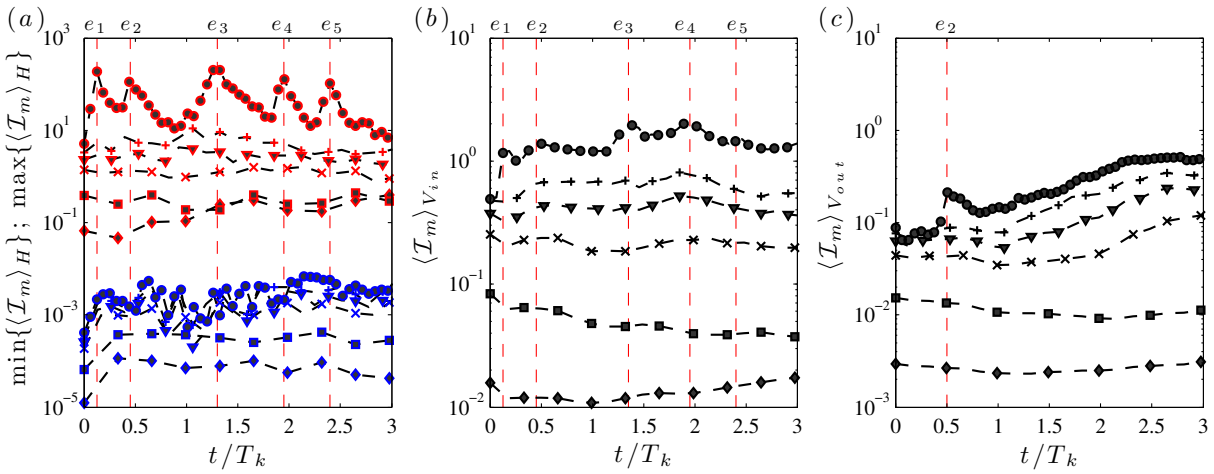

Figure 4.4.3: Evolution in time (scaled by T_K) of (a) the maxima and minima values of the turbulence intensity parameter, (b) the bulk turbulence intensity parameter within R_i, $\langle\mathcal{I}_m\rangle_{V_{in}}$, and ($c$) the bulk turbulence intensity parameter outside R_i, $\langle\mathcal{I}_m\rangle_{V_{out}}$. Legend: Exp. 6: $-\bullet-$; Exp. 5: $-+-$; Exp. 4: $-\blacktriangledown-$; Exp. 3: $-\times-$; Exp. 2: $-\blacksquare-$; Exp. 1: $-\blacklozenge-$.

The temporal structure of $\langle\mathcal{I}_m\rangle_V$ (see figure 4.4.4(a)) is forced by the turbulent activity in the near-shore region (see peaks denoted by vertical dashed lines) but with lower magnitudes because of the low turbulent activity on the offshore region. Meanwhile, the time series of $\langle\mathcal{K}_m\rangle_V$ can be clustered into three groups (see figure 4.4.4(b)): a first group with experiments 1-3, a second group with experiments 4-5 and a third group with experiment 6. The first group contains experiments with the lowest and almost constant value of $\langle\mathcal{K}_m\rangle_V$, the second includes experiments with weak fluctuations of $\langle\mathcal{K}_m\rangle_V$ and the third group has the highest values and the strongest fluctuations of $\langle\mathcal{K}_m\rangle_V$. Experiment 6 is unique in that it yields substantially increased values of $\langle\mathcal{K}_m\rangle_V$ that are clearly correlated with individual breaking events ($-\bullet-$ and vertical dashed line in figure 4.4.4b). The temporal structure of $\langle\mathcal{K}_m\rangle_V$ indicates that episodic increases of the bulk diffusivity parameter are not directly correlated with the bulk-averaged turbulence intensity.

Figure 4.4.4(c) shows the volumetric and temporal averages, $\langle\cdot\rangle_{V,T}$, of $\mathcal{I}_m$ and $\mathcal{K}_m$. Red symbols correspond to $\langle\mathcal{K}_m\rangle_{V,T}$ against $\langle\mathcal{I}_m\rangle_{V,T}$ while the clusters of symbols around each red symbol correspond to $\langle\mathcal{K}_m\rangle_V(t)$ against $\langle\mathcal{I}_m\rangle_V(t)$ (data shown in figures 4.4.4a,b). Further, the standard deviations (s.d.) of the bulk values $\langle\cdot\rangle_V$ over time are shown (bars in the red symbols). We only see significant temporal variability in experiment 6, shown by $-\bullet-$ in figure 4.4.4(b) and the cluster of circles in figure 4.4.4(c). The large deviations seen in experiment 6 are a consequence of having approximately steady values of turbulence intensity (see figure 4.4.4a) but with very episodic elevated mixing (see figure 4.4.4b), suggesting that an instantaneous and local sampling of dissipation can be very misleading in terms of predicting the instantaneous mixing rate. On the other hand, averaging over all the events we identify a simple relation between $\langle\mathcal{K}_m\rangle_{V,T}$ and $\langle\mathcal{I}_m\rangle_{V,T}$. For values of $\mathcal{O}\left(10^{-2}\right) \leq \langle\mathcal{I}_m\rangle_{V,T} \leq \mathcal{O}\left(10^{-1}\right)$ we find that $\langle\mathcal{K}_m\rangle_{V,T} \sim \mathcal{O}\left(10^{0}\right)$, *i.e.* that the total diffusivity is not substantially elevated over that expected by laminar diffusion. For $\mathcal{O}\left(10^{-1}\right) \leq \langle\mathcal{I}_m\rangle_{V,T} \leq \mathcal{O}\left(10^{1}\right)$, however, the observed diffusivity is greater than that expected in a laminar flow and increases approximately linearly with turbulence intensity. The data fit a power law $\langle\mathcal{K}_m\rangle_{V,T} \sim a\left\{\langle\mathcal{I}_m\rangle_{V,T}\right\}^b$, with parameters $a = 12.2$ and $b = 1.1$. In the next subsection we describe the Kelvin wave evolution in the near-shore region and analyse the vertical distribution of $\mathcal{I}_m$ during the events e_2 and e_3.

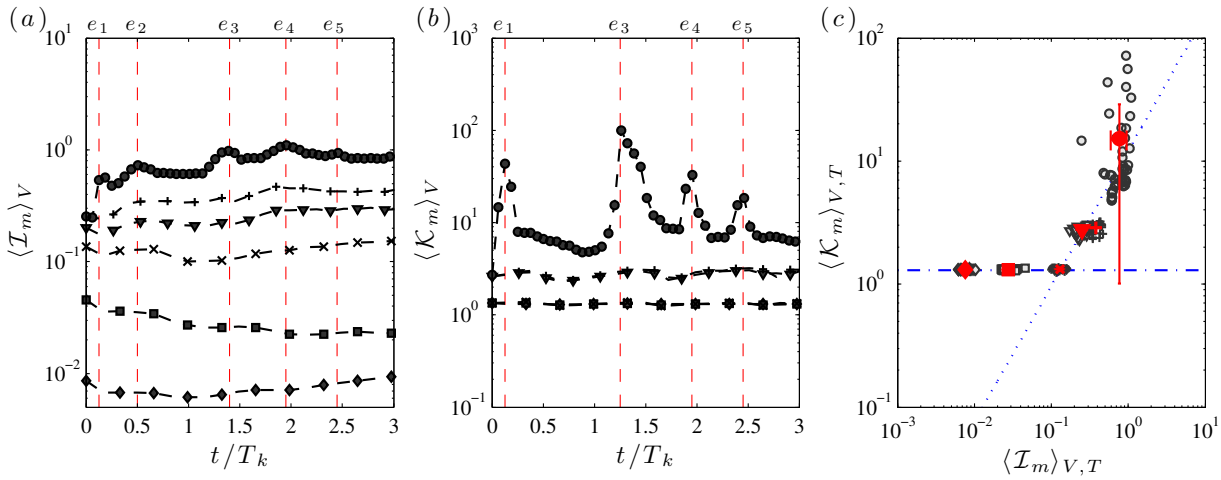

Figure 4.4.4: Evolution in time (scaled by T_K) of (a) the bulk turbulence intensity parameter, $\langle \mathcal{I}_m \rangle_V$, and (b) the bulk diffusivity parameter, $\langle \mathcal{K}_m \rangle_V$. Panel (c) exhibits $\langle \mathcal{K}_m \rangle_{V,T}$ versus $\langle \mathcal{I}_m \rangle_{V,T}$. Legend: Exp. 6: $-\bullet-$; Exp. 5: $-+-$; Exp. 4: $-\blacktriangledown-$; Exp. 3: $-\times-$; Exp. 2: $-\blacksquare-$; Exp. 1: $-\blacklozenge-$.

4.4.3 Flow evolution in the near-shore region

Figure 4.4.5 shows a summary of the vertical stratification in experiment 6, $\mathcal{N}^2/\mathcal{N}_0^2$ (where $\mathcal{N}_0^2 \equiv \max\{\mathcal{N}^2(t=0)\}$), in the area $\mathcal{A}_\theta$ defined by $z/H \in [0,1]$, $\theta \in [0, 2\pi]$ and $r/R = 0.98$, for 12 different times $t/T_k \in [0,3]$. The region $\mathcal{A}_\theta$ allows us to observe the IKW evolution near the boundary where the wave displacements are maximal and where the maximal values of the turbulent activity are observed (see figure 4.4.1). Figure 4.4.5(b) shows KH-type instabilities in the early stages of the experiment ($t/T_k \approx 0.128$) because of the strong initial shear near the crest of the IKW. Figure 4.4.5(c) shows the collapse or breakdown of the shear instabilities at $t/T_k \approx 0.25$. This process induces the formation of a turbulent patch and a local thickening of the density interface region that propagates along the shore region (see figure 4.4.5d and 4.4.1c). Simultaneously, the IKW has begun to steepen and form a solitary wave train (see figure 4.4.5d $- f$). After the first period, the leading wave of the solitary wave train interacts with the pre-existing stirred region (see figure 4.4.5g). The interaction generates interfacial breaking near the trough of the leading wave and a turbulent patch that subsequently spreads along the shore, over the solitary wave train (see figure 4.4.5g, h). This sequence of events is also observed after the second period (see figure 4.4.5(j)), where interfacial instabilities on the trough and tail of the leading wave can be seen. After $t/T_k \approx 3$, the initial IKW has evolved into a solitary wave train that covers the area $\mathcal{A}_\theta$ and a significant thickening and weakening of the density interface as a consequence of vertical mixing is observed (see figures 4.4.5(k, l)).

Turbulent patch and detrainment of vortices:

Figure 4.4.6 shows the turbulence intensity parameter, $\mathcal{I}_m$, and the radial vorticity scaled by the initial maximum buoyancy frequency, $(\vec{\omega} \cdot \hat{r}/\,|\mathcal{N}_0|)$, in the region $\mathcal{A}_\theta$, within the window time $t/T_k \in [0.25, 0.75]$. During this time the first two peaks of $\langle \mathcal{I}_m \rangle_V$ are registered (see figure 4.4.3a, $\mathrm{e}_1 - \mathrm{e}_2$). Figure 4.4.6($a$) shows the turbulent activity during the breakdown of KH-type billows around $t/T_k \approx 0.25$. The maximum magnitudes of $\mathcal{I}_m$ ($\sim 10^1 - 10^2$) are identified in the density interface and the upper layer, near the crest and over the wavefront. We identify high-intensity spots of $\mathcal{I}_m$ (in red) that

are ejected from the interfacial turbulent patch towards the top layer (blue arrow in figure 4.4.6a). Figure 4.4.6(b, d, f, h) illustrates the evolution (red arrows) of two red spots with $10^2 \leq \mathcal{I}_m \leq 10^3$. The

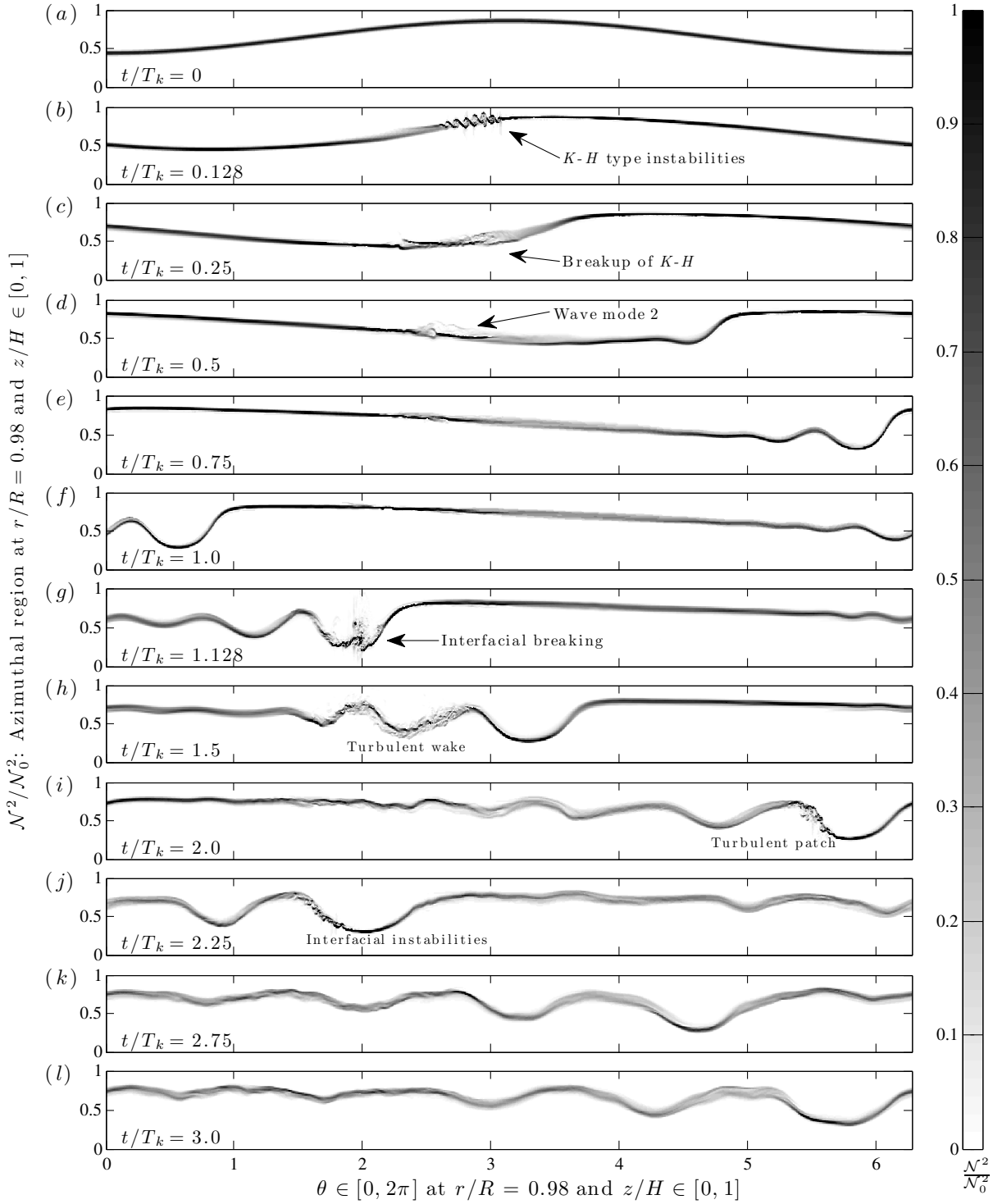

Figure 4.4.5: Results of experiment 6: evolution in time $t/T_k \in [0, 3]$ of the stratification, $\mathcal{N}^2/\mathcal{N}_0^2$, in the area $\theta \in [0, 2\pi]$, $z/H \in [0, 1]$ at $r/R = 0.98$.

radial vorticity field (see figure 4.4.6$c, \mathrm{e}, g, \mathrm{i}$) shows that these spots correspond to a coherent pair of counter-rotating vortices escaping from the interface region (see blue arrow in figure 4.4.6(c)) by their mutual interaction, carrying small scale turbulent fluid within their circulating cores into the ambient, non-turbulent water, thus enhancing the turbulent activity in the top layer (see figures 4.4.6j, l, n, p and 4.4.6k, m, o, q). This process is correlated with a local peak of the bulk turbulence intensity (event e_2 in figure 4.4.4a), but not with a local peak of the effective diffusivity parameter (see figure 4.4.4b). In this event, most of the higher spots of turbulence intensity are located near the top boundary, not in the the mixing interface; therefore we expect a weaker response of the effective diffusivity parameter.

Interfacial breaking and turbulent wake:

Figure 4.4.7 shows the density field and the turbulence intensity during the highest peaks of the turbulence activity parameters observed in experiment 6 (see event e_3 in figure 4.4.4a, b). During this time interval the solitary-type waves encounter and interact with the pre-existing turbulent patch shown in figure 4.4.6. The leading solitary-type wave induces a compression of the isopycnals in the density interface, increasing the buoyancy effects in the wavefront $\mathcal{N}^2 \sim |\partial_z \rho|$, but also enhancing the shear and the turbulent activity, $\varepsilon_m \sim |\partial_z^m U|^2$, on the flat density region, upstream of the leading wave, from where interfacial instabilities start to re-emerge (see figure 4.4.7a, b). As the leading solitary wave crosses the sheared region, cores of interfacial fluid are ejected and transported through the top layer flow (see figure 4.4.7c, d). These processes induce local convection, which in turn enhances the turbulent activity on the internal face of the leading wave. Figure 4.4.7(e, f) shows a strong interfacial breaking on the trough of the leading wave. The interaction between this new source of turbulence and the solitary wave train induces an interfacial turbulent wake that is spread over the wave train. The turbulent wake is characterized by the growth and collapse of Kelvin-Helmholtz-type billows that lead to local unstable density conditions, which in turn trigger baroclinic-type instabilities by free convection (Matsumoto & Hoshino, 2004; van Haren, 2015) (see figure 4.4.7$g - l$). The wave breaking process and the subsequent turbulent wake is schematized in figure 4.4.8; similar schematics have been previously introduced by Moum *et al.* (2003) and Carr *et al.* (2008). The results suggest that the coupling of shear and convective flows plays an important role in the emergence of interfacial instabilities and breaking in steepened wavefronts (Preusse *et al.*, 2012b,a).

4.5 Summary and discussion

Direct numerical simulations of the Boussinesq equations with a hyper-viscosity/diffusivity (H-VD) approach have been conducted to examine the transition from a laminar to a turbulent regime in a flow induced by the gravest internal Kelvin wave (IKW) in a continuous two-layer cylindrical domain at laboratory scale.

A range of values of the steepening parameter $\mathcal{T}_{sk}$, the damping parameter $\mathcal{T}_{\nu k}$ and the Richardson number $\mathcal{J}$, all related to the initial wave amplitude η_0, have been explored for a single Burger number $\mathcal{B}_\mathrm{i} = 0.25$. Under this rotating regime, the IKW structure is strongly confined to the shore (Stocker & Imberger, 2003). The results show the existence of four dynamic regimes and two regimes of turbulent activity.

The first three dynamic regimes have been analysed in previous numerical studies (de la Fuente *et al.*,

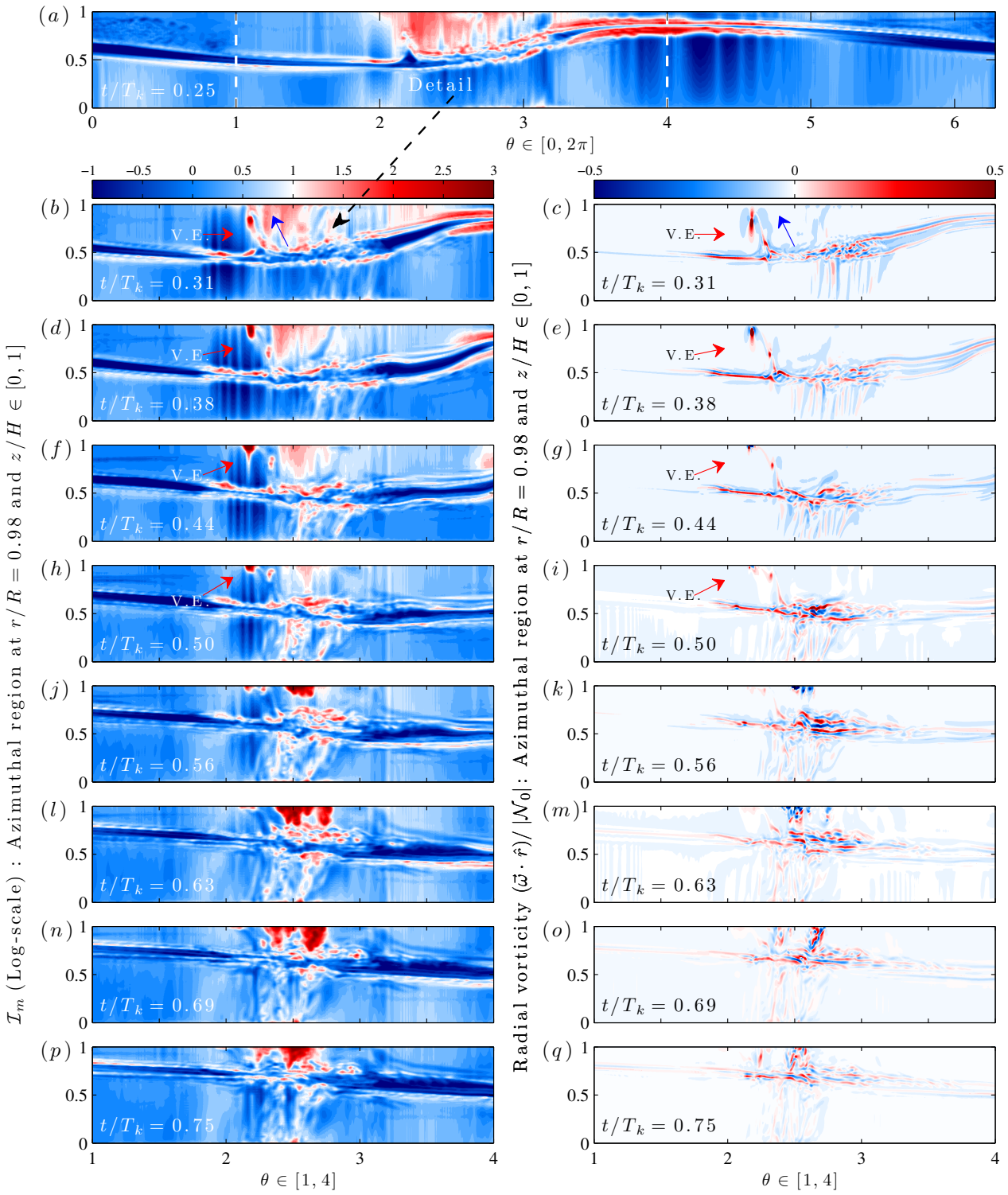

Figure 4.4.6: Results of experiment 6: evolution in time $t/T_k \in [0.25, 0.75]$ of the turbulence intensity parameter (in log-scale) and radial vorticity in the region $\theta \in [0, \pi]$, $z/H \in [0, 1]$ at $r/R = 0.98$, during the peak of $\langle \mathcal{I}_m \rangle_V$, denoted with the symbol e_2 in figures 4.4.1(d), 4.4.3 and 4.4.4. VE, vortex ejection.

2008; Sakai & Redekopp, 2010), here called damped linear (DLR), nonlinear (NLR) and non-hydrostatic

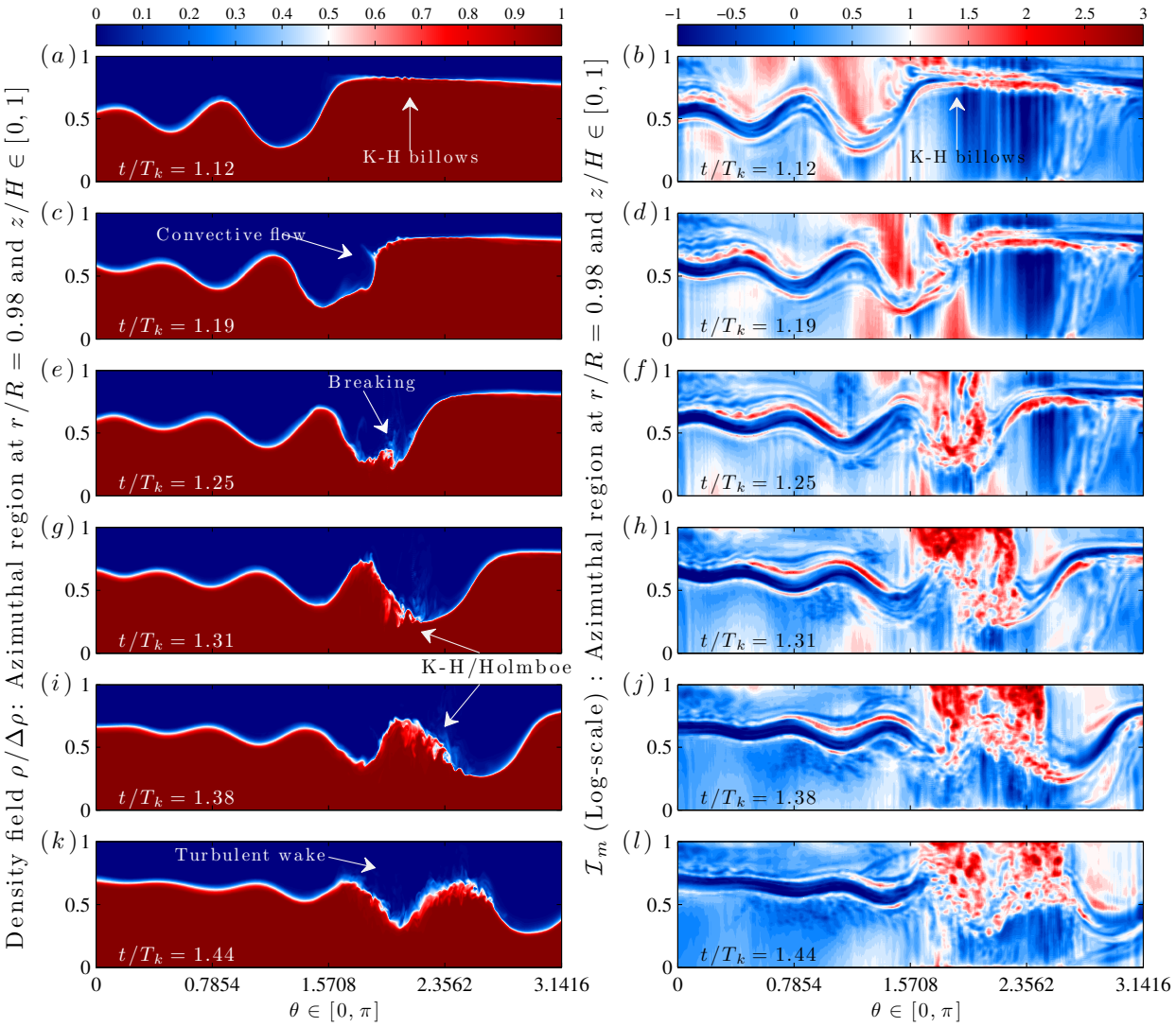

Figure 4.4.7: Results of experiment 6: evolution in time $t/T_k \in [1.12, 1.44]$ of the density field and turbulence intensity parameter during the breaking wave process in the region $\theta \in [0, \pi]$, $z/H \in [0, 1]$ at $r/R = 0.98$.

(NHR) regimes. These three regimes can also be identified in laboratory experiments conducted by Ulloa *et al.* (2014), which studied the evolution of internal wave fields composed by rotating, basin-scale internal gravity waves. In particular, for similar dimensionless numbers, numerical and experimental results show clear similarity (e.g., compare figure 5*a* in Ulloa *et al.* (2014) with figure 4.2.1*k* of this paper). However, despite the similarities, our numerical results cannot be directly contrasted with those laboratory results because they substantially differ in the initial and boundary conditions. In the laboratory experiments the flow was induced by linear tilting of the density interface, and energy damping was governed by wall-friction. Here we present a fourth regime called the laminar-turbulent transition regime (TR). The TR is characterized by the growth of interfacial instabilities and the formation of turbulent patches as a consequence of the IKW degeneration. Observation of the TR motivates the analysis of the turbulent activity involved in the IKW evolution.

The first regime of the turbulent activity is related to the linear and weakly nonlinear dynamics of the IKW. Increasing η_0 to transition from the LR to the weakly nonlinear NHR produces only a

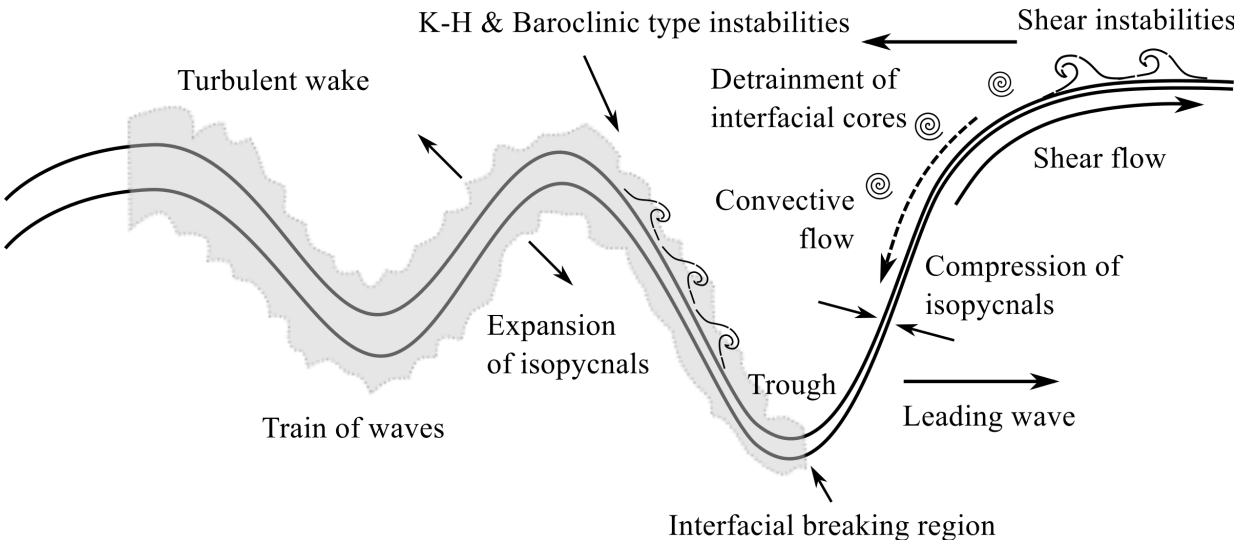

Figure 4.4.8: Schematic of the breaking wave process.

Exp.	$\mathcal{T}_{\nu k}/\mathcal{T}_{sk}$	$\min_{z\sim z_i}\{\mathcal{J}\}$	DLR	NLR	NHR	TR	$I.I.^{(1)}$	$I.B.^{(2)}$	$\langle\mathcal{I}_m\rangle_V$	$\langle\mathcal{K}_m\rangle_V$
1	3×10^{-3}	31.86	✓	×	×	×	0	0	$\mathcal{O}\left(10^{-3}-10^{-2}\right)$	$\mathcal{O}\left(10^{0}\right)$
2	2×10^{0}	3.04	✓	✓	×	×	0	0	$\mathcal{O}\left(10^{-2}-10^{-1}\right)$	$\mathcal{O}\left(10^{0}\right)$
3	4×10^{2}	0.58	✓	✓	✓	×	0	0	$\mathcal{O}\left(10^{-1}\right)$	$\mathcal{O}\left(10^{0}\right)$
4	2×10^{3}	0.30	✓	✓	✓	×	0	0	$\mathcal{O}\left(10^{-1}-10^{0}\right)$	$\mathcal{O}\left(10^{0}-10^{1}\right)$
5	5×10^{3}	0.19	✓	✓	✓	✓	2	0	$\mathcal{O}\left(10^{-1}-10^{0}\right)$	$\mathcal{O}\left(10^{0}-10^{1}\right)$
6	10^{4}	0.13	✓	✓	✓	✓	4	1	$\mathcal{O}\left(10^{0}-10^{1}\right)$	$\mathcal{O}\left(10^{1}-10^{2}\right)$

Table 4.3: Regimes observed in the IKW evolution. (1): Number of interfacial instabilities observed, (2): Number of interfacial breaking observed.

moderate increase of the low values of the bulk turbulence intensity parameter $\langle\mathcal{I}_m\rangle_V$. It does not, however, significantly increase the overall rate of fluid mixing measured by the bulk effective diffusivity parameter $\langle\mathcal{K}_m\rangle_V$ (see the results of experiments 1-3 in figure 4.4.4). In this regime the sheared flow induced by the IKW and its weakly nonlinear degeneration is fully suppressed by the buoyancy, thus avoiding the transition from laminar to turbulent flow. The second regime of turbulent activity is related to the strong nonlinear dynamics of the IKW. The results show a substantial increase in turbulent activity as the flow evolves from the strong NHR to the TR (see the results of experiments 4-6 in figure 4.4.4). The strong degeneration of the IKW and the intensification of the shear flow in the wavefront of the leading wave destroy locally and intermittently the interface stability within the Rossby radius from the boundary, triggering the formation of intermittent turbulent patches from the growth and breakdown of Kelvin-Helmholtz-type billows. On the other hand, buoyancy imposes stability in the interior regions, though the turbulent activity there tends to increase as a consequence of the inertial gravity wave radiation from the near-shore to the offshore region (see figures 4.3.2-4.4.1). In this second regime, the nonlinear degeneration of the IKW and the turbulent episodes observed in experiments 4-6 are directly correlated with increases in the turbulence activity parameter, showing a power dependence between $\langle\mathcal{I}_m\rangle_V$ and $\langle\mathcal{K}_m\rangle_V$ (see figure 4.4.4(c)). Table 4.3 summarizes the IKW regimes.

We have identified four sources of turbulence in the TR: (i) interfacial instabilities driven by shear

flows, (ii) the transport of vorticity from the interfacial region to well-mixed layers driven by the mutual interaction of vortex pairs (with opposite sign), (iii) interfacial breakings, associated with the interaction of convective and shear flows over steep solitary-type waves and (iv) baroclinic-type instabilities presumably supported by the combination of vortex-type motions and shear flow in the near-shore region. The analysis of the emergence of interfacial instabilities in internal solitary waves (ISWs) has been addressed mainly via numerical study in a two-layer fluid, in a two-dimensional channel (Barad & Fringer, 2010; Carr *et al.*, 2011; Almgren *et al.*, 2012; Preusse *et al.*, 2012a). The numerical experiments of Carr *et al.* (2011) and Almgren *et al.* (2012) have shown that the growth of Kelvin-Helmholtz-type billows near the trough and tail of ISW amplitude (compare figures 7 and 8 by Carr *et al.* (2011) and Almgren *et al.* (2012), respectively, with our figure 4.4.5i, j) is close to the thickness of the top layer, $\eta_0/h_1 \approx 1$. In addition, the propagation of shear instabilities can disturb the tail and interact with a solitary wave train, giving rise to a turbulent wake in the density interface region, as shown by Barad & Fringer (2010) (see their figures 3 and 4 and our figures 4.4.5h and 4.4.7g, i, k). Parts of these previous results have been supported by laboratory experiments (Grue *et al.*, 1999, 2000). Moreover, recent laboratory results have shown that convective instabilities in ISWs due to small-scale overturns may aid shear-induced instabilities on the wavefront (Carr *et al.*, 2008; Fructus *et al.*, 2009), giving feedback to the unstable state of the flow and enhancing the turbulence and mixing in the wave vicinity. In this context, our numerical study extends the analysis to nonlinear internal waves in enclosed rotating water bodies, such as medium or large lakes.

Field studies in stratified medium or large lakes have identified important sources of turbulence in the density interface attributed to shear instabilities (Kelvin-Helmholtz-type billows) riding over the slope of IKWs (Lorke, 2007; Preusse *et al.*, 2010). Furthermore, density inversion and interfacial breakings at the trough of a solitary wave train of large amplitudes have also been associated with the nonlinear degeneration of basin-scale IKWs (Preusse *et al.*, 2010, 2012b,a). Both nonlinear processes have been observed in the TR of experiment 6. However, the interaction between interfacial turbulent patches and steep internal waves has not been studied and detected in detail in stratified lakes. This process can be a periodic source of turbulence and mixing in stratified lakes. In addition, the results suggest that the turbulence intensity is linked to the internal Rossby radius, and its horizontal distribution could be driven by the behaviour of the vertical vorticity (mainly observed in the near-shore region) and radial vorticity (mainly generated in the density interface region by shear flow), both processes as a consequence of the evolution and degeneration of the IKW.

The classification of the 'dynamic regimes' can be adopted for further use, nut it is important to note that the regimes were established for a particular configuration of stratification ($h_1/H = 0.35$) and rotation ($B_\mathrm{i} = 0.25$) and, indeed, the conditions to achieve them (LR, NL, NHR, TR) can change in terms of h_1/H and B_i (see e.g., Horn *et al.*, 2001; Boegman *et al.*, 2005b; Ulloa *et al.*, 2014).

To analyse the effect of rotation in the spatial distribution of turbulence as a consequence of the IKW degeneration, further studies are required. However, if the rotating regime changes (e.g., due to seasonal variations), for example to higher Burger numbers (larger R_i), the radial velocity component plays a more active role in the IKW propagation and the IKW can store more available potential energy within R_i. Therefore, variations in the rotating regime could change both the thresholds of dynamics regimes and the spatial distribution of turbulence induced by the IKW evolution.

As in Thomson (1880) and Csanady (1967), our study adopts the simplest representation possible for a rotating, stratified lake: a cylindrical basin with uniform depth. Moreover, to highlight the processes that promote wave steepening, degeneration and instability, we have excluded the effects of

bottom friction. Real lakes, of course, have irregular shapes, frictional bottom boundary layers and shoaling bathymetry. How these features influence and modify the wave dynamics discussed here are important practical issues (see e.g., Beletsky *et al.*, 1997; Boegman *et al.*, 2003; Sakai & Redekopp, 2010) that warrant further work.

Acknowledgements

The authors acknowledge support from the Civil Engineering Department, Universidad de Chile, and the Scripps Institution of Oceanography at the University of California San Diego. This work was supported by the U.S. National Science Foundation (grant number OCE-1155121) and XSEDE computing resources (grant TG-OCE 120004). Powered@NLHPC: This research was partially supported by the supercomputing infrastructure of the NLHPC (ECM-02), Center for Mathematical Modeling, Universidad de Chile. We thank Roy Barkan, Hieu Pham, Oscar Sepulveda and the four anonymous referees for helpful discussions and suggestions. KBW acknowledges support from a Fulbright Fellowship. The first author acknowledges financial support from the CONICYT doctoral fellowship 21110069 and the Postgraduate Department Scholarship, Universidad de Chile (Research Internship Abroad, 2012).

4.6 Appendix A. Derivation of the turbulence activity parameter

We can derive the equation of the kinetic energy budget by taking the scalar product of the velocity field $\vec{v}$ with the momentum equation (see 4.2.1). Then

$$\partial_t \mathscr{E}_k + (\vec{v}\cdot\nabla)\,\mathscr{E}_k = -\frac{\vec{v}}{\rho_0}\left(\nabla p + \rho g\hat{k}\right) + \nu_m \vec{v}\cdot\nabla^{2m}(\vec{v})\,, \tag{A.1}$$

where $\mathscr{E}_k \equiv (\vec{v}\cdot\vec{v})/2$ is the kinetic energy per mass unit. Rearranging terms, the local time rate of change of kinetic energy can be expressed as follows:

$$\partial_t \mathscr{E}_k = -\nabla\cdot\left\{\vec{v}\left(\mathscr{E}_k + \frac{p}{\rho_0}\right) - \nu_m\nabla^{h-1}(\vec{v}\cdot\nabla^m\vec{v})\right\} - \frac{\rho}{\rho_0}gw - \nu_m\left|\nabla^m\vec{v}\right|^2. \tag{A.2}$$

The first term of the right-hand side of equation (A.2) gives the rate change of the kinetic energy resulting from advection, pressure and hyper-viscous diffusion of energy, the second term gives the reversible rate of exchange with potential energy due to buoyancy flux, while the third term gives the irreversible rate of hyper-viscous kinetic energy dissipation. Averaging equation (A.2) over a closed volume V, we obtain the following kinetic energy budget:

$$\partial_t\langle\mathscr{E}_k\rangle_V = -\frac{1}{V}\int_V\left\{gw\frac{\rho}{\rho_0}\right\}\mathrm{d}V - \frac{1}{V}\int_V\left\{\nu_m\left|\nabla^m\vec{v}\right|^2\right\}\mathrm{d}V. \tag{A.3}$$

We are interested in the second term of equation (A.3):

$$\varepsilon_m = \nu_m\left|\nabla^m\vec{v}\right|^2. \tag{A.4}$$

From ε_m and ν_m, the hyper-viscous Kolmogorov length scale can be calculated using the same arguments that set the ordinary ($m = 1$) Kolmogorov scale, resulting in

$$\ell_K \equiv \left\{ \frac{\nu_m^3}{\varepsilon_m} \right\}^{1/(6m-2)} . \tag{A.5}$$

This scale defines where viscous forces balance inertial forces and the cascade is ultimately dissipated. The activity parameter is fundamentally the ratio of the Ozmodiv scale and the Kolmogorov scale. The Ozmidov scale depends on the kinetic energy dissipation and the buoyancy frequency, and it is defined as follows:

$$\ell_O \equiv \left\{ \frac{\varepsilon_m}{\mathcal{N}^3} \right\}^{1/2} . \tag{A.6}$$

This is the buoyancy scale at which the buoyant forces balance the inertial forces. A turbulence activity parameter will be a ratio, to some power (p) for convenience, of these two scales, i.e., a measure of how much bandwidth there is in the flow between the Ozmidov scale and the Kolmogorov scale (Barry *et al.*, 2001):

$$\mathcal{I}_{m,p} \equiv \left\{ \frac{\ell_O}{\ell_K} \right\}^p = \left\{ \frac{\varepsilon_m}{\nu_m^3} \right\}^{p/(6m-2)} \cdot \left\{ \frac{\varepsilon_m}{\mathcal{N}^3} \right\}^{p/2} . \tag{A.7}$$

In the viscous case ($m = 1$), the turbulence activity parameter has been defined using $p = 4/3$. Thus

$$\mathcal{I}_m \equiv \left\{ \frac{\ell_O}{\ell_K} \right\}^{4/3} = \frac{\varepsilon}{\mathcal{N}^2 \nu}. \tag{A.8}$$

If we keep the power $p = 4/3$ for the hyper-viscous version of the turbulence intensity parameter we obtain the following expression:

$$\mathcal{I}_m \equiv \frac{1}{\mathcal{N}^2} \left\{ \frac{(\varepsilon_m)^m}{\nu_m} \right\}^{2/(3m-1)} . \tag{A.9}$$

4.7 Appendix B. Derivation of the diffusivity parameter

We are interested in estimating how the mass diffusivity changes as a consequence of the evolution of an IKW in a two-layer flow. For this we will study the scales associated with the fluid mixing due to the flow and molecular action. We can analyse the fluid mixing via the time rate of change of the background potential energy per mass unit, $\mathscr{E}_b = \rho g z_* / \rho_0$:

$$\partial_t \mathscr{E}_b = \frac{g}{\rho_0} \partial_t \left\{ z_*(\vec{x}, t) \rho(\vec{x}, t) \right\} = \frac{g}{\rho_0} \left\{ z_* \partial_t \rho + \rho \partial_t z_* \right\}, \tag{B.1}$$

where z_* is the reference height in the minimum potential energy state of a fluid parcel at position $(\vec{x}, t)$ (Winters *et al.*, 1995; Winters & D'Asaro, 1996). From the mass transport equation (see 4.2.1), we can obtain the term $\partial_t \rho$ and replace it in equation (B.1), yielding

$$\partial_t \mathscr{E}_b = -\frac{g}{\rho_0} z_* \left\{ \nabla \left(\vec{v} \rho \right) - \kappa_m \nabla^{2m} \rho \right\} + \frac{g \rho}{\rho_0} \partial_t z_* . \tag{B.2}$$

Because the z_* vertical coordinate depends implicitly on the density distribution $\rho(\vec{x}, t)$, we can write

$$z_* \nabla \rho = \nabla \xi \quad \text{where} \quad \xi = \int^{\rho} z_* \left(\hat{\rho}\right) \mathrm{d}\hat{\rho}, \tag{B.3}$$

noting that $\nabla z_* = (\mathrm{d}z_*/\mathrm{d}\rho)\nabla\rho$. Using equation (B.3) and rearranging terms, the background potential energy budget can be written as follows:

$$\partial_t \mathscr{E}_b = -\frac{g}{\rho_0} \nabla \left\{ \vec{v}\xi - \kappa_m \nabla \left(z_* \nabla^{2m-1} \rho \right) \right\} - \frac{g}{\rho_0} \kappa_m \left(\frac{\mathrm{d}\rho}{\mathrm{d}z_*} \right)^{-1} |\nabla^m \rho|^2 + \frac{g\rho}{\rho_0} \frac{\partial z_*}{\partial t}. \tag{B.4}$$

Averaging $\partial_t \mathscr{E}_b$ over a closed volume V, the first and the third terms of the right-hand side of equation (B.4) are zero due to the no-flux boundary conditions and the mathematical construction of z_*, respectively (Winters *et al.*, 1995), respectively. Hence, the background potential energy budget in a closed domain is reduced to the following expression:

$$\partial_t \langle \mathscr{E}_b \rangle_V = \frac{1}{V} \int_V - \left\{ \frac{g}{\rho_0} \kappa_m \left(\frac{\mathrm{d}\rho}{\mathrm{d}z_*} \right)^{-1} |\nabla^m \rho|^2 \right\} \mathrm{d}V. \tag{B.5}$$

Notice that the background density gradient, $\mathrm{d}\rho/\mathrm{d}z_*$, is a negative or null quantity, therefore $-\mathrm{d}\rho/\mathrm{d}z_*$ is a null or positive quantity, and therefore $\partial_t \langle \mathscr{E}_b \rangle_V$ is always positive. The expression integrated in the equation (B.5) corresponds to the diapycnal flux given our m operators, $\phi_{h\mathrm{d}}$, which can be expressed in terms of the 'buoyancy', b, writing the density as $\rho = \rho_0(1 - g^{-1}b)$:

$$\phi_{h\mathrm{d}} = \kappa_m \frac{|\nabla^m b|^2}{\mathrm{d}b/\mathrm{d}z_*}. \tag{B.6}$$

When the flow is turbulent, the buoyancy field is stirred and filamented and the numerator greatly exceeds the denominator. If we move to the laminar limit and imagine that the fluid is not at all stirred or filamented, but rather exists in its minimum potential energy state, then we can define a reference laminar diffusive flux for comparison. We call this flux ϕ_*, where

$$\phi_* = \kappa_m \frac{|\mathrm{d}^m b/\mathrm{d}z_*^m|^2}{\mathrm{d}b/\mathrm{d}z_*}. \tag{B.7}$$

We can now define an 'enhancement' parameter, measuring the increase in diffusive flux due to turbulent stirring and straining relative to the laminar, diffusive flux in a fluid with the same background buoyancy profile that is not stirred or strained:

$$\mathcal{K}_m \equiv \frac{\phi_{h\mathrm{d}}}{\phi_*} = \frac{|\nabla^m b|^2}{\left| \frac{\mathrm{d}^m b}{\mathrm{d}z_*^m} \right|^2}. \tag{B.8}$$

Note that this reduces to the Cox number when $m = 1$ and always represents a ratio of turbulent diffusive flux to laminar diffusive flux for the same collection of fluid parcels, i.e. for a fluid with the same sorted state of buoyancy profile state.

Chapter 5

Concluding remarks

In this thesis we investigated the degeneration of basin-scale internal gravity waves in an idealized two-layer stratified rotating basin via numerical and laboratory experiments. The dynamics of the basin-scale internal gravity waves was controlled by four main parameters: (i) a first parameter associated to the relevance of rotation in the wave dynamics; (ii) a second parameter associated to the relative phase velocities across the domain, which can admit internal waves, and thus lead to steepening when the wave amplitude is not neglected; (iii) a third parameter associated to the relevance of viscosity, which can control the wave damping; and (iv) a fourth parameter associated to the local hydrodynamic stability of stratified shear flows. The basin-scale internal gravity waves were energized by initial displacements of the density interface under different background environments (rotation and stratification structure).

The free evolution of basin-scale gravity waves in a two-layer stratified rotating cylindrical basin was analysed via laboratory experiments conducted in cylindrical tank on a rotating table. Although most of the experiments were developed under nonlinear wave regimes, the linear theory predicted with good agreement the frequency structure of the basin-scale internal gravity wave field. In addition, the laboratory experiments showed similar results to those predicted by numerical experiments performed by de la Fuente *et al.* (2008) and Sakai & Redekopp (2010), in weakly nonlinear and non-hydrostatic regimes. In this context, both numerical and laboratory results have shown the nonlinear degeneration of the basin-scale internal wave and the formation of a train of solitary type waves, as a consequence of steepening and non-hydrostatic wave dispersion, which propagate along the shoreline. Moreover, the results suggested a nonlinear interaction between Kelvin and Poincaré waves, which could lead to pseudo-resonant states and the transfer of energy from lower modes to higher modes. The nonlinear dynamic of basin-scale internal gravity waves showed a relevant dependence between the wave amplitude and the stratification structure, in agreement with the theory of nonlinear wave dynamics. However, additionally, we identified that rotation also play a role in the degeneration of basin-scale internal waves. In fact, the laboratory results showed that the scales of the solitary type waves driven by the degeneration of the IKW had better agreement with KdV type models when the background rotations were more important or stronger. The results showed that the intensity of the nonlinear dynamics affected the decay rate of the internal gravity wave field and, particularly, the decay rate of the IKW, which showed a strong sensibility at the background stratification/rotation conditions. The main decay mechanisms identified were the Ekman layers damping, the nonlinear disintegration via steepening and non-hydrostatic process, and the consequently transfer of energy from the IKW to sub-modes. Although the characterization and quantification of the decay time scale of the IKW is important, it is essential to understand how the basin-scale motions lose energy. This quantity does not give information about where, how and how much energy dissipation occurs in the flow, in terms of the internal wave field dynamics at laboratory scale. The quantification of the spatiotemporal energy dissipation and mixing processes continues to be a challenge in this type of laboratory experiments.

The numerical experiments were performed using spectral based direct numerical simulations with an hyper-viscosity/diffusivity approach, which assumes a downscale energy cascade with the rate of energy transfer controlled by the nearly inviscid processes in the inertial subrange. This approach allows the inertial subrange to be as broad as possible for a given grid resolution, which is convenient when no extensive computational resources are available. In addition, the employed numerical method

required suitable initial conditions characterized by smooth fields. Therefore, the classic normal mode solutions obtained from discontinuous two-layer stratifications were not suitable (Csanady, 1967), but neither the normal mode solutions obtained from continuously stratified systems (Kundu *et al.*, 2012, See Chapter 13, sub-section 13.9). The analytical construction of smooth linear normal modes proposed in Chapter 2 solved the discontinuity problem of the layered solutions through the use of a Laplacian diffusion on the density and momentum fields, over a finite time scale, in order to induce a smooth transition between the bottom and top layer. This approach allowed the energization of the wave through the increment of its amplitude, which leads to a direct increment of the vertical shear at the density interface region. The solutions proposed in Chapter 2 were derived from an inviscid fluid, hence, free-slip boundary conditions were adopted for the numerical experiments. This physical characteristic implies that the energy dissipation occurs only in the interior of the fluid, which is a clear difference and restriction of the conceptual model with respect to real scenarios. For the use of no-slip boundary conditions (which take into account the presence the viscous boundary layers), new or modified solutions are required.

Smooth linear normal modes, introduced in Chapter 2, were used to compute the free evolution of the gravest internal Kelvin waves (IKW) via direct numerical simulations of the Boussinesq equations with a hyper-viscosity/diffusivity approach. From the numerical experiments, we identified four dynamics regimes, here called damped linear (DLR), nonlinear (NLR), non-hydrostatic (NHR), and laminar-turbulent transition (TR). The three first regimes have been analysed in previous numerical studies (de la Fuente *et al.*, 2008; Sakai & Redekopp, 2010). We focused the analysis in the TR, which was characterized by the growth of interfacial instabilities and the formation of turbulent patches as a consequence of the IKW degeneration. To quantify the increment of the dissipation rates of kinetic energy and the buoyancy variance, we derived turbulence activity parameters for the hyper-viscosity/diffusivity approach. Both parameters are analogous to the turbulence intensity parameter (Barry *et al.*, 2001) and the Cox number (Winters & D'Asaro, 1996) for Newtonian fluids. From this analysis, two energetic regimes were found. The first energetic regime was linked to linear and weakly nonlinear dynamics of the IKW. In this regime, no important increments of the effective mass diffusivity in terms of increments of turbulence intensity were observed. The second energetic regime was linked to strong NHR to the TR. In this regime, the strong nonlinear degeneration of the IKW and the turbulent episodes were directly correlated with the increment of both turbulence activity parameters, showing a power dependence between the turbulent intensity and the effective mass diffusion. We highlight the spatial and temporal distribution of the turbulence activity. Most of the turbulent activity was observed within the internal Rossby radius of deformation, near the shore region, whereas the temporal structure showed periodic increments associated to the interaction of basin-scale internal waves with interfacial turbulent patches. These two regimes have been previously identified both in field and numerical stratified flows, but not specifically for stratified flows driven by IKW. Our numerical experiments achieved a limited range of values for the turbulence activity parameters, thus, in order to compare with previous observations (e.g., Shih *et al.*, 2005; Bouffard & Boegman, 2013), we require to extend the range of values of the turbulence activity parameters, which means further numerical experiments with higher numerical resolutions.

Appendices

Appendix A

Governing equations

In this appendix, the equation of motions of stratified fluids in rotating environments ('geopgysical flows') are stated from several conservation laws and the so-called Boussinesq approximation. This appendix has mostly based on Pedlosky (1987), Cushman-Roisin & Beckers (2011) and Kundu *et al.* (2012) as references.

A.1 Equations of fluid motion

In this section the mass, momentum and energy budgets for a newtonian fluid on a f–plane are stated.

A.1.1 Mass budget

The conservation of mass for a material volume $V(t)$ bounded by volume's surface $A(t)$ in a flowing fluid is a fundamental law in fluid mechanics. This statement takes the following form:

$$\frac{\mathrm{d}}{\mathrm{d}t}\int_{V(t)}\rho(\vec{x},t)\mathrm{d}V \equiv 0, \tag{A.1.1}$$

where ρ is the fluid density. Applying both the Reynolds transport theorem and the Gauss' divergence theorem the differential equation that represents mass budget is obtained:

$$\int_{V(t)}\left\{\frac{\partial\rho(\vec{x},t)}{\partial t}+\nabla\cdot(\rho(\vec{x},t)\vec{v}(\vec{x},t))\right\}\mathrm{d}V \equiv 0, \tag{A.1.2}$$

where $\vec{v}=(u,v,w)$ is the velocity field. The last equality is possible if the integrand is nulled at every point in space. Thus, (A.1.2) requires:

$$\frac{\partial\rho(\vec{x},t)}{\partial t}+\nabla\cdot\{\rho(\vec{x},t)\vec{v}(\vec{x},t)\}\equiv 0, \quad \text{or,} \quad \frac{1}{\rho(\vec{x},t)}\frac{D}{Dt}\rho(\vec{x},t)+\nabla\cdot\vec{v}(\vec{x},t)\equiv 0, \tag{A.1.3}$$

where $D/Dt=\partial/\partial t+(\vec{v}\cdot\nabla)$ is the material derivative. The relationship in (A.1.3) is called 'continuity equation'. $D\rho/Dt$ is the time rate of change of fluid density following a fluid particle. This rate is zero for constant density where ρ is constant throughout the flow field, and for incompressible flow where the density of fluid particles does not change but different fluid particles may have different density. Then, assuming $D\rho/Dt=0$, the continuity equation for incompressible flows is reduced to

$$\nabla\cdot\vec{v}(\vec{x},t)\equiv 0. \tag{A.1.4}$$

A.1.2 Momentum budget

The Newton's second law is the fundamental principle governing fluid momentum. This conservation law is better stated per unit volume with density replacing mass. For geophysical flows, or flows in rotating environments, the momentum equation is

$$\rho\left\{\frac{D\vec{v}}{Dt}+\left(f\hat{k}\times\vec{v}\right)\right\}\equiv-\nabla p-\rho g\hat{k}+\mu\Delta\vec{v}, \tag{A.1.5}$$

where f is the inertial frequency or the Coriolis parameter, p is the pressure field, g is the gravity acceleration, is the unit vertical vector (positive upward), Δ represents the Laplace operator acting on the momentum transport, with ν the dynamic viscosity coefficient. Notice that (A.1.5) is the standard Navier-Stokes equations in a rotating environment in which only the vertical component of angular velocity is important.

A.1.3 Equation of state

For an incompressible fluid, such as pure water at ordinary pressures and temperatures, density can be assumed constant. However, in environmental fluids, such as oceans and lakes, water density is a function of pressure, temperature and salinity, mainly. But for most applications in environmental waters, density variations as a consequence of pressure variations can be neglected. A simplified linear model has been used to describe the relationship between density, temperature and salinity for water:

$$\rho=\rho_0\left[1-\alpha\left(T-T_0\right)+\beta\left(S-S_0\right)\right], \tag{A.1.6}$$

where T is the temperature (in degrees Celsius or Kelvin), S is the salinity (in practical salinity units 'psu'). The constants ρ_0, T_0 and S_0 are reference values of density, temperature, and salinity, respectively. The terms α and β are called 'thermal expansion (in $[T]^{-1}$)' and 'saline contraction (in $[S]^{-1}$)' coefficients, respectively. We have added one equation, and by doing so, we have introduced additional variables, temperature and salinity.

A.1.4 Energy budget

The equation governing temperature arise from the principle of energy conservation, also known as the first law of thermodynamics, which states that internal energy gained by a parcel of matter is equal to the heat it receives minus the mechanical work it performs, i.e.,

$$\frac{D\mathrm{e}}{Dt}=Q-W \tag{A.1.7}$$

where e is the internal energy, Q is the rate of heat gain, and W is the rate of work done by the pressure force onto the surrounding fluid, all per unit mass. The internal energy is proportional to the temperature:

$$\mathrm{e}=C_vT, \tag{A.1.8}$$

where C_v is the hear capacity at constant volume, and T is the absolute temperature. The Q term includes only the heat gained by a parcel through its contact with its neighbors throughs the process

of diffusion. Using the Fourier law of heat conduction, Q can be written as follows:

$$Q = \frac{k_T}{\rho}\Delta T, \tag{A.1.9}$$

where k_T is the thermal conductivity of the fluid. The work done by the fluid is the pressure force multiplied by the displacement in the direction of the force. Hence, W can be written as follows:

$$W = -\frac{p}{\rho^2}\frac{D\rho}{Dt} \tag{A.1.10}$$

Using the second relation of the continuity equation (A.1.3), assuming an incompressible flow, $\nabla\cdot\vec{v} \equiv 0$, and replacing (A.1.8), (A.1.9) and (A.1.10) into (A.1.7) leads to:

$$\frac{DT}{Dt} = \frac{k_T}{\rho C_v}\Delta T. \tag{A.1.11}$$

This is the energy equation, which governs the evolution of temperature.

A.1.5 Salt budget

For seawater (or salty waters), density varies with the salinity as stated in (A.1.6). Its evolution is governed by the Fick's second law:

$$\frac{DS}{Dt} = \kappa_S \Delta S, \tag{A.1.12}$$

which is analogous to the energy equation. This equations states that a seawater parcel conserves its salt content, except for redistribution by diffusion. The term κ_S is the salt diffusion coefficient, which plays a role analogous to the hear diffusivity k_T.

In this context, the set of governing equations in now complete. There are seven variables $\{u, v, w, \rho, p, T, S\}$, for which we have seven governing equations: a continuity equation (A.1.4), three momentum equations (A.1.5), an equation of state (A.1.6), an energy equation (A.1.11) and a salt equation (A.1.12).

A.1.6 Boussinesq approximation

In most geophysical systems, the fluid density varies, but not greatly around a mean reference value, ρ_0. No losing generality, we can write the density field as following:

$$\rho = \rho_0 + \rho'(\vec{x}, t), \quad \text{with} \quad |\rho'| \ll \rho_0, \tag{A.1.13}$$

where the density perturbation ρ' caused by the existing stratification and/or fluid motions is small compared with the reference value ρ_0. Adopting this assumption, governing equations can be simplified.

First, substituting (A.1.13) into continuity equation (A.1.3):

$$\frac{1}{\rho_0 + \rho'}\left(\frac{\partial \rho'}{\partial t} + \vec{v}\cdot\nabla\rho'\right) + \nabla\cdot\vec{v} = 0 \tag{A.1.14}$$

Geophysical flows indicate that relative variations of density in time and space are usually much less

than the variations of the velocity field. Therefore, the first term (A.1.14) can be neglected and continuity equation is reduced to (A.1.4).

Second, we are going to substitute (A.1.13) into the momentum equations (A.1.5), but making the difference between horizontal components and the vertical component. The x- and y- (horizontal) momentum equations can be treated simultaneously. Wherever ρ' occurs, the dominant quantity of density will be ρ_0, therefore the density factor ρ in the left-hand front can be approximated by ρ_0. Dividing by $\rho 0$, the resultant horizontal momentum equations are the following:

$$\frac{Du}{Dt} - fv = -\frac{1}{\rho_0}\frac{\partial p}{\partial x} + \nu\Delta u, \tag{A.1.15a}$$

$$\frac{Dv}{Dt} + fu = -\frac{1}{\rho_0}\frac{\partial p}{\partial y} + \nu\Delta v, \tag{A.1.15b}$$

where $\nu = \mu/\rho_0$ is the kinematic viscosity coefficient. In the z- (vertical) momentum equations ρ appears as a factor not only in the left-hand front but also in the gravity force on the right-hand side. Operating analogously than the horizontal momentum simplifications, ρ' can be neglected from the factor ρ in the left-hand side, but on the right, it can not be done. Indeed, the term $\rho g\hat{k}$ considers the fluid weight, which causes the increment of pressure with depth in fluids columns. In hydrostatic balance, gravity force balances the vertical pressure gradient. If $\rho \approx \rho_0$, yiels

$$\frac{\mathrm{d}p_0}{\mathrm{d}z} = -\rho_0 g, \tag{A.1.16}$$

where p_0 is the pressure associated to the hydrostatic limit or 'hydrostatic pressure'. Thus, we can write the pressure field as the sum of a hydrostatic component, which is only z dependent, and a perturbation, which depends of time and space:

$$p = p_0(z) + p'(\vec{x}, t), \quad \text{with} \quad p_0(z) = P_0 - \rho g z, \tag{A.1.17}$$

so that the vertical momentum equations becomes

$$\frac{Dw}{Dt} = -\frac{1}{\rho_0}\frac{\partial p'}{\mathrm{d}z} - \frac{\rho'}{\rho_0}g + \nu\Delta w. \tag{A.1.18}$$

Note that the hydrostatic pressure $p_0(z)$ can be subtracted from p in the reduced horizontal momentum equations (A.1.15), because it has no derivatives with respect to x and y, an it is dynamically inactive.

For water, the energy equation can be subjected to the same approximation used in the momentum equations, $\rho \approx \rho_0$. This leads to the following equation:

$$\frac{DT}{Dt} = \kappa_T \Delta T, \tag{A.1.19}$$

where $\kappa_T = k_T/(\rho_0 C_v)$ is the heat kinematic diffusivity, which is analogous to the salt equation (A.1.12).

For sea water, the combination of equations (A.1.12) and (A.1.19) allows determining the evolution of density. However, in some water environments, the density is strongly dominated by only one of them, such as in lakes, in which the water density is strongly defined by the thermal structure, or estuaries with salty wedges, in which the water density is mainly defined by the salt distribution. In

these scenarios is possible to define a unique equation for the density evolution, combining (A.1.12) and (A.1.19) and the state equation:

$$\frac{D\rho'}{Dt} = \kappa\Delta\rho, \tag{A.1.20}$$

where $\rho' = \rho - \rho_0$ is the Boussinesq density and κ can take the value of κ_T or κ_S, depending if temperature or salt dominates the density field. Under this assumption the energy and salt equations have been merged into a density equation, which is not to be confused with mass conservation.

In summary, the Boussinesq approximation, rooted in the assumption that the density does not move away much from a mean value, has allowed the replacement of the actual density ρ by its reference density ρ_0 everywhere, except in the term of the gravitational force, and in the energy equation, which has become an equation governing density variations (Cushman-Roisin & Beckers, 2011). At this point, since the original variables ρ and p no longer appear in the equations, it is customary to drop the primes from ρ' and p' without risk of ambiguity. From hereinafter, the variables ρ and p will denote the perturbation density or Boussinesq density and the perturbation pressure, respectively.

Appendix B

Internal gravity waves

In this appendix we briefly introduce the main linear gravity waves involved in this thesis. In presence of horizontal boundaries, a stratified and rotating flow can admit the existence of two type of gravitational oscillations, the so-called Kelvin and Poincare waves. Here we present the derivation of the normal modes that characterize the Poincaré and Kelvin waves in a smooth two-layer stratified cylindrical domain.

B.1 Equations of motion

We consider an inviscid stratified fluid with a background density $\bar{\rho}(z)$, contained in a cylindrical domain $\mathscr{C}$ of depth H, bounded both above and below by flat rigid boundaries, with outer vertical boundary, $\partial\mathscr{C}$, at $r = R$. Then, the linearized equations of motions on an f-plane are:

$$\frac{\partial \vec{v}}{\partial t} + f\hat{k} \times \vec{v} = -\frac{1}{\rho_0}\nabla p - \frac{\rho}{\rho_0} g\hat{k}, \tag{B.1.1a}$$

$$\nabla \cdot \vec{v} = 0, \tag{B.1.1b}$$

$$\frac{\partial \rho}{\partial t} + w\frac{\mathrm{d}\bar{\rho}}{\mathrm{d}z} = 0, \tag{B.1.1c}$$

where $\vec{v} = (u, v, w)^t$ is the vector velocity field, p is the pressure field, ρ_0 is the reference density, ρ is the Boussinesq density and g is gravity. Here u and v denote the radial and azimuthal velocity components, respectively, whereas w denotes the vertical velocity component. The boundary condition is the following:

$$\vec{v} \cdot \hat{n} = 0 \quad \text{on } \partial\mathscr{C}, \tag{B.1.2}$$

where $\hat{n}$ is the unit inward normal for $\partial\mathscr{C}$.

B.1.1 Wave equation and modal structure

Via a suitable combination of mathematical operations of (B.1.1), we derive a wave equation for the vertical velocity component, w:

$$\left\{\frac{\partial^2}{\partial t^2} + f^2\right\}\frac{\partial^2 w}{\partial z^2} + \left\{\frac{\partial^2}{\partial t^2} + \mathcal{N}^2(z)\right\}\Delta_H w = 0, \tag{B.1.3}$$

where Δ_H is the horizontal Laplace operator and $\mathcal{N}(z) = \sqrt{-(g/\rho_0)\mathrm{d}_z\bar{\rho}}$ is the buoyancy frequency. We search modal solutions of the type:

$$\tilde{w}(r, \theta, z, t) = \mathcal{A}_w \mathcal{W}(r, z)\sin(n\theta - \omega t - \varphi) \tag{B.1.4}$$

where $\mathcal{A}_w$ is the modal amplitude and $\mathcal{W}(r,z)$ is radial and vertical modal structure of w, $n \in \{1,2,3,...\}$ is the azimuthal mode, and φ is a wave phase. Substituting (B.1.4) into (B.1.3) yields:

$$\left(\frac{\omega^2 - f^2}{\omega^2 - \mathcal{N}^2}\right)\frac{\partial \mathcal{W}}{\partial z^2} + \frac{\partial^2 \mathcal{W}}{\partial r^2} + \frac{1}{r}\frac{\partial W}{\partial r} - \frac{n^2}{r^2}\mathcal{W} = 0. \tag{B.1.5}$$

Assuming the radial structure is uncoupled of the vertical structure, then we can express $\mathcal{W}(r,z) = G_w(r)\cdot\mathcal{F}_w(z)$, where G_w and $\mathcal{F}_w$ denote the radial and vertical modal structure, respectively. Substituting $\mathcal{W}(r,z) = G_w(r)\cdot\mathcal{F}_w(z)$ into (B.1.5) and dividing by $G_w(r)\cdot\mathcal{F}_w(z)$, the equation (B.1.5) is reduced to

$$\left(\frac{\omega^2 - f^2}{\omega^2 - \mathcal{N}^2}\right)\frac{1}{\mathcal{F}_w}\frac{\mathrm{d}^2\mathcal{F}_w}{\mathrm{d}z^2} + \frac{1}{G_w}\left(\frac{\mathrm{d}^2 G_w}{\mathrm{d}r^2} + \frac{1}{r}\frac{\mathrm{d}G_w}{\mathrm{d}r} - \frac{n^2}{r^2}G_w\right) = 0. \tag{B.1.6}$$

The last expression can be written as follows:

$$\frac{1}{G_w}\left(\frac{\mathrm{d}^2 G_w}{\mathrm{d}r^2} + \frac{1}{r}\frac{\mathrm{d}G_w}{\mathrm{d}r} - \frac{n^2}{r^2}G_w\right) = -\left(\frac{\omega^2 - f^2}{\omega^2 - \mathcal{N}^2}\right)\frac{1}{\mathcal{F}_w}\frac{\mathrm{d}^2\mathcal{F}_w}{\mathrm{d}z^2} = -\alpha^2, \tag{B.1.7}$$

where α is an arbitrary complex parameter. Hence, we have two ordinal differential equation (ODE) instead of one partial differential equation for $\mathcal{W}$:

$$\frac{\mathrm{d}^2\mathcal{F}_w}{\mathrm{d}z^2} + \alpha^2\left(\frac{\mathcal{N}^2(z) - \omega^2}{\omega^2 - f^2}\right)\mathcal{F}_w = 0, \tag{B.1.8a}$$

$$\frac{\mathrm{d}^2 G_w}{\mathrm{d}r^2} + \frac{1}{r}\frac{\mathrm{d}G_w}{\mathrm{d}r} - \left(\frac{n^2}{r^2} - \alpha^2\right)G_w = 0. \tag{B.1.8b}$$

Boundary conditions for (B.1.8) are directly derived from (B.1.2) and the algebra is detailed in Sub-Appendix B.3:

$$\mathcal{F}_w = 0, \quad \text{at} \;\; z = 0, H, \tag{B.1.9a}$$

$$\left(\frac{f}{r}\frac{\partial}{\partial\theta} + \frac{\partial^2}{\partial t\partial r}\right)G_w(r)\sin\left(n\theta - \omega t - \varphi\right) = 0 \quad \text{at} \;\; r = R. \tag{B.1.9b}$$

B.1.2 Stratification: $\bar{\rho}$, $\mathcal{N}$

To solve the equations (B.1.8) we require to know the background stratification. In general terms, the environmental stratification can be characterized by a scalar density field:

$$\rho(\vec{x},t) = \rho_0 + \bar{\rho}(z,t) + \rho'(\vec{x},t) \tag{B.1.10}$$

where ρ_0 is the reference density, $\bar{\rho}(z,t)$ is the background density profile, which depends of the z–coordinate and time t, and $\rho'(\vec{x},t)$ is the perturbed density component. In order to calculate the vertical structure of normal modes we will assume $\rho'(\vec{x},t) = 0$, and a monotonic decreasing density function $\bar{\rho}(z,t)$ in terms of z (stable stratification) for a specific time $t = t_0$. A continuous two-layer density profile has been characterized by the following function:

$$\bar{\rho}(z,t_0) = \Delta\rho\frac{z_\mathrm{i}}{H} + \sum_{k=1}^{\infty} a_k \cos\left(k\pi\frac{z}{H}\right)\mathrm{e}^{-\gamma_k t_0}, \tag{B.1.11}$$

with

$$a_k = 2\frac{\Delta\rho}{k\pi}\sin\left(k\pi\frac{z_{\rm i}}{H}\right), \quad \gamma_k = \frac{(k\pi)^2\,\mathcal{D}_c}{H^2}, \quad t_0 = \frac{\delta_{\rm i}^2}{\mathcal{D}_c}, \tag{B.1.12}$$

where $z_{\rm i} = h_2$ is the position of the density interface, measured from the bottom upward, $\Delta\rho = \rho_2 - \rho_1$ is the density difference among the bottom layer and the top layer, $\mathcal{D}_c$ represents a diffusion coefficient, and $\delta_{\rm i}$ is a length scale that characterizes the thickness of the transition among the bottom layer and the top layer. All the above parameters must to be known to define the density vertical structure. From (B.1.11) we derive the vertical buoyancy frequency structure $\mathcal{N}(z)$:

$$\mathcal{N}(z) = \sqrt{-\frac{g}{\rho_0}\frac{{\rm d}\bar{rho}}{{\rm d}z}} = \sqrt{\frac{g'}{H/2}}\left\{\sum_{k=1}^{\infty}\sin\left(k\pi\frac{z_{\rm i}}{H}\right)\sin\left(k\pi\frac{z}{H}\right){\rm e}^{-\gamma_k t_0}\right\}^{1/2}. \tag{B.1.13}$$

Figure B.1.1 show the vertical structure of the background density.

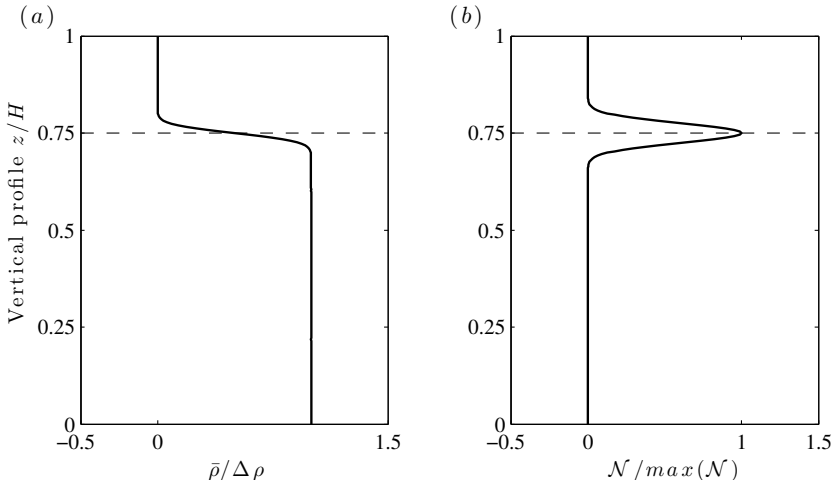

Figure B.1.1: (a) Background density profile $\bar{\rho}(z)/\Delta\rho$. (b) Background buoyancy frequency $\mathcal{N}(z)/\max(\mathcal{N})$

B.1.3 Bounds of the wave frequency: ω

Before to solve (B.1.8a) and obtain $\mathcal{F}_w(z)$, we can study the bounds of the wave frequency ω in terms of the α-value. For this, we apply and integral technique similar to that used to analyse the stability of shear flows. First, we multiply equation (B.1.8a) by the complex conjugate $\mathcal{F}_w^*$, obtaining:

$$\frac{{\rm d}^2\mathcal{F}_w}{{\rm d}z^2}\mathcal{F}_w^* + \alpha^2\left(\frac{\mathcal{N}^2(z)-\omega^2}{\omega^2-f^2}\right)\mathcal{F}_w\mathcal{F}_w^* = \frac{\rm d}{{\rm d}z}\left(\frac{{\rm d}\mathcal{F}_w}{{\rm d}z}\mathcal{F}_w^*\right) - \frac{{\rm d}\mathcal{F}_w}{{\rm d}z}\frac{{\rm d}\mathcal{F}_w^*}{{\rm d}z} + \alpha^2\left(\frac{\mathcal{N}^2(z)-\omega^2}{\omega^2-f^2}\right)\mathcal{F}_w\mathcal{F}_w^*. \tag{B.1.14}$$

Second, rewritting $\mathcal{F}_w\mathcal{F}_w^* = |\mathcal{F}(z)|^2$ and $({\rm d}\mathcal{F}_w/{\rm d}z)({\rm d}\mathcal{F}_w^*/{\rm d}z) = |{\rm d}\mathcal{F}/{\rm d}z|^2$ and integrating vertically across the domain equation (B.1.14), we obtain:

$$\int_0^H \frac{\rm d}{{\rm d}z}\left(\frac{{\rm d}\mathcal{F}_w}{{\rm d}z}\mathcal{F}_w^*\right){\rm d}z - \int_0^H\left|\frac{{\rm d}\mathcal{F}(z)}{{\rm d}z}\right|^2{\rm d}z + \int_0^H\alpha^2\left(\frac{\mathcal{N}^2(z)-\omega^2}{\omega^2-f^2}\right)|\mathcal{F}(z)|^2{\rm d}z = 0. \tag{B.1.15}$$

Then, we can perform an integration by part on the first term of (B.1.15) and use the boundary conditions (B.1.9a), obtaining the following relationship:

$$\int_0^H \left|\frac{\mathrm{d}\mathcal{F}(z)}{\mathrm{d}z}\right|^2 \mathrm{d}z = \int_0^H \alpha^2 \left(\frac{\mathcal{N}^2(z)-\omega^2}{\omega^2-f^2}\right) |\mathcal{F}(z)|^2 \mathrm{d}z. \tag{B.1.16}$$

The left-hand term corresponds to a non-negative quantity, therefore the right-hand term must to satisfy the same condition. In the case of $\alpha^2 > 0$, as long as ω is real, we must impose

$$\frac{\mathcal{N}^2(z)-\omega^2}{\omega^2-f^2} \geq 0 \tag{B.1.17}$$

From (B.1.17) and assuming $f^2 < \mathcal{N}^2$, the common situation, we can define a range of values for the wave frequency:

$$f^2 \leq \omega^2 \leq \mathcal{N}^2_{\max} \tag{B.1.18}$$

This means when $\alpha^2 > 0$, we expect, as solutions, super-inertial wave frequencies. The normal modes with this type of frequency are usually called Poincaré waves. In the case of $\alpha^2 < 0$, as long as ω is real, we must impose

$$\frac{\mathcal{N}^2(z)-\omega^2}{\omega^2-f^2} \leq 0 \tag{B.1.19}$$

From (B.1.19) and assuming $f^2 < \mathcal{N}^2$, the common situation, we can define two possible range of values for the wave frequency:

$$\omega^2 \leq f^2 \leq \mathcal{N}^2_{\max} \quad \text{or} \quad f^2 \leq \mathcal{N}^2_{\max} \leq \omega^2 \tag{B.1.20}$$

This means when $\alpha^2 < 0$, we expect, as solutions, sub-inertial wave frequencies. The normal modes with this type of frequency are usually called Kelvin waves. The second range, in which $\mathcal{N}^2_{\max} \leq \omega^2$, cannot be possible in linear internal wave theory. In both cases we can note that if a wave frequency ω exists, so does one of frequency $-\omega$, corresponding to propagation in the opposite direction.

To obtain $\tilde{w}$ we require to solve (B.1.8); both equations depend of α and ω. First, we focus the analysis in the cases $\alpha^2 < 0$ and $\alpha^2 > 0$, where the particular case $\alpha^2 = 0$ is discussed the Sub-Appendix B.4.

B.1.4 Sub-inertial modes: $\alpha^2 < 0$, $(\omega/f)^2 < 1$

We consider that $\alpha^2 < 0$. Just for mathematical convenience a new parameter β is defined as $\beta^2 = -\alpha^2$. Then, using a stretch variable $r_\beta = \beta r$ and substituting $r = \beta^{-1} r_\beta$ in (B.1.8b) yields a new ODE for G in terms of r_β:

$$\frac{\mathrm{d}^2 G_w}{\mathrm{d}r_\beta^2} + \frac{1}{r_\beta}\frac{\mathrm{d}G_w}{\mathrm{d}r_\beta} - \left(\frac{n^2}{r_\beta^2}+1\right) G_w = 0. \tag{B.1.21}$$

Equation (B.1.21) corresponds to a Modified Bessel equation whose solutions are Modified Bessel functions (Abramowitz & Stegun, 1965):

$$G_w(r) = AI_n(\beta r) + BK_n(\beta r). \tag{B.1.22}$$

Here I_n is the first kind Modified Bessel function and K_n is the second kind Modified Bessel function, A and B are constant and n is the azimuthal mode. Since $K_n(\beta r) \to \infty$ as $r \to 0$, we must have $B = 0$. Hence,

$$\tilde{w}(r,\theta,z,t) = \mathcal{A}_w \mathcal{F}_w(z) I_n(\beta r) \sin\left(n\theta - \omega t - \varphi\right) \tag{B.1.23}$$

The structure of $\mathcal{F}_w(z)$ is obtained solving (B.1.8a) given the density structure $\bar{\rho}(z)$. The wave frequency, ω, is obtained substituting $G_w(r)$ in the boundary condition (B.1.9b).

$$\frac{fn}{R} I_n(\beta R) - \omega\beta \frac{\mathrm{d}I_n(\beta R)}{\mathrm{d}r_\beta} = 0. \tag{B.1.24}$$

The last expression corresponds to a dispersion equation for the eigenvalues β and ω. Solving the modal velocity $\tilde{w}$, we proceed to find the modal density $\tilde{\rho}$ from (B.1.1c):

$$\frac{\partial \tilde{\rho}}{\partial t} + w\frac{\mathrm{d}\bar{\rho}}{\mathrm{d}z} = -\omega\, G_\rho(r)\mathcal{F}_\rho(z)\sin\left(n\theta - \omega t - \varphi\right) + \mathcal{A}_w I_n(\beta r)\mathcal{F}_w(z)\sin\left(n\theta - \omega t - \varphi\right)\frac{\partial \bar{\rho}}{\partial z} = 0 \tag{B.1.25}$$

yields,

$$\tilde{\rho}(r,\theta,z,t) = \frac{\mathcal{A}_w}{\omega} I_n(\beta r)\left[\frac{\mathrm{d}\bar{\rho}}{\mathrm{d}z}\mathcal{F}_w(z)\right]\cos\left(n\theta - \omega t - \varphi\right). \tag{B.1.26}$$

From the vertical component of the momentum equation (B.1.1) we derive the modal pressure, $\tilde{p}$:

$$\frac{\partial \tilde{p}}{\partial z} = -\rho_0 \frac{\partial w}{\partial t} - g\rho = A\rho_0 G_w(r)\left(\frac{\omega^2 - \mathcal{N}^2(z)}{\omega}\right)\mathcal{F}_w(z)\cos(n\theta - \omega t - \varphi). \tag{B.1.27}$$

Then, using the EDO (B.1.8a), yields

$$\tilde{p}(r,\theta,z,t) = -\mathcal{A}_w\rho_0\left(\frac{\omega^2 - f^2}{\beta^2\omega}\right) I_n(\beta r)\frac{\mathrm{d}\mathcal{F}_w(z)}{\mathrm{d}z}\cos(n\theta - \omega t - \varphi). \tag{B.1.28}$$

Finally, from the horizontal components of the momentum equation (B.1.1) and (B.1.28), we obtain the modal structure for $\tilde{u}$ and $\tilde{v}$:

$$\tilde{u}(r,\theta,z,t) = \frac{\mathcal{A}_w}{\beta^2}\left\{n\left(\frac{f}{\omega}\right)\frac{I_n(\beta r)}{r} - \frac{\mathrm{d}I_n(\beta r)}{\mathrm{d}r}\right\}\frac{\mathrm{d}\mathcal{F}_w(z)}{\mathrm{d}z}\sin(n\theta - \omega t - \varphi), \tag{B.1.29a}$$

$$\tilde{v}(r,\theta,z,t) = -\frac{\mathcal{A}_w}{\beta^2}\left\{n\frac{I_n(\beta r)}{r} - \left(\frac{f}{\omega}\right)\frac{\mathrm{d}I_n(\beta r)}{\mathrm{d}r}\right\}\frac{\mathrm{d}\mathcal{F}_w(z)}{\mathrm{d}z}\cos(n\theta - \omega t - \varphi). \tag{B.1.29b}$$

B.1.5 Super-inertial modes: $\alpha^2 > 0$, $(\omega/f)^2 > 1$

We consider that $\alpha^2 > 0$. Using a stretch variable $r_\alpha = \alpha r$ and substituting $r = \alpha^{-1} r_\alpha$ in (B.1.8b) yields a new ODE for G in terms of r_α:

$$\frac{\mathrm{d}^2 G_w}{\mathrm{d}r_\alpha^2} + \frac{1}{r_\alpha}\frac{\mathrm{d}G_w}{\mathrm{d}r_\alpha} - \left(\frac{n^2}{r_\alpha^2} - 1\right)G_w = 0. \tag{B.1.30}$$

Equation (B.1.30) corresponds to a Bessel equation whose solutions are Bessel functions (Abramowitz & Stegun, 1965):

$$G_w(r) = AJ_n\left(\alpha r\right) + BY_n\left(\alpha r\right). \tag{B.1.31}$$

Here J_n is the first kind Bessel function and Y_n is the second kind Bessel function, A and B are constant and n is the azimuthal mode. Since $Y_n(\beta r) \to \infty$ as $r \to 0$, we must have $B = 0$. Hence,

$$\tilde{w}(r,\theta,z,t) = \mathcal{A}_w \mathcal{F}_w(z) J_n(\alpha r) \sin\left(n\theta - \omega t - \varphi\right) \tag{B.1.32}$$

The wave frequency, ω, is obtained substituting $G_w(r)$ in the boundary condition (B.1.9b).

$$\frac{fn}{R} J_n(\alpha R) - \omega\alpha \frac{\mathrm{d}J_n(\alpha R)}{\mathrm{d}r_\alpha} = 0. \tag{B.1.33}$$

The last expression corresponds to a dispersion equation for the eigenvalues α and ω. Analogously to the previous case, from $\tilde{w}$ we proceed to find $\tilde{\rho}$, $\tilde{p}$, $\tilde{u}$ and $\tilde{v}$:

$$\tilde{\rho}(r,\theta,z,t) = \frac{\mathcal{A}_w}{\omega} J_n(\beta r) \left[\frac{\mathrm{d}\bar{\rho}}{\mathrm{d}z} \mathcal{F}_w(z)\right] \cos\left(n\theta - \omega t - \varphi\right). \tag{B.1.34a}$$

$$\tilde{p}(r,\theta,z,t) = \mathcal{A}_w \rho_0 \left(\frac{\omega^2 - f^2}{\alpha^2 \omega}\right) J_n(\alpha r) \frac{\mathrm{d}\mathcal{F}_w(z)}{\mathrm{d}z} \cos(n\theta - \omega t - \varphi). \tag{B.1.34b}$$

$$\tilde{u}(r,\theta,z,t) = \frac{\mathcal{A}_w}{\alpha^2} \left\{ n \left(\frac{f}{\omega}\right) \frac{J_n(\alpha r)}{r} - \frac{\mathrm{d}J_n(\alpha r)}{\mathrm{d}r} \right\} \frac{\mathrm{d}\mathcal{F}_w(z)}{\mathrm{d}z} \sin(n\theta - \omega t - \varphi), \tag{B.1.34c}$$

$$\tilde{v}(r,\theta,z,t) = -\frac{\mathcal{A}_w}{\alpha^2} \left\{ n \frac{J_n(\alpha r)}{r} - \left(\frac{f}{\omega}\right) \frac{\mathrm{d}J_n(\alpha r)}{\mathrm{d}r} \right\} \frac{\mathrm{d}\mathcal{F}_w(z)}{\mathrm{d}z} \cos(n\theta - \omega t - \varphi). \tag{B.1.34d}$$

B.2 Eigenvalue & eigenvector problem: G_w, $\mathcal{F}_w(z)$

To characterize G_w and $\mathcal{F}_w(z)$ we must obtain the eigenvalues α and ω. For this, we must solve equation (B.1.8a) and equations (B.1.24), (B.1.33), depending if $\alpha^2 < 0$ or $0 < \alpha^2$, respectively. The solution of both type of equations requires numerical approaches, which means spatial discretization, and hence, discrete solutions for the wave numbers and frequencies. In addition, from each couple of α and ω we can obtain the respective discrete phase velocity, c, via the dispersion relation:

$$c^2 = \frac{\omega^2 - f^2}{\alpha^2} \tag{B.2.1}$$

The relation (B.2.1) can be written in dimensionless terms introducing the radius of deformation $\mathcal{R}_o = c/f$ and the horizontal length scale, R:

$$\alpha^2 R^2 = \frac{\sigma^2 - 1}{\mathcal{B}^2}, \tag{B.2.2}$$

where $\sigma^2 = \omega^2/f^2$ is the dimensionless wave frequency, and $\mathcal{B} = \mathcal{R}_o/R$, hereinafter denoted as the Burger number. Therefore, the set of equations (B.1.8a), (B.1.24), (B.1.33) can be solved in terms of σ and $\mathcal{B}$:

$$\frac{\sqrt{1-\sigma^2}}{\mathcal{B}} I_{n-1}\left(\frac{\sqrt{1-\sigma^2}}{\mathcal{B}}\right) + n\left(\frac{1}{\sigma} - 1\right) I_n\left(\frac{\sqrt{1-\sigma^2}}{\mathcal{B}}\right) = 0, \quad \text{for} \quad \alpha^2 < 0. \tag{B.2.3a}$$

$$\frac{\sqrt{\sigma^2-1}}{\mathcal{B}}J_{n-1}\left(\frac{\sqrt{\sigma^2-1}}{\mathcal{B}}\right)+n\left(\frac{1}{\sigma}-1\right)J_n\left(\frac{\sqrt{\sigma^2-1}}{\mathcal{B}}\right)=0,\quad \text{for}\quad \alpha^2>0. \tag{B.2.3b}$$

$$\frac{\mathrm{d}^2\mathcal{F}_w}{\mathrm{d}z_*^2}+(H\alpha)^2\left(\frac{[\mathcal{N}(z)/f]^2-\sigma^2}{\sigma^2-1}\right)\mathcal{F}_w=0, \tag{B.2.4}$$

where $z_*=z/H\in[0,1]$ is the dimensionless vertical coordinate. Then, setting the value of $\mathcal{B}$, we can obtain σ through the numerical solution of the nonlinear equations (B.2.3a)-(B.2.3b). Once knowing σ and $\mathcal{B}$, we obtain the eigenvalue α and the respective eigenvector $\mathcal{F}_w$ via the solution of (B.2.4).

We address the numerical problem via a straightforward finite-difference technique, adopting a uniform grid spacing Δz. We define the first and last grid point on the flat bottom and at the rigid lid, respectively, since the boundary conditions on the $\mathcal{F}_w$ are imposed there. Dividing the vertical domain ($0\leq z\leq H$) in m grid points, the discrete version of z is given by:

$$z_\ell=\Delta z(\ell-1),\quad \text{with}\quad \Delta z=H/(m-1)\quad \text{and}\quad \ell\in\{1,2,3,...,m\}\,. \tag{B.2.5}$$

The ODE (B.2.4) can be written in its discrete version as following:

$$\mathcal{F}_w(z_{\ell+1})-2\mathcal{F}_w(z_\ell)+\mathcal{F}_w(z_{\ell-1})+\alpha_*^2\mathcal{L}(z_\ell)\mathcal{F}_w(z_\ell)=0, \tag{B.2.6a}$$

$$\mathcal{F}_w(z_1)=0,\qquad \mathcal{F}_w(z_m)=0, \tag{B.2.6b}$$

with

$$\alpha_*^2=(\Delta z\cdot\alpha)^2\,,\quad \mathcal{L}(z_\ell)=\left(\frac{[\mathcal{N}(z_\ell)/f]^2-\sigma^2}{\sigma^2-1}\right). \tag{B.2.7}$$

Hereinafter $\mathcal{F}_w(z_\ell)=\mathcal{F}_\ell$ and $\mathcal{L}(z_\ell)=\mathcal{L}_\ell$. This problem can be set in a matrix form as follows:

$$\mathbb{M}(\alpha_*^2)\vec{\mathcal{F}}=0, \tag{B.2.8}$$

where $\mathbb{M}$ is a tridiagonal matrix that depends on α_*^2. The possible eigenvalue α_* are those that allow a nonzero $\vec{\mathcal{F}}$, and this occurs if the system is singular:

$$\det\left[\mathbb{M}\right]=0. \tag{B.2.9}$$

The problem is reduced to finding the zeros of the determinant of $\mathbb{M}$. For each value ω^2 for which $\det\left[\mathbb{M}(\alpha_*^2)\right]=0$, the corresponding discretized spatial eigenmode $\vec{\mathcal{F}}$ is a solution of (B.2.8). Equation (B.2.6) can be written as a generalized eigenvalue problem:

$$\mathbb{A}\vec{\mathcal{F}}=\alpha_*^2\mathbb{B}\vec{\mathcal{F}}, \tag{B.2.10}$$

where $\mathbb{A}$ and $\mathbb{B}$ are tridiagonal matrices and independent of α_*^2, with the following structure

$$\mathbb{A}=\begin{bmatrix}2&-1&0&\dots&0&0\\-1&2&-1&\dots&0&0\\0&-1&2&\dots&\vdots&\vdots\\\vdots&\vdots&\vdots&\ddots&-1&0\\0&0&\dots&-1&2&-1\\0&0&\dots&0&-1&2\end{bmatrix},\quad \mathbb{B}=\begin{bmatrix}\mathcal{L}_1&0&0&\dots&0&0\\0&\mathcal{L}_2&0&\dots&0&0\\0&0&\mathcal{L}_3&\dots&\vdots&\vdots\\\vdots&\vdots&\vdots&\ddots&0&0\\0&0&\dots&0&\mathcal{L}_{n-1}&0\\0&0&\dots&0&0&\mathcal{L}_n\end{bmatrix}. \tag{B.2.11}$$

Furthermore, $\mathbb{A}$ and $\mathbb{B}$ are symmetric positive definite matrices, since both are diagonally dominant. Figures B.2.1 and B.2.1 show examples of the modal structure of the velocity field $(\tilde{u}, \tilde{v}, \tilde{w})$ for $\mathcal{B} = 0.25$.

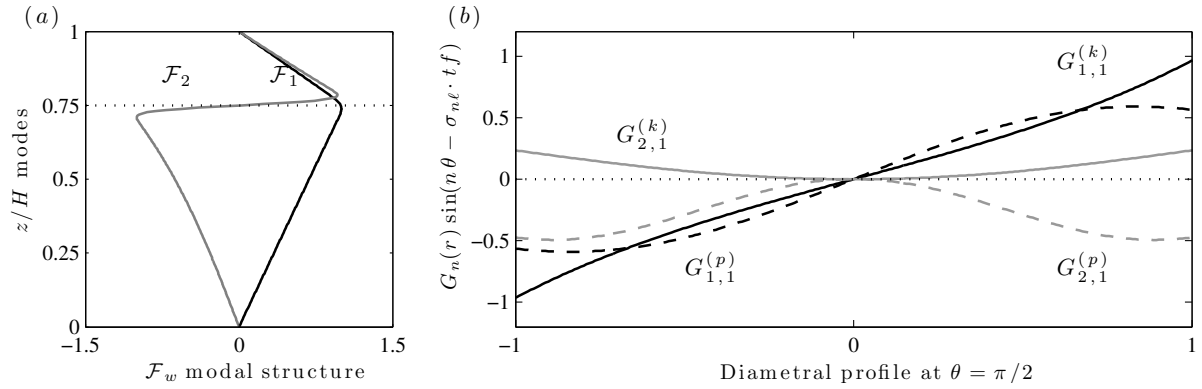

Figure B.2.1: (a) Vertical modal structure $\mathcal{F}_\ell(z)$ of the vertical velocity component, $\tilde{w}$. (b) Horizontal modal structure $G_n(r)\sin(n\theta - \sigma_{n\ell}\cdot tf)$ at $\theta = \pi/2$ of the vertical velocity component w. Super-index, k : Kelvin wave, p : Poincaré wave. Sub-index, n : azimuthal mode, ℓ : vertical mode.

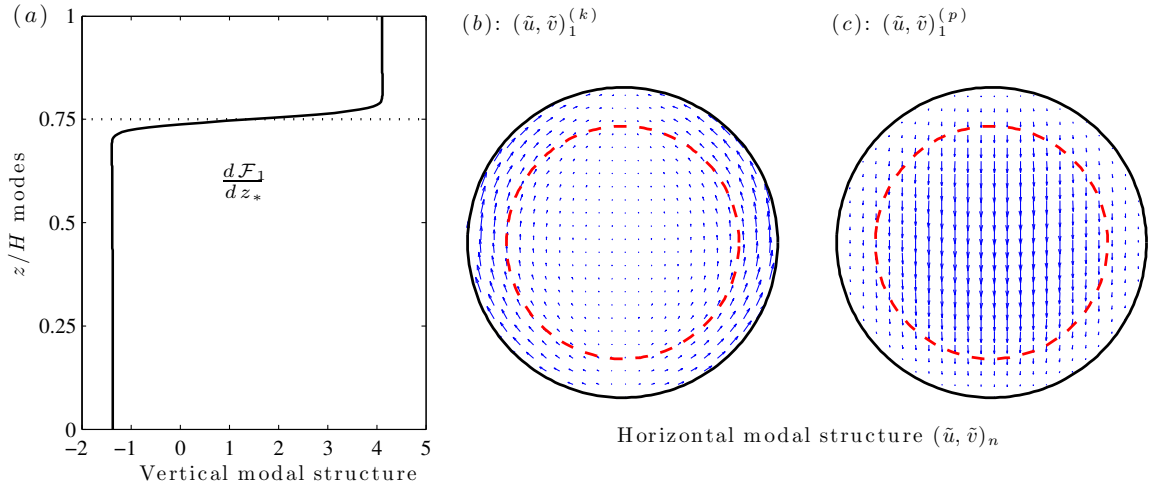

Figure B.2.2: (a) Vertical modal structure $\mathrm{d}\mathcal{F}_\ell(z)/\mathrm{d}z_*$ of the horizontal velocity components, $(\tilde{u}, \tilde{v})$. Sub-index, ℓ : vertical mode. (b) Horizontal modal structure of the horizontal velocity components $(\tilde{u}, \tilde{v})$. Super-index, k : Kelvin wave, p : Poincaré wave. Sub-index, n : azimuthal mode.

B.3 Boundary condition for w at $r = R$

The vertical boundary conditions of w come directly into F_w; however, in the case of the radial boundary condition, we require to write u in terms of w. First, from (B.1.1a) u can be written in terms of the pressure field:

$$\left(\frac{\partial^2}{\partial t^2} + f^2\right) u = -\left(\frac{f}{\rho_0 r}\frac{\partial}{\partial\theta} + \frac{1}{\rho_0}\frac{\partial^2}{\partial t \partial r}\right) p. \tag{B.3.1}$$

From (B.1.1a) and (B.1.1c), w can be also written in terms of the pressure field:

$$\left(\frac{\partial^2}{\partial t^2}+\mathcal{N}^2(z)\right)w=-\frac{1}{\rho_0}\frac{\partial^2 p}{\partial t\partial z}. \tag{B.3.2}$$

From (B.3.1) and (B.3.2) we eliminate the pressure field and write w in terms of u:

$$\left(\frac{f}{r}\frac{\partial}{\partial\theta}+\frac{\partial^2}{\partial t\partial r}\right)\left(\frac{\partial^2}{\partial t^2}+\mathcal{N}^2(z)\right)w=\left(\frac{\partial^4}{\partial z\partial t^3}+f^2\right)u. \tag{B.3.3}$$

Then, at the boundary $r=R$, $u=0$, resulting in:

$$\left(\frac{f}{r}\frac{\partial}{\partial\theta}+\frac{\partial^2}{\partial t\partial r}\right)\left(\frac{\partial^2}{\partial t^2}+\mathcal{N}^2(z)\right)w=0 \tag{B.3.4}$$

Substituting (B.1.4) into (B.3.4) yields:

$$\left(\frac{f}{r}\frac{\partial}{\partial\theta}+\frac{\partial^2}{\partial t\partial r}\right)G_w(r)\sin\left(n\theta-\omega t-\varphi\right)=0 \quad \text{at} \quad r=R,\ \ \theta\in[0,2\pi]\,,\ \ z\in[0,\ H], \tag{B.3.5}$$

whereas substituting (B.1.4) into (B.1.2) yields:

$$\mathcal{F}_w=0, \quad \text{at} \quad z=0,H,\ \ \theta\in[0,2\pi]\,,\ \ r\in[0,R]\,. \tag{B.3.6}$$

B.4 Modal structure: case $\alpha^2=0$

We analyse the particular case $\alpha^2=0$. Then, the EDOs (B.1.8) are reduced to:

$$\left(\omega^2-f^2\right)\frac{\mathrm{d}^2\mathcal{F}_w}{\mathrm{d}^2 z}=0, \tag{B.4.1a}$$

$$\frac{\mathrm{d}^2 G_w}{\mathrm{d}r^2}+\frac{1}{r}\frac{\mathrm{d}G_w}{\mathrm{d}r}-\frac{n^2}{r^2}G_w=0. \tag{B.4.1b}$$

From (B.4.1a) is obtained that if $\omega^2\neq f^2$, yields:

$$\mathcal{F}_w(z)=Az+B, \tag{B.4.2}$$

where A and B are constants. Substituting the boundary conditions $\mathcal{F}_w(z=0)=0$ and $\mathcal{F}_w(z=H)=0$, it is obtained a trivial solution:

$$\mathcal{F}_w(z)=0. \tag{B.4.3}$$

For non-trivial solutions, $\mathcal{F}_w(z)\neq 0$, hence $\omega=\pm f$, and $\mathcal{F}_w(z)$ can take any form as long as it satisfies the boundary conditions. Meanwhile (B.4.1b) corresponds to a Euler equation, and therefore we can propose solutions as the following:

$$G_w(r)=Ar^n+Br^{-n}, \tag{B.4.4}$$

where A and B are constants. In the same way than previous cases, $G_w(r) < \infty$ when $r \to 0$, hence $B = 0$. The solution for the radial structure is:

$$G_w(r) = Ar^n. \tag{B.4.5}$$

Substituting $G_w(r)$ in the boundary condition (B.1.9a), yields:

$$-\omega n R^{n-1} + fn\frac{R^n}{R} = 0 \quad \to \quad \omega = f. \tag{B.4.6}$$

Hence, for the particular case $\alpha = 0$, the wave frequency takes the value of the inertial frequency, but it is not possible to obtain an analytical expression for $\tilde{w}$ because the vertical structure $\mathcal{F}_w$ is undefined.

Bibliography

Abramowitz, M., & Stegun, A. 1965. *Handbook of Mathematical Functions: With Formulas, Graphs, and Mathematical Tables.* Dover.

Almgren, A., Camassa, R., & Tiron, R. 2012. Shear instability of internal solitary waves in Euler fluids with thin pycnoclines. *J. Fluid Mech.*, **710**, 324–361, dx.doi.org/10.1017/jfm.2012.366.

Antenucci, J., & Imberger, J. 2001. Energetics of long internal gravity waves in large lakes. *Limnol. Oceanogr.*, **46**, 1760–1773, dx.doi.org/10.4319/lo.2001.46.7.1760.

Appt, J., Imberger, J., & Kobus, H. 2004. Basin-scale motion in stratified Upper Lake Constance. *Limnol. Oceanogr.*, **4**, 919–933, dx.doi.org/10.4319/lo.2004.49.4.0919.

Barad, M. F., & Fringer, O. B. 2010. Simulations of shear instabilities in interfacial gravity waves. *J. Fluid Mech.*, **644**, 61–95, dx.doi.org/10.1017/S0022112009992035.

Barry, M. E., Ivey, G. N., Winters, K. B., & Imberger, J. 2001. Measurements of diapycnal diffusivities in stratified fluids. *J. Fluid Mech.*, **442**, 267–291, dx.doi.org/10.1017/S0022112001005080.

Beletsky, D., O'Connor, W. P., Schwab, D. J., & Dietrich, D. E. 1997. Numerical simulation of internal Kelvin waves and costal upwelling fronts. *J. Phys. Oceanogr.*, **27**, 1197–1215, dx.doi.org/10.1175/1520--0485(1997).

Bendat, J., & Piersol, A. 2000. *Random Data.* Wiley. New York.

Boegman, L., & Ivey, G. N. 2009. Flow separation and resuspension beneath shoaling nonlinear internal waves. *J. Geophys. Res.*, **114 C02018**, dx.doi.org/10.1029/2007JC004411.

Boegman, L., Imberger, J., Ivey, G., & Antenucci, J. 2003. High-frequency internal waves in large stratified lakes. *Limnol. Oceanogr.*, **48(2)**, 895–919, dx.doi.org/10.4319/lo.2003.48.2.0895.

Boegman, L., Ivey, G., & Imberger, J. 2005a. The degeneration of internal waves in lakes with sloping topography. *Limnol. Oceanogr.*, **50**, 1620–1637, dx.doi.org/10.4319/lo.2005.50.5.1620.

Boegman, L., Ivey, G., & Imberger, J. 2005b. The energetics of large-scale internal wave degeneration in lakes. *J. Fluid. Mech.*, **531**, 159–180, dx.doi.org.10.1017/S0022112005003915.

Boehrer, B., & Schultze, M. 2008. Stratification of Lakes. *Rev. Geophys.*, **46**, RG2005, dx.doi.org/10.1029/2006RG000210.

Bouffard, D., & Boegman, L. 2013. A diapycnal diffusivity model for stratified environmental flows. *Dynam. Atmos. Oceans*, **61-62**, 14–34, dx.doi.org/10.1016/j.dynatmoce.2013.02.002.

Bouffard, D., & Lemmin, U. 2013. Kelvin waves in Lake Geneva. *J. Great Lakes Res.*, **39(4)**, 637–645, dx.doi.org/10.1016/j.jglr.2013.09.005.

Bouffard, D., Boegman, L., & Rao, Y. 2012. Poincaré wave-induced mixing in a large lake. *Limnol. Oceanogr.*, **57**, 1201–1216, dx.doi.org/10.4319/lo.2012.57.4.1201.

Bouffard, D., Boegman, L., Ackerman, J. D., Valipour, R., & Rao, Y. R. 2014. Near-inertial wave

driven dissolved oxygen transfer through the thermocline of a large lake. *J. Great Lakes Res.*, **40**, 300–307, dx.doi.org/10.1016/j.jglr.2014.03.014.

Carr, M., Fructus, D., Grue, J., Jensen, A., & Davies, P. A. 2008. Convectively induced shear instability in large amplitude internal solitary waves. *Phys. Fluids*, **20**, 126601, dx.doi.org/10.1063/1.3030947.

Carr, M., King, St. E., & Dritschel, D. G. 2011. Numerical simulation of shear-induced instabilities in internal solitary waves. *J. Fluid Mech.*, **683**, 263–288, dx.doi.org/10.1017/jfm.2011.261.

Choi, W., & Camassa, R. 1999. Fully nonlinear internal waves in two-fluid system. *J. Fluid Mech.*, **396**, 1–36, dx.doi.org/10.1017/S0022112099005820.

Csanady, G. 1968. Motions in a model Great Lake due to a suddenly imposed wind. *J. Geophys. Res.*, **73**, 6435–6447, dx.doi.org/10.1029/JB073i020p06435.

Csanady, G. T. 1967. Large-scale motion in the great lakes. *J. Geophys. Res.*, **72**, 4151–4162, dx.doi.org/10.1029/JZ072i016p04151.

Csanady, G. T. 1982. On the Structure of Transient Upwelling Events. *J. Phys. Onceanogr.*, **12**, 84–96, dx.doi.org/10.1175/1520--0485(1982)012<0084:OTSOTU>2.0.CO;2.

Csanady, G.T. 1975. Hydrodynamics of large lakes. *Annu. Rev. Fluid Mech.*, **7**, 347–386, dx.doi.org/10.1146/annurev.fl.07.010175.002041.

Cushman-Roisin, Benoit, & Beckers, Jean-Marie. 2011. *Introduction to Geophysical Fluid Dynamics*. Academic Press.

de la Fuente, A., Shimizu, K., Imberger, J., & Niño, Y. 2008. The evolution of internal waves in a rotating, stratified, circular basin and the influence of weakly nonlinear and nonhydrostatic accelerations. *Limnol. Oceanogr.*, **53(6)**, 2738–2748, dx.doi.org/10.4319/lo.2008.53.6.2738.

de la Fuente, A., Shimizu, K., Niño, Y., & Imberger, J. 2010. Nonlinear and weakly nonhydrostatic inviscid evolution of internal gravitational basin-scale waves in a large, deep lake: Lake Constance. *J. Geophys. Res.*, **115, C12045**, dx.doi.org/10.1029/2009JC005839.

EI, G. A., Grimshaw, R. H. J., & Kamchatnov, A. M. 2005. Analytic model for a weakly dissipative shallow-water undular bore. *Chaos*, **15**, dx.doi.org/10.1063/1.1914743.

EI, G. A., Grimshaw, R. H. J., & Smyth, N. F. 2006. Unsteady undular bores in fully nonlinear shallow-water theory. *Phys. Fluids*, **18**, dx.doi.org/10.1063/1.2175152.

Fedorov, A., & Melville, W. K. 1995. Propagation and breaking of nonlinear Kelvin wave. *J. Phys. Oceanogr.*, **25**, 2518–2531, dx.doi.org/10.1175/1520--0485(1995)025<2518:PABONK>2.0.CO;2.

Flór, J.-B., Scolan, H., & Gula, J. 2011. Frontal instabilities and waves in a differentially rotating fluid. *J. Fluid Mech.*, **685**, 532–542, dx.doi.org/10.1017/jfm.2011.338.

Forel, F. A. 1873. Première étude sur les seiches. *Bulletin de la Société Vaudoise des Sciences Naturelles*, 12:213.

Forel, F. A. 1892. *Le Léman, Monographie Limnologique - Tome Premier*. Librarie de l'Université, Lausanne, https://archive.org/details/lelmanmonograp02fore.

Fructus, D., Carr, M., Grue, J., Jensen, A., & Davies, P. A. 2009. Shear-induced breaking of large internal solitary waves. *J. Fluid Mech.*, **620**, 1–29, dx.doi.org/10.1017/S0022112008004898.

Garcia, C. M., Cantero, M. I., Niño, Y., & Garcia, M. H. 2005. Turbulence measurements with acoustic doppler velocimeters. *J. Hydraul. Eng.*, **131(12)**, 1062–1073, dx.doi.org/10.1061/(ASCE)0733--9429(2005)131:12(1062).

Garrett, C., & Munk, W. 1979. Internal waves in the ocean. *Annu. Rev. Fluid Mech.*, **11**, 339–369, dx.doi.org/10.1146/annurev.fl.11.010179.002011.

Grimshaw, R. H. J. 1985. Evolution equation for weakly nonlinear, long internal waves in a rotating fluid. *Stud. Appl. Math.*, **73**, 1–33.

Grimshaw, R. H. J., & Helfrich, K. 2008. Long-time solutions of the Ostrovsky equation. *Stud. Appl. Math.*, **121**, 71–88, dx.doi.org/10.1111/j.1467--9590.2008.00412.x.

Grimshaw, R. H. J., & Helfrich, K. 2012. The effect of rotation on internal solitary waves. *J. Appl. Math.*, **77**, 326–339, dx.doi.org/10.1093/imamat/hxs024.

Grimshaw, R. H. J., He, J.-M., & Ostrovsky, L. A. 1998. Terminal Damping of a Solitary wave Due to Radiation in Rotational Systems. *Stud. Appl. Math.*, **101**, 289–338, dx.doi.org/10.1111/1467--9590.00090.

Grimshaw, R. H. J., Helfrich, K., & Johnson, E. R. 2012. The reduced Ostrovsky equation: Integrability and Breaking. *Stud. Appl. Math.*, **129**, 414–435, dx.doi.org/10.1111/j.1467--9590.2012.00560.x.

Grimshaw, R. H. J., Helfrich, K. R., & Johnson, E. R. 2013. Experimental study of the effect of rotation on large amplitude internal waves. *Phys. Fluids*, **25**, 056602, dx.doi.org/10.1063/1.4805092.

Grue, J., Jensen, A., Rusas, P.-O., & Sveen, J. K. 1999. Properties of large-amplitude internal waves. *J. Fluid Mech.*, **380**, 257–278, dx.doi.org/10.1017/S0022112098003528.

Grue, J., Jensen, A., Rusas, P.-O., & Sveen, J. K. 2000. Breaking and broadening of internal solitary waves. *J. Fluid Mech.*, **413**, 181–217, dx.doi.org/10.1017/S0022112000008648.

Gula, J., Plougonven, R., & Zeitlin, V. 2009. Ageostrophic instabilities of fronts in a channel in a stratified rotating fluid. *J. Fluid Mech.*, **627**, 485–507, dx.doi.org/10.1017/S0022112009006508.

Hammack, J. L., & Henderson, D. M. 1993. Resonant interactions among surface water waves. *Annu. Rev. Fluid Mech.*, **25**, 55–97, dx.doi.org/10.1146/annurev.fl.25.010193.000415.

Helfrich, K., & Grimshaw, R. H. J. 2008. Nonlinear disintegration of the internal tide. *J. Phys. Oceanogr.*, **38**, 686–701, dx.doi.org/10.1175/2007JPO3826.1.

Helfrich, K., & Melville, W. K. 2006. Long nonlinear internal waves. *Annu. Rev. Fluid Mech.*, **38**, 395–425, dx.doi.org/10.1146/annurev.fluid.38.050304.092129.

Horn, D. A., Imberger, J., & Ivey, G. N. 2001. The degeneration of large-scale interfacial gravity waves in lakes. *J. Fluid Mech.*, **434**, 181–207, dx.doi.org/10.1017/S0022112001003536.

Howard, Louis N. 1961. Note on a paper of John W. Miles. *J. Fluid Mech.*, **10**, 509–512, dx.doi.org/10.1017/S0022112061000317.

Imberger, J., & Hamblin, P. F. 1982. Dynamics of lakes, reservoirs and cooling ponds. *Annu. Rev. Fluid Mech.*, **14**, 153–87, dx.doi.org/10.1146/annurev.fl.07.010175.002041.

Ivey, G. N., Winters, K. B., & Koseff, J. R. 2008. Density Stratification, Turbulence, but How Much Mixing? *Annu. Rev. Fluid Mech.*, **40**, 169–84, dx.doi.org/10.1146/annurev.fluid.39.050905.110314.

Johnson, E. R., & Grimshaw, R. H. J. 2013. Modified reduced Ostrovsky equation: Integrability and breaking. *Phys. Rev. E*, **88**, dx.doi.org/10.1103/PhysRevE.88.021201.

Kamchatnov, A. M., Kuo, Y. H., Lin, T. C., Horng, T. L., Gou, S. C., Clift, R., El, G. A., & Grimshaw, R. H. J. 2012. Undular bore theory for the Garder equation. *Phys. Rev. E*, **86**, dx.doi.org/10.1103/PhysRevE.86.036605.

Katsis, C, & Akylas, T. R. 1987. Solitary internal waves in a rotating channel: A numerical study. *Phys. Fluids*, **30**, 297–301, dx.doi.org/10.1063/1.866377.

Kundu, P., Cohen, I., & Dowling, David R. 2012. *Fluid Mechanics*. Academic Press.

Lamb, H. 1932. *Hydrodynamics*. Dover, 6th ed.

Lamorgese, A. G., Caughey, D. A., & Pope, S. B. 2005. Direct numerical simulation of homogeneous turbulence with hyperviscosity. *Phys. Fluids*, **17**, 015106, dx.doi.org/10.1063/1.1833415.

Lorke, A. 2007. Boundary mixing in the thermocline of a large lake. *J. Geophys. Res.*, **112**, C09019, dx.doi.org/10.1029/2006JC004008.

Lorke, A., Peeters, F., & Bäuerle, E. 2006. High-frequency internal waves in the litoral zone of large lake. *Limnol. Oceanogr.*, **51(4)**, 1935–1936, dx.doi.org/10.4319/lo.2006.51.4.1935.

MacIntyre, S., Clark, J., Jellison, R., & Jonathan, Fram. 2009. Turbulent mixing induced by nonlinear internal waves in Mono Lake, California. *Limnol. Oceanogr.*, **54**, 2255–2272, dx.doi.org/10.4319/lo.2009.54.6.2255.

Martinsen, E., & Weber, J. E. 1981. Frictional influence on internal Kelvin waves. *Tellus*, **33**, 402–410, dx.doi.org/10.1111/j.2153--3490.1981.tb01763.x.

Matsumoto, Y., & Hoshino, M. 2004. Onset of turbulence induced by a Kelvin-Helmholtz vortex. *Geophys. Res. Lett.*, **31**, L02807, dx.doi.org/10.1029/2003GL018195.

Maxworthy, T. 1983. Experiments in solitary internal Kelvin waves. *J. Fluid. Mech.*, **129**, 365–383, dx.doi.org/10.1017/S0022112083000816.

Melville, W. K., Tomasson, G. G., & Renouard, D. P. 1989. On the stability of Kelvin waves. *J. Fluid Mech.*, **206**, 1–23, dx.doi.org/10.1017/S002211208900220X.

Miles, J. W. 1961. On the stability of heterogeneous shear flows. *J. Fluid Mech.*, **10**, 496–508, dx.doi.org/10.1017/S0022112061000305.

Moum, J. N., Farmer, D. M, Smyth, W. D., Armi, L., & Vagle, S. 2003. Structure and generation of turbulence at interface strained by internal solitary waves propagating shoreward over the continental-shelf. *J. Phys. Oceanogr.*, **33**, 2093–2112, dx.doi.org/10.1175/1520--0485(2003)033<2093:SAGOTA>2.0.CO;2.

Murray, J. 1888. On the effecs of winds on the distribution of temperature in the sea and fresh-water Lochs of the west of Sconland. *Scott. Geogr. Mag.*, **4**, 345, 10.1080/14702548808554534.

Ostrovsky, L. A., & Stepanyants, Y. A. 2005. Internal solitons in laboratory experiments: Comparison with theoretical models. *Chaos*, **15**, 1–28, dx.doi.org/10.1063/1.2107087.

Pedlosky, J. 1970. Finite-Amplitude Baroclinic waves. *J. Atmos. Sci.*, **27**, 15–30, dx.doi.org/10.1175/1520--0469(1970)027<0015:FABW>2.0.CO;2.

Pedlosky, J. 1987. *Geophysical Fluid Dynamics*. Springer.

Poincaré, Henry. 1885. Sur l'équilibre d'une masse de fluide animme d'un movement de rotation. *Acta Mathematica*, **VII**, 259–380.

Preusse, M., Peeters, F., & Lorke, A. 2010. Internal waves and the generation of turbulence in the thermocline of a large lakes. *Limnol. Oceanogr.*, **55(6)**, 2353–2365, dx.doi.org/10.4319/lo.2010.55.6.2353.

Preusse, M., Stastna, M., Freisthler, H., & Peeters, F. 2012a. Intrinsic breaking of internal solitary waves in a deep lake. *PloS One*, **7**, e41674. dx.doi.org/10.1371/journal.pone.0041674.

Preusse, M., Freisthler, H., & Peeters, F. 2012b. Seasonal variation of solitary wave properties in Lake Constance. *J. Geophys. Res.*, **117**, C04026, dx.doi.org/10.1029/2011JC007403.

Renouard, D. P., Chabert, D., & X., Zhang. 1987. An experimental study of strongly nonlinear waves in a rotating system. *J. Fluid Mech.*, **177**, 381–394, dx.doi.org/10.1017/S0022112087001009.

Renouard, D. P., Tomasson, G. G., & Melville, W. K. 1993. An experimental and numerical study of nonlinear internal waves. *Phys. Fluids*, **A 5**, 1401–1411, dx.doi.org/10.1063/1.858575.

Rozas, C., de la Fuente, A., Ulloa, H., Davies, P., & Niño, Y. 2014. Quantifying the effect of wind on internal wave resonance in lake Villarrica, Chile. *Environ. Fluid Mech.*, **14 (4)**, 849–871, dx.doi.org/10.1007/s10652--013--9329--9.

Sakai, S. 1989. Rossby-Kelvin instability: a new type of ageostrophic instability caused by a resonance between Rossby waves and gravity waves. *J. Fluid Mech.*, **202**, 149–176, dx.doi.org/10.1017/S0022112089001138.

Sakai, T., & Redekopp, L. G. 2010. A weakly nonlinear evolution model for long internal waves in a large lake. *J. Fluid Mech.*, **637**, 137–172, dx.doi.org/10.1017/S0022112010001114.

Sakai, T., & Redekopp, L. G. 2011. Lagrangian transport in a circular lake: effect of nonlinearity and the second vertical mode. *Nonlin. Processes Geophys*, **18**, 765–778, dx.doi.org/10.5194/

npg--18--765--2011.

Shih, L. H., Koseff, J. R., Ivey, G. N., & Ferziger, J. H. 2005. Parameterization of turbulent fluxes and scales using homogeneous shared stably stratified turbulence simulations. *J. Fluid Mech.*, **525**, 193–214: dx.doi.org/10.1017/S0022112004002587.

Shimizu, K., & Imberger, J. 2009. Damping mechanisms of internal waves in constinuously stratified rotating basins. *J. Fluid Mech.*, **637**, 137–172, dx.doi.org/10.1017/S0022112009008039.

Shimizu, K., & Imberger, J. 2010. Seasonal difference in the evolution of damped basin-scale internal waves in shallow stratified lake. *Limnol. Oceanogr.*, **55**, 1449–1462, dx.doi.org/10.4319/lo.2010.55.3.1449.

Shimizu, K., Imberger, J., & Kumagai, M. 2007. Horizontal structure and excitation of primary motion in a strongly stratified lake. *Limnol. Oceanogr.*, **52**, 2641–2655, dx.doi.org/10.4319/lo.2007.52.6.2641.

Spyksma, K., Magcalas, M., & Campbell, N. 2012. Quantifying effects of hyperviscosity on isotropic turbulence. *Phys. Fluids*, **24**, 125102, dx.doi.org/10.1063/1.4768809.

Staquet, C., & Sommeria, J. 2002. Internal gravity waves: From Instabilities to Turbulence. *Annu. Rev. Fluid Mech.*, **34**, 559–593, dx.doi.org/10.1146/annurev.fluid.34.090601.130953.

Stocker, R., & Imberger, J. 2003. Energy Partitioning and Horizontal Dispersion in a Stratified Rotating Lake. *J. Phys. Oceanogr.*, **33**, 512–529, dx.doi.org/10.1175/1520--0485(2003)033<0512:EPAHDI>2.0.CO;2.

Stocker, R., Imberger, J., & D'alpaos, L. 2000. An analitical model of a circular stratified rotating basin under the effect of periodic wind forcing. *In: In 5th Intl Symp. in Stratified Flows, Vancouver, Canada, pp. 387Ð392.*

Thomson, W. (Lord Kelvin). 1880. On gravitational oscillations of rotating water. *Proc. Roy. Soc. Edinburgh*, **10**, 92–100, dx.doi.org/10.1017/S0370164600043467.

Ulloa, H. N. 2011. *Estudio Experimental de la Respuesta de Ondas Internas Gravitacionales Afectadas por la Rotación Terrestre en un Flujo Estratificado*. Civil Engineering Thesis. Facultad de Ciencias Físicas y Matemáticas, Universidad de Chile, http://repositorio.uchile.cl/handle/2250/104097.

Ulloa, H. N., de la Fuente, A., & Niño, Y. 2014. An experimental study of the free evolution of rotating, nonlinear internal gravity waves in a two-layer stratified fluid. *J. Fluid Mech.*, **742**, 308–339, dx.doi.org/10.1017/jfm.2014.10.

Ulloa, H. N, Winters, K. B., de la Fuente, A., & Niño, Y. 2015a. Analytical Construction of Kelvin and Poincaré modes in a smooth two-layer stratification. Application to the wave regimes study. *In Prep.*

Ulloa, H. N., Winters, K. B., de la Fuente, A., & Niño, Y. 2015b. Degeneration of internal Kelvin waves in a continuous two-layer stratification. *J. Fluid Mech.*, **777**, 68–96, dx.doi.org/10.1017/jfm.2015.311.

Valipour, R. amd Bouffard, D., Boegman, L., & Rao, Y. R. 2015. Near-inertial waves in Lake Erie. *Limnol. Oceanogr.*, dx.doi.org/10.1002/lno.10114.

van Haren, H. 2015. Instability observations associated with wave breaking in the stable-stratified deep-ocean. *Physica D*, **292-293**, 62–69, dx.doi.org/10.1016/j.physd.2014.11.002.

Vincent, W. F. 2012. Forel's limnology - From lake physics to ecosystem services. *Limnol. Oceanogr. Bulletin*, **21**, 70–77, http://www.aslo.org/bulletin/12_v21_i3.pdf.

Waite, M. L., & Bartello, P. 2004. Stratified turbulence dominated by vortical motion. *J. Fluid Mech.*, **517**, 281–308, dx.doi.org/10.1017/S0022112004000977.

Wake, G. W., Ivey, G. N., Imberger, J., McDonald, N. R., & Stocker, R. 2004. Baroclinic geostrophic adjustment in a rotating circular basin. *J. Fluid Mech.*, **515**, 63–86, dx.doi.org/10.1017/S0022112004000230.

Wake, G. W., Ivey, G. N., & Imberger, J. 2005. The temporal evolution of baroclinic basin-scale waves in a rotating circular basin. *J. Fluid Mech*, **523**, 367–392, dx.doi.org/10.1017/S0022112004002344.

Watson, E. R. 1904. Movements of the waters on Loch Ness as indicated by temperature. *Geogr. J.*, **24**, 430–437, dx.doi.org/10.2307/1775951.

Wedderburn, E. M. 1908. An experimental investigation of the temperature changes occuring in fresh-water lochs. *Proc. Roy. Soc. Edinburgh*, **29**, 2–20, dx.doi.org/10.1017/S0370164600011524.

Wedderburn, E. M. 1909. Temperature observations in Loch Garry (Invernessshire). With notes on currents and seiches. *Proc. Roy. Soc. Edinburgh*, **29**, 98–135, dx.doi.org/10.1017/S0370164600008853.

Wedderburn, E. M. 1912. Temperature observations in Loch Earn, wirh a further contribution to the hydrodynamical theory of the temperature seiche. *Proc. Roy. Soc. Edinburgh*, **48**, 629–695, dx.doi.org/10.1017/S0080456800015842.

Winters, K. B., & D'Asaro, E. A. 1996. Diascalar flux and the rate of fluid mixing. *J. Fluid Mech.*, **317**, 179–193, dx.doi.org/10.1017/S0022112096000717.

Winters, K. B., & D'Asaro, E. A. 1997. Direct simulation of internal wave energy transfer. *J. Phys. Oceanogr.*, **27**, 1937–1945, dx.doi.org/10.1175/1520--0485(1997)027<1937:DSOIWE>2.0.CO;2.

Winters, K. B., & de la Fuente, A. 2012. Modelling rotating stratified flows at laboratory-scale using spectrally-based DNS. *Ocean Modelling*, **50**, 47–59, dx.doi.org/10.1016/j.ocemod.2012.04.001.

Winters, K. B., Lombard, P. N., Riley, J. J., & D'Asaro, E. A. 1995. Available potential energy and mixing in density-stratified fluids. *J. Fluid Mech.*, **289**, 115–128, dx.doi.org/10.1017/S002211209500125X.

Wüest, A., & Lorke, A. 2003. Small-Scale Hydrodynamics in Lakes. *Annu. Rev. Fluid Mech.*, **35**, 373–412, dx.doi.org/10.1146/annurev.fluid.35.101101.161220.